LEGIBILITY NOTICE

A major purpose of the Technical Information Center is to provide the broadest dissemination possible of information contained in DOE's Research and Development Reports to business, industry, the academic community, and federal, state and local governments.

Although a small portion of this report is not reproducible, it is being made available to expedite the availability of information on the research discussed herein.

1

D3
4-11-83
W.B.

I-8130 ② Dr. 1314

ORNL-5864

ornl

OAK
RIDGE
NATIONAL
LABORATORY

UNION
CARBIDE

Development of a Fuel-Rod Simulator and Small-Diameter Thermocouples for High-Temperature, High Heat Flux Tests in the Gas-Cooled Fast Reactor Core Flow Test Loop

R. W. McCulloch
R. E. MacPherson

OPERATED BY
UNION CARBIDE CORPORATION
FOR THE UNITED STATES
DEPARTMENT OF ENERGY

MASTER

DISTRIBUTION OF THIS DOCUMENT IS UNLIMITED

Printed in the United States of America. Available from
National Technical Information Service
U.S. Department of Commerce
5285 Port Royal Road, Springfield, Virginia 22161
NTIS price codes--Printed Copy: A07 Microfiche A01

This report was prepared as an account of work sponsored by an agency of the United States Government. Neither the United States Government nor any agency thereof, nor any of their employees, makes any warranty, express or implied, or assumes any legal liability or responsibility for the accuracy, completeness, or usefulness of any information, apparatus, product, or process disclosed, or represents that its use would not infringe privately owned rights. Reference herein to any specific commercial product, process, or service by trade name, trademark, manufacturer, or otherwise, does not necessarily constitute or imply its endorsement, recommendation, or favoring by the United States Government or any agency thereof. The views and opinions of authors expressed herein do not necessarily state or reflect those of the United States Government or any agency thereof.

ORNL--5864

DE83 009877

ORNL-5864
Dist. Category UC-77

Contract No. W-7405-eng-26

Engineering Technology Division

GAS-COOLED REACTOR PROGRAMS

DEVELOPMENT OF A FUEL-ROD SIMULATOR AND SMALL-DIAMETER THERMOCOUPLES FOR HIGH-TEMPERATURE, HIGH-HEAT-FLUX TESTS IN THE GAS-COOLED FAST REACTOR CORE FLOW TEST LOOP

R. W. McCulloch   R. E. MacPherson

Date Published - March 1983

NOTICE
PORTIONS OF THIS REPORT ARE ILLEGIBLE.
It has been reproduced from the best available copy to permit the broadest possible availability.

Prepared by the
OAK RIDGE NATIONAL LABORATORY
Oak Ridge, Tennessee 37830
operated by
UNION CARBIDE CORPORATION
for the
DEPARTMENT OF ENERGY

DISCLAIMER

This report was prepared as an account of work sponsored by an agency of the United States Government. Neither the United States Government nor any agency thereof, nor any of their employees, makes any warranty, express or implied, or assumes any legal liability or responsibility for the accuracy, completeness, or usefulness of any information, apparatus, product, or process disclosed, or represents that its use would not infringe privately owned rights. Reference herein to any specific commercial product, process, or service by trade name, trademark, manufacturer, or otherwise does not necessarily constitute or imply its endorsement, recommendation, or favoring by the United States Government or any agency thereof. The views and opinions of authors expressed herein do not necessarily state or reflect those of the United States Government or any agency thereof.

CONTENTS

ACKNOWLEDGMENTS

Contributions of a great many people were essential for the successful development of the Gas Cooled Fast Reactor—Core Flow Test Loop fuel rod simulator (FRS). The initial efforts of D. L. Clark on the concept and design and the patience and suggestions of many industrial heater manufacturers are appreciated. The pioneering work of C. S. Morgan's boron nitride preform development and A. S. Moorhead's development of joining techniques finally made fabrication reasonable to consider, while many contributions by R. E. Dial and W. R. Finnell in fabrication, tooling, and thermocouple development made fabrication not only possible but highly controlled and repeatable. The radiographic and infrared inspection skills of S. D. Snyder gave us badly needed insight into the subtle relationships of the fabrication process to FRS performance, without which success would have been impossible. The continued support of D. W. Post and R. T. Lovell for fabrication of variable width ribbon heating elements and of R. L. Ludwig for metallographic and failure analysis are also greatly appreciated. Finally, we wish to acknowledge the guidance, support and intuitive direction of A. G. Grindell throughout the entire effort and of Uri Gat and P. R. Kasten for providing both financial and moral support.

DEVELOPMENT OF A FUEL ROD SIMULATOR AND SMALL-DIAMETER THERMOCOUPLES FOR HIGH-TEMPERATURE, HIGH HEAT FLUX TESTS IN THE GAS-COOLED FAST REACTOR CORE FLOW TEST LOOP

R. W. McCulloch   R. E. MacPherson

ABSTRACT

The Core Flow Test Loop was constructed to perform many of the safety, core design, and mechanical interaction tests in support of the Gas-Cooled Fast Reactor (GCFR) using electrically heated fuel rod simulators (FRSs). Operation includes many off-normal or postulated accident sequences including transient, high-power, and high-temperature operation. The FRS was developed to survive (1) hundreds of hours of operation at 200 W/cm², 1000°C cladding temperature, and (2) 40 h at 40 W/cm², 1200°C cladding temperature. Six 0.5-mm type K sheathed thermocouples were placed inside the FRS cladding to measure steady-state and transient temperatures through clad melting at 1370°C.

Development included laser welding and furnace brazing techniques to join 0.25-mm wall copper-to-nickel tubular terminals and 2-mm-diam terminal rods to themselves and to the helical ribbon heating element. Joints successfully withstood as many as 5000 thermal transients and operation near 1000°C at current densities as high as 4000 A/cm². Variable-width ribbon heating elements were fabricated that provided cosine axial heat-flux patterns accurate to ±2.5%. Boron nitride preform fabrication techniques were extended to obtain 90% theoretical density in inner and outer annular regions without swaging to reduce cladding diameter. This allowed the use of cladding prototypical to the GCFR in both surface "ribbing" and cold work. Finally, reliability of FRS thermocouples was improved to ~100% from near 0%. Major accomplishments were (1) the reduction of thermoelement grain size by a factor of 2 to ~17 μ, (2) discovery of the adverse effects of residual cold work on thermoelement embrittlement, and (3) subsequent elimination of this cold work prior to thermocouple use.

---

1. INTRODUCTION

1.1 General

This report summarizes the efforts made toward the development of a reliable, high-temperature, high heat flux fuel rod simulator (FRS) and its associated internal thermocouples for use in that portion of the Gas-

Cooled Fast Reactor—Core Flow Test Loop (GCFR-CFTL) Test Program related to the operation of simulated core assemblies. Although the total effort spanned more than six years, emphasis is placed on the last four years when most of the pertinent FRS development, fabrication, and testing took place. References 1–4 detail GCFR-CFTL development over this period.

The CFTL, shown in Fig. 1, is a high-temperature, high-pressure, fast-transient, out-of-reactor gas loop that is designed to supply helium to a test bundle at appropriate temperature and pressure conditions. The test bundle consists of electrically heated FRSs that are arranged to represent a segment of the GCFR core. The CFTL was designed to accommodate rod bundles of 37, 61, and 91 FRSs and to operate from ambient pressure to 10.3

ORNL-DWG 78-16148

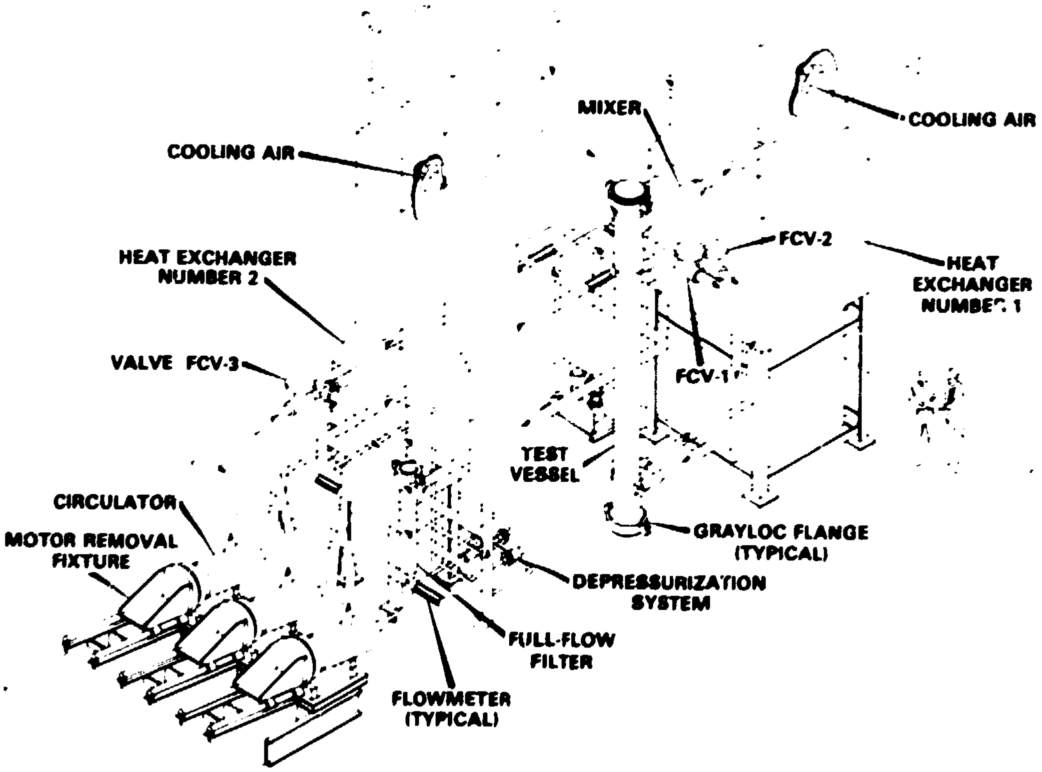

Fig. 1. CFTL.

MPa, from 300 to 1370°C, and at FRS power levels from 0 to 43 kW/rod (0 to 4 MW total power). The principal objectives of the test program were the acquisition and analysis of test data on (1) thermal and pressure-drop characteristics, (2) design and safety margins, and (3) friction and thermal mechanical behavior of test bundles that simulate portions of GCFR fuel and control assemblies. The CFTL test bundles were to be operated with flat or skewed power distributions at prescribed power levels and slopes and at steady-state or transient conditions. Transient operation was to include prescribed variations (with time) of test bundle power, helium pressure, and coolant flow rate to simulate normal, upset, emergency, and faulted accident transients. Depressurization accidents were also included in the test program. Data obtained were to be primarily from thermocouples, most of which are integral components of the FRSs.

The CFTL was essentially complete when the GCFR funding was discontinued. Because of its versatility, it has been dedicated to support the High-Temperature Gas-Cooled Reactor (HTGR) Program.

The current design of the CFTL FRS is shown in Fig. 2. The FRS cladding is prototypical of the 316 stainless steel alloy that was to have been used in the manufacture of GCFR fuel rod cladding and thus has the same dimensions, configuration, and thermal and mechanical characteristics. The length of the FRS is 2860 mm, 1200 mm of which is heated; the outside diameter (OD) is 8 mm. A length of 1220 mm of the outer surface, slightly overlapping the heated length, is roughened to enhance heat transfer to the helium. The FRS is reentrant in design; that is, both power terminals enter at a single end. The outer terminal, a copper tube, is joined to a tubular nickel conductor which, in turn, is joined to the variable width Kanthal A-1* heating element. Nichrome V and platinum-8% tungsten heating elements were used in earlier prototypes. The heating element is designed to provide a cosine heat flux distribution. The center terminal is made of a solid copper rod that is joined to a nickel conductor. This conductor, in turn, is joined through an adapter to the other end of the heating element to complete the electric-current-carrying

---

*Trademark of the Kanthal Corporation, Bethel, CT 06801.

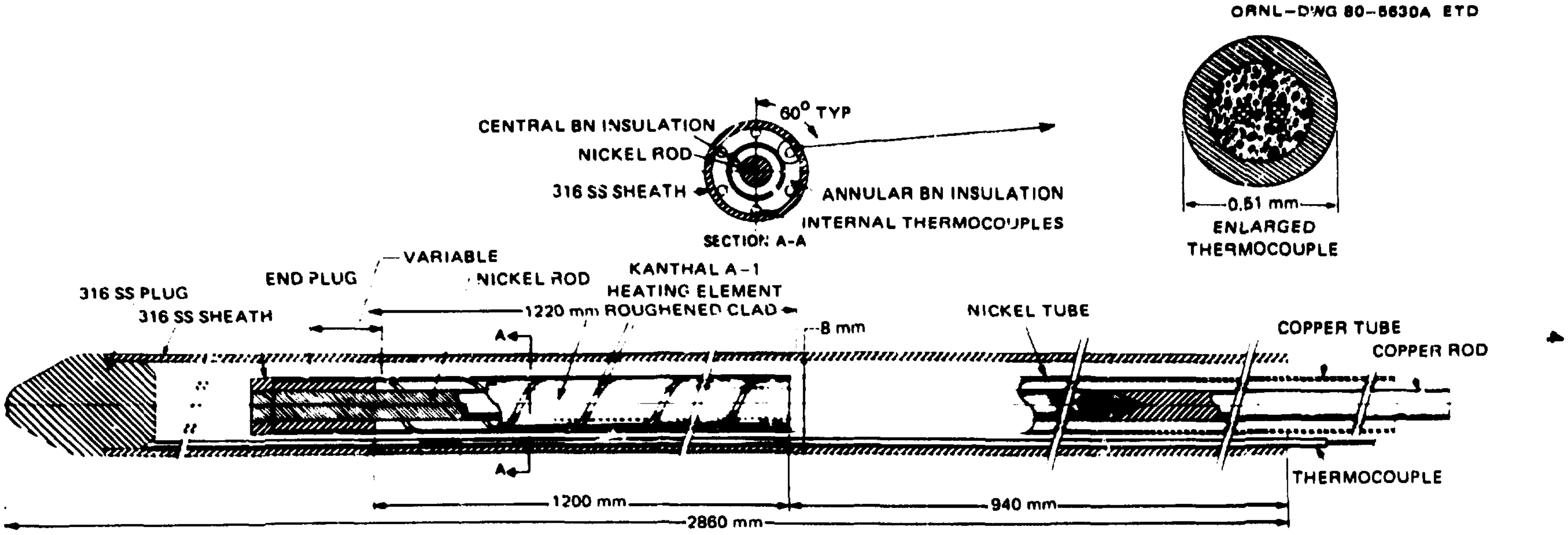

Fig. 2. GCFR-CFTL FRS.

circuit in the FRS. Cold-pressed boron nitride (BN) preforms provide electrical insulation and thermal conductance between (1) the cladding and the heating element with its associated tubular conductor and terminal (outer annulus) and (2) the heating element and the center conductor with its terminal (inner annulus). Swaging was used on early CFTL FRSs to provide final compaction of the BN preforms. Later models were made using a special "nonswaged" fabrication technology to preserve the prototypical properties of the GCFR clad. Six type K thermocouples (four on earlier FRSs) with insulated junctions are installed inside the FRS cladding. The sheaths of the thermocouples run longitudinally along the inside surface parallel to the axis of the cladding at 60° circumferential intervals.

The operating conditions place stringent requirements on all materials used in the FRS. The heating element must operate at the maximum temperature without property degradation. The BN must maintain both high thermal conductivity and electrical resistivity at the maximum temperature; additionally, its properties must remain uniform axially and circumferentially to provide accurate simulation of the cosine heat flux. The FRS must also maintain its integrity while enduring thermal transient tests.

The FRS development program staff at Oak Ridge National Laboratory (ORNL) has performed materials, fabrication, inspection, testing, and failure analysis tasks to prepare procedures that are satisfactory for the production of adequate CFTL FRSs.

The associated FRS and thermocouple technology, developed in support of CFTL, has application to out-of-reactor safety tests in light-water reactor, liquid-metal fast breeder reactor, and other systems where transient, high heat flux, high-temperature operation is required in conjunction with useful reliability.

The results of the development work are largely positive. The FRSs can be fabricated to operate for more than 1000 h at 1000°C and power as high as 200 W/cm^2 and 50 h at 1200°C and 40 W/cm^2.

The difficulties associated with the GCFR configuration, the most complex high-performance FRS we have attempted, were surmounted. These included a central current return conductor, six internal 0.5-mm thermocouples, and a variable width heating element to produce accurately the requisite "chopped" cosine heat flux distribution.

A new nonswaged FRS technology was created to preserve the requisite clad roughening during fabrication for enhancing heat transfer and maintaining the initial cold work requirements. This method made available, for the first time, a high heat flux high-temperature FRS fabricated with cladding identical to that of the fuel rod it simulated.

Major materials joining, inspection, and terminal heat generation problems were solved. High-temperature braze joints and laser butt-welded connections with previously unattainable electrical and dimensional tolerances were developed. Thousands of stringent thermal cycles between 350 and 1000°C and much steady-state operation at temperatures to 1200°C were logged during development tests made with several prototypical rods.

Major problems with small-diameter 0.50-mm thermocouples, internal to the FRS, were solved. Thermocouple failures were reduced from 100% in early rod prototypes containing four thermocouples to zero percent for recent prototypes containing six thermocouples. Techniques to manufacture refined-grain-size thermocouples were developed that enabled production of thermocouples having Alumel and Chromel thermoelements that had a maximum grain size of ASTM 8.5 (19 μm) and 11 (8 μm), respectively, for a thermoelement having a diameter of 76 μm. The harmful effect of critical levels of residual cold-work on thermocouple lifetime was discovered, and a method was devised to eliminate it. These thermocouples, when properly manufactured and assembled in accordance with the developed technique, were shown to survive the GCFR operational condition imposed on them.

Nevertheless, the GCFR FRS still has several shortcomings even after the completion of considerable development. The use of nickel material for the central current return conductor adversely affects FRS reliability. The conductor material was initially specified to be, and remains, nickel. No better material is available that matches the combined requirements of high melting point, thermal expansion comparable to stainless steel, and low electrical resistivity at high temperatures. The included a central current return conductor, six internal 0.5-mm thermocouples, and a variable width heating element to produce accurately the requisite "chopped" cosine heat flux distribution.

A new nonswaged FRS technology was created to preserve the requisite clad roughening during fabrication for enhancing heat transfer and maintaining the initial cold work requirements. This method made available, for the first time, a high heat flux high-temperature FRS fabricated with cladding identical to that of the fuel rod it simulated.

Major materials joining, inspection, and terminal heat generation problems were solved. High-temperature braze joints and laser butt-welded connections with previously unattainable electrical and dimensional tolerances were developed. Thousands of stringent thermal cycles between 350 and 1000°C and much steady-state operation at temperatures to 1200°C were logged during development tests made with several prototypical rods.

Major problems with small-diameter 0.50-mm thermocouples, internal to the FRS, were solved. Thermocouple failures were reduced from 100% in early rod prototypes containing four thermocouples to zero percent for recent prototypes containing six thermocouples. Techniques to manufacture refined-grain-size thermocouples were developed that enabled production of thermocouples having Alumel and Chromel thermoelements that had a maximum grain size of ASTM 8.5 (19 μm) and 11 (8 μm), respectively, for a thermoelement having a diameter of 76 μm. The harmful effect of critical levels of residual cold-work on thermocouple lifetime was discovered, and a method was devised to eliminate it. These thermocouples, when properly manufactured and assembled in accordance with the developed technique, were shown to survive the GCFR operational condition imposed on them.

Nevertheless, the GCFR FRS still has several shortcomings even after the completion of considerable development. The use of nickel material for the central current return conductor adversely affects FRS reliability. The conductor material was initially specified to be, and remains, nickel. No better material is available that matches the combined requirements of high melting point, thermal expansion comparable to stainless steel, and low electrical resistivity at high temperatures. The nickel melting point, 50°C lower than that of the Kanthal A-1 heating element, precludes higher operational performance or, alternately, reduces operational time at internal temperatures above 1000°C.

Additionally, a relatively slow boron-nickel eutectic reaction was shown to occur at the higher temperatures. This reaction reduces the equivalent nickel melting point from 1450 to ~1000°C, which limits both lifetime and thermal cycling ability of the rods. This problem could be eliminated with the use of central magnesium oxide (MgO) cold-pressed insulators. However, project closeout did not permit us to try to accomplish this goal.

Chapter 2 details the FRS fabrication and testing and describes much of the component development necessary to enable successful FRS operation. Chapters 3 and 4 report the achievements in BN preform technology and variable width ribbon fabrication that paralleled and influenced much of the FRS development. Finally, Chap. 5 delineates the investigations and subsequent development that resulted in 0.5-mm type K, sheathed, insulated-junction thermocouples that would survive thousands of thermal cycles and operation to 1200°C without failure.

1.2 Integrated Technology Development for FRS Fabrication

Initial CFTL FRS development took place in conjunction with industrial fabricators. The FRSs were designed by ORNL, performance specifications were written, and prototype contracts were awarded. This approach resulted in poor quality and constantly changing delivery schedules. The FRS performance was often greatly affected by subtle fabrication changes that were difficult to control or even define.

In response to continuing procurement problems, an integrated FRS Technology Development Program was established at ORNL. Its charter was to (1) develop design, material, and fabrication procedures that directly related to individual program requirements and (2) generate fabrication specifications that then could be used by industry to produce FRSs of the quality levels required, according to the schedules needed. This was to be accomplished by (1) developing fabrication techniques, processes, and inspection methods; (2) verifying that inspections were adequate to control the processes; (3) testing FRSs to verify that operational requirements were met; (4) fabricating a statistically significant number of FRSs to establish confidence in the procedures; and (5) generating a detailed fabrication specification to guide future procurement.

In establishing the FRS Technology Development Program, the decision was made to use cold-pressed BN preform technology exclusively because of the high degree of fabrication control and simulator property uniformity achievable with this method. Earlier work had shown considerable promise and a substantial improvement over powder-filling technology.[5]

References 6 and 7 document this technology development effort, which demonstrated that high-quality fuel simulators can be routinely fabricated under carefully controlled conditions. The CFTL FRS development paralleled much of this work and was directly applicable. The end result was extension of the technology through the development of nonswaged FRS fabrication techniques to enable the CFTL FRS to meet GCFR fuel rod cladding mechanical and surface roughening requirements for GCFR fuel rod cladding.

2. CFTL FRS FABRICATION AND TESTING

2.1 General

During the period from January 1977 until September 16, 1980, when the CFTL FRS development was suspended, 26 FRS prototypes and nine FRS prototypical conductivity test cells were fabricated. Of these, 20 prototypes and 8 test cells were operationally tested. The fabrication process that evolved throughout this development effort was carefully controlled, post-process inspections were completed on each prototype, and thousands of hours of high-temperature, high- and low-power and transient operation were logged.

Table 1 summarizes the FRS prototype fabrication and testing efforts and includes information on heating element and other components, number and types of internal thermocouples, and a brief summary of fabrication and testing highlights. This section provides a chronological description of the results summarized by Table 1.

Fabrication development and testing can be roughly divided into five phases. Phase I, which encompassed the first eight prototypes, saw the initiation of local fabrication development towards the solution of CFTL FRS problems. Major FRS fabrication and joining problems were encountered, and most work was on refractory alloy FRSs. The fabrication of a viable FRS to meet CFTL test requirements was demonstrated with GNR-L-7P, the last in this phase, but major reliability problems with rod internal thermocouples were uncovered.

In phase II, we extended the fabrication technology to include nonswaged FRSs, which allowed the use of "ribbed" and cold worked prototypical GCFR cladding. Thermocouple failure mechanisms were uncovered and most of the thermocouple reliability problems solved simply by going to a nonswaged FRS. High temperature (>1200°C) and high power (38 kW), sodium temperature operations were successfully demonstrated in this phase.

Phase III, which included all conductivity test cells, paralleled other phases. Test cells were a simplified means of obtaining information about BN preform and fabrication parameters. The preform density was the major factor influencing annular thermal conductivity (k), k varied with

Table 1. Summary of CFTL FRS and conductivity test cell fabrication and testing

Phase	Rod serial No.[a]	Heating element materials	Tubular lead materials	Central rod materials	Instrumentation[b]	Test stand[c]	Remarks[d]
I	None	Nichrome V	Nickel	Molybdenum	None		Sizing tolerance too large; fabrication discontinued
I	GLR-L-1P	Nichrome V	Nickel	Molybdenum	Four 0.5-mm type K TC with stainless steel sheath; 2 IJ; 2 GJ	HTS	First GCFR FRS operated satisfactorily in dc-leakage test
I	GLS-L-2P	Platinum-8% tungsten	Molybdenum	Molybdenum	Four 0.5-mm type K TC with stainless steel sheath; 2 IJ; 2 GJ		Platinum-tungsten to molybdenum butt weld separated during swaging
I	GLS-L-3P	Platinum-8% tungsten	Molybdenum	Molybdenum	Four 0.5-mm type K TC with stainless steel sheath; 2 IJ; 2 GJ		Failed during postanneal IR scan; organic impurity in central BN
I	GLS-L-4P	Platinum-8% tungsten	Molybdenum	Molybdenum	Four 0.5-mm type K TC with stainless steel sheath; 4 IJ	HTS	Successful; operated up to 1250°C; severe differential thermal expansion mismatch
I	GLR-L-5P	Nichrome V	Nickel/copper	Nickel/copper	Four 0.5-mm type K TC with Inconel 600 sheath; 4 IJ		Successful; two Inconel TCs broke at tab during fabrication
I	GLF-L-6P (FR-6P)	Nichrome V	Nickel/copper	Nickel/copper	Four 0.5-mm type K TC with Inconel 600 sheath; 4 IJ	HTS	Lost one TC; nickel/copper braze failed; repaired and operated to 1250°C
I	GLR-L-7P	Nichrome V	Nickel	Nickel	Four 0.5-mm type K SDI TCs with Inconel 600 sheath; all IJ	HTS	Successfully fabricated; tested at 700–900°C for >1000 h; completed >1000 transients; ran to failure at 1250°C; TCs showed susceptibility to transients and high temperature
II	GNR-L-8P	Nichrome V	Nickel	Nickel	None		First nonswaged rod prototype; fabricated for evaluation purposes
II	GR-L-9P	Nichrome V (variable width)	Nickel/copper	Nickel/copper	Four 0.5-mm type K SDI TCs with Inconel sheath, all IJ		Nonswaged preform caused excessive movement of heating element; TCs got crossed; terminal region was shortened to correct problem; postfabrication inspection normal, but length too short to test
II	GR-L-10P	Nichrome V (variable width)	Nickel/copper	Nickel/copper	Four 0.5-mm type K SDI TCs with Inconel sheath; 3 IJ, 1 GJ	SRSL	Encountered copper spalling of central rod during fabrication; rod failed prematurely during testing because of spalling; developed nondestructive elongation method of correcting spalling and testing copper/nickel braze joint.
II	GNR-L-11P	Nichrome V (variable width)	Nickel/copper	Nickel/copper	Four 0.5-mm type K SDI TCs with Inconel sheath; all IJ	SRSL	First successful nonswaged FRS; tested to destruction in SRSL.
II	GNR-L-12P	Nichrome V (variable width)	Nickel/copper	Nickel/copper	Four 0.5-mm type K SDI TCs with Inconel	SRSL	Repeat of -11P; all satisfactory; tested in SRSL; first FRS to meet all normal CFTL requirements
III	GNT-L-13S	Nichrome V	Nickel/copper	None/platinum (type B) TC	Four 0.5-mm type K SDI TCS with Inconel sheath; all IJ	WCTS	First conductivity cell tested in WCTS

Table 1 (continued)

Phase	Rod serial No.[a]	Heating element material	Tubular lead materials	Central rod materials	Instrumentation[b]	Test stand[c]	Remarks[d]
III	GNT-L-14S	Nichrome V	Nickel/copper	None/platinum (type B) TC	Four 0.5-mm type K	WCTS/ SRSL	Tested in WCTS and in SRSL; showed clearly high nonswaged thermal conductivity and its dependence on power and sheath temperature
III	GNT-L-17S	Kanthal A-1	Nickel/copper	None/platinum (type B) TC	None	WCTS	Tested in WCTS to obtain additional BN κ vs temperature and power data
III	GNT-L-18S	Kanthal A-1	Nickel/copper	None/platinum (type B) TC	None	WCTS	Tested in WCTS to obtain additional BN κ vs temperature and power data
III	GNT-L-19S	Kanthal A-1	Nickel/copper	Type K TC	None	WCTS	Similar results to those obtained on previous conductivity cells
III	GNT-L-20S	Nichrome V	Nickel	Type K TC	None	WCTS	Contained an MgO-15 wt % BN central preform; κ was ~10% higher than with previous test cells; MgO-BN performed well electrically at 1350°C
III	GNK-L-28S	Kanthal A-1 (constant width)	Nickel	Type K TC	None		Test cell was fabricated to further evaluate effects of preform length and tamping energy on FRS transient properties; IR scans indicated preform length should be maintained at 10 mm or less
III	GNK-L-30S	Kanthal A-1 (constant width)	Nickel/copper	Type K TC	None	WCTS	Used TS-1449 annular BN preform
III	GNK-L-31S	Kanthal A-1 (constant width)	Nickel/copper	Type K TC	None	WCTS	Used PT-13 treated preforms made from TS-1449 powder
IV	GNK-L-15P	Kanthal A-1	Nickel/copper	Molybdenum/ copper	Four 0.5-mm type K CSG TCs with Inconel sheath; 2 IJ, 1 MGJ, 1 BNBF IJ		First FRS with Kanthal heating element; Kanthal-tube weld failed during fabrication
IV	GNK-L-16P	Kanthal A-1	Nickel/copper	Nickel/copper	Four 0.5-mm type K CSG HTS TCs with Inconel sheath, 1 GJ, 3 MGJ		Successfully fabricated, test in HTS to determine thermal cycling effect on Kanthal FRS tested satisfactorily; TCs survived >400 stringent transient cycles
IV	GNK-L-21P	Kanthal A-1 (constant width)	Nickel/copper	Nickel/copper	Four CSG type K in Inconel TCs with IJ	HTS	Successfully operated 309 h at steady-state temperature 700-1100°C with 4[illegible] h at 1100°C; successfully completed ~4000 thermal cycles, some very severe, with no TC losses; Kanthal/nickel butt weld successful
IV	GNK-L-22P	Kanthal A-1 (variable width)	Nickel/copper	Nickel/copper	Four GMI type K in Inconel TCs with IJ	SRSL	Operated [illegible]-h steady-state at [illegible] kW, 650°C cladding temperature; endured [illegible] transient cycles with power [illegible]-41 kW, cladding temperature 365-650°C; failed during [illegible]-30 kW, [illegible] by nickel rod melting; all TCs survived
IV	GNK-L-23P	Kanthal A-1 (variable width)	Nickel/copper	Nickel/copper	Four GMI type K in Inconel TCs with IJ	HTS	Successfully operated [illegible] h at steady-state temperature 700-1100°C with 32 h at 1100°C, successfully completed ~5000 thermal cycles similar to those of -21P; all TCs survived.

Table 1 (continued)

Phase	Rod serial No.[a]	Heating element material	Tubular lead materials	Central rod materials	Instrumentation[b]	Test stand[c]	Remarks[d]
IV	GNK-2-24P	Kanthal A-1 (variable width)	Nickel/copper	Nickel/copper	Three, type K in Inconel TCs from GMI; open type S TC; all IJ	SRSL	Fabrication defects in rod, type S TC tab pulled off; tested in SRSL even though it was not fully acceptable; endured 19 h of steady-state and transient operation before failure at 38 kW, 750°C cladding temperature; fabrication defects led to premature failure
IV	GNK-2-25P	Kanthal A-1 (variable width)	Nickel/copper	Nickel/copper	Four, type K in Inconel IJ TCs: two from CSG; two from GMI	HTS	Operated 100 h, 35 h at 700°C; ran approach-to-cladding-melting tests 700–1400°C cladding temperature; rod survived 1 min at 1400°C cladding temperature in vacuum, later reached 1300°C cladding temperature in helium before failure
IV	GNK-2-26P	Kanthal A-1 (variable width)	Nickel/copper	Nickel/copper	Four, type K in SS, BNBF IJ TCs from GMI	SRSL	Experienced fabrication problems in nickel end plug region but corrected; rod operated 32 h steady-state and transient at 10 to 29 kW, 740–780°C cladding temperature; premature failures occurred by melting of nickel rod adjacent to end plug
IV	GNK-2-27P	Kanthal A (variable width)	Nickel/copper	Nickel/copper	None	SRSL	Rod operated 70-h steady state 10–34 kW at cladding temperature 700–925°C; failure was similar to that of -26P
V	GNK-2-29P	Kanthal A-1 (variable width)	Nickel/copper	Nickel/copper	None	HTS	First 5-mm rod, electrical breakdown of inner BN region to scale on Kanthal A-1 material
V	GNK-2-32P	Kanthal A-1 (variable width)	Nickel/copper	Nickel/copper	Six each type K IJ, 304 steady-state sheathed TCs	SRSL	Fabrication problems similar to 29P used GA roughened cladding; rod endured 700 h of steady-state transient tests and 8000 thermal cycles without TC failure; evidence of boron-nickel reaction
V	GNK-2-33P	Kanthal A-1 (variable width)	Nickel/copper	Nickel/copper	Four each type K IJ, 304 SS, sheathed TCs, 2 Pt sheathed type S TCs	HTS	Fabrication successful; rod tested for 1972 h and 12,490 thermal cycles; two type S TCs failed, four type K TCs survived all operation until failure
V	GNK-2-34P	Kanthal A-1 (variable width)	Nickel/copper	Nickel/copper	Six each type K, IJ, Inconel-sheathed TCs from GMI	SRSL	Fabrication successful; tested for 556 h and 5800 cycles in SRSL; steady-state and transient power was 29 kW + 0 to 29 kW, respectively; failure similar to -32 P; differential thermal expansion on central nickel rod, weakened by boron/nickel reaction, failed during thermal cycling

---

[a] Serial number postscript S indicates conductivity cell and postscript P indicates FRS prototype.

[b] IJ = insulated junction, GJ = ground junction, MGJ = modified ground junction, TC = thermocouple, SDI = Sensor Dynamic, Inc., GMI = Groth Mazur Industries, CSG = Claude S. Gordon, BNBF = BN backfilled and SS = stainless steel.

[c] WCTS = water test stand, HTS = helium test stand, and SRSL = single-rod sodium loop.

[d] IR = infrared, and K = thermal conductivity.

heat flux, and MgO central preforms (with increased thermal expansion over BN) enhanced annular k.

During phase IV, the Kanthal A-1 heating element was exclusively used to extend the FRS operational range by allowing 50°C higher internal temperatures; long-time operation and extended thermal cycling (>10,000 cycles) of FRSs were demonstrated, and type K thermocouple failures were virtually eliminated.

Phase V was concerned primarily with the 8-mm-diam FRS, which generally included six internal thermocouples. The nonswaged FRS technology was improved with the use of a higher density BN preform; roughened General Atomic (GA) cladding was obtained and used, and the susceptibility of the central nickel rod to failure during high-power thermal cycling in the Single Rod Sodium Loop (SRSL) was uncovered. Suspicion of boron-nickel incompatibility was verified, but the limitations were not defined. The use of MgO central preforms to solve compatibility problems as well as enhance operation capability could not be pursued to a determination because the CCFR-CFTL activities were closed out.

2.2 Phase I – Initial Development

The first fabrication attempt in this phase (see Table 1) failed because of problems with terminal-to-preform sizing tolerance. However, information and tooling developed during the attempt were used to fabricate the first instrumented CFTL rod, GLR-L-1P. This rod contained a Nichrome V heating element, a nickel tubular terminal, and a molybdenum central rod for current return. Four type K stainless-steel-sheathed thermocouples, two with insulated junctions and two with grounded junctions, were welded to precise axial and circumferential locations inside the sheath. The unit was subjected to a high-temperature dc-leakage test in the helium test stand (HTS) and failed shortly after reaching the clad melting temperature.

The next three units (GLS-L-2P, -3P, and -4P) contained a platinum-8% tungsten alloy heating element and molybdenum tubular and central terminals. Only the last of the three was successfully fabricated. The first failed when a molybdenum-platinum laser weld separated during swaging, and the second failed during the postanneal infrared scan because of internal organic contamination. Improvements in terminal joining techniques using these materials were developed as a result of the first failure. Modification of the fabrication procedure to allow a check of the active component assembly for organic impurities was incorporated as a result of the second failure.

Unit GLS-L-4P was tested in the HTS and subjected to rigorous operation. The BN preform resistance vs temperature data up to 1200°C were obtained for the annular region. Data showed the BN resistance to be 3 kΩ at 1200°C. The high-temperature resistance slope of approximately a factor of 10 decrease per 150°C indicated that the resistance remained adequate up to clad melting temperatures. Rod failure occurred at a measured sheath temperature of 1260°C and 8 kW of power, but no BN resistance data were obtained at that temperature level.

Failure analysis of rod -4P indicated that excessive differential thermal expansion between the central molybdenum rod and the 316 stainless steel sheath contributed to its failure. The lower thermal expansion of molybdenum [6.1×10^{-6} μm/m°C vs 19.8×10^{-6} μm/m°C for austenitic stainless steel at 1200°C] resulted in shearing the weld that joined the end plug to the molybdenum rod. The plug moved about 1.75 cm along the rod. Normal operation was experienced at the high temperatures; however, when the FRS cooled, the molybdenum rod became hung up rather than able to slide freely back into the end plug. Tensile forces in the stainless steel sheath, caused by its greater contraction during cooling than experienced by the molybdenum rod, resulted in the separation of the sheath at two axial locations totalling about 1.75 cm.

Because of the differential thermal expansion problems experienced on GLS-L-4P as well as the withdrawal of funding support for platinum-tungsten alloy improvement, emphasis was shifted to the reference rod design; a Nichrome V heating element and copper-nickel terminals were used on subsequently fabricated rods. Additionally, the decision was made to substitute Inconel 600 material for the stainless steel sheath on the type K thermocouples because the Inconel sheaths caused less decalibration errors at temperatures up to 1150°C.

Rod GLR-L-5P was fabricated using these reference materials. During fabrication, tabs welded to the junction ends of two of the four internal thermocouples broke off. Otherwise, fabrication of the unit was normal. The rod was not tested because insufficient data would have been obtained without complete internal instrumentation.

In the next rod, GLR-L-6P, one of the four Inconel tabs broke from a thermocouple sheath during rod fabrication. The tab fabrication procedure, which consisted of welding a bead on the junction end and swaging it down to the thermocouple diameter, was reviewed and found to be adequate. However, an annealing step subsequent to tab fabrication was added, and the 1.36-kg tensile force, applied to each thermocouple during rod fabrication, was reduced to a value of 0.23 kg.

Separation of the braze joining the nickel-copper central rods occurred during swaging of rod GLR-L-6P. Failure occurred because of inadequate temperature control of the braze joint during brazing. The brazing operation for the rod was then modified and proved successful on later prototypes.

The rod was repaired and operated in a dc-leakage test in the HTS. It failed at a measured sheath temperature of 1150°C. Analysis indicated that the failure occurred because there was a low-density area in the inner BN insulation. Several hours prior to failure of the rod during operation at a measured temperature of 1150°C, a short occurred in the electrical circuits external to the rod, causing a sharp temperature ramp that brought the rod cladding temperature briefly up to 1250°C. Although the rod survived this incident, the subsequent failure might have been initiated at that time because of overheating in the area of low-density BN.

The FRS prototype GLR-L-7P contained a constant width Nichrome V heating element, a nickel tubular terminal, and a nickel central rod and terminal. The stainless steel sheath contained four internal 0.5-mm type K Inconel-sheathed thermocouples. Fabrication was normal, but final infrared inspection indicated that the transient heat flux profile was close to the ±5% maximum tolerance. Concentricity was excellent (no eccentricity was measurable throughout the heated length), final BN density was about 90% of theoretical and very uniform, and all electrical checks were normal.

However, because the transient heat flux profile was less uniform than expected, the cause of the variations was investigated further. The investigation revealed variations in cladding thickness of 7 to 10%. When these variations were eliminated by calculation from the infrared scans that were made during core and cladding transient tests, the profile appeared to be markedly improved.

To accommodate a previous change by GA in the cladding thickness from 0.7 to 0.5 mm, the wall thickness of our existing cladding had been suitably reduced by centerless grinding. Radiographs of these tubes, made after the wall thickness variation with GLR-L-7P was discovered, revealed that several tubes had very large variations in wall thickness, whereas others did not. The cladding used on prototype GLR-L-7P had been randomly selected from these tubes.

The GLR-L-7P was then installed in the HTS to (1) undergo long-term, steady-state testing; (2) evaluate the fast transient capability of CFTL (FRSs); and (3) observe the effects of thermal cycling, if any, on ratchetting of the FRS. The FRS was operated in the HTS for more than 1000 h at steady-state conditions and successfully completed about 1100 thermal transient cycles at various power and temperature levels. Tables 2 and 3 summarize these tests.

Steady-state operation, most of which was at 900°C, was completed and showed no degradation of heating element or BN insulation properties.

Table 2. Steady-state operational tests of GLR-L-7P

(Total steady-state operational hours = 1005)

Temperature (°C)	Duration (h)	Potential voltage (maximum)	Power (kW)
700	234	141	2.09
800	168	160	2.66
850	23	177	3.29
900	580	188	3.60

Table 3. Thermal cycling tests of GLR-L-7P

(Total thermal cycles = 1097)

Power (kW)	Rise time (s)	Hold time (min)	Power at hold time (kW)	Fall time (min)	Temperature change (°C)	Number of thermal cycles
3.40	90	3.0	3.4	1.5	350–870	202
3.40	90	9.0	4.4	1.5	350–870	339
13	12	4.74 (3.4 kW)	3.4	1.5	350–870	241
13	15	1.0 (5.6 kW)	5.6	1.75	350–1000	105
18	9	1.1 (5.6 kW)	5.6	1.75	350–1000	107
28 average (38 maximum)	6	1.1 (5.6 kW)	5.6	1.75	350–1000	103

This test series demonstrated adequately the capability of the prototypic swaged rod to meet the steady-state operation requirements of the first bundle.

Thermal cycling of GLR-L-7P ranged from low-power, relatively slow transients of 1.5-min duration in the temperature range from 350 to 870°C to high-power, relatively fast transients of 6- to 15-s ramp times in the temperature range of 350 to 1000°C. Although over one-half of the transients completed were relatively fast, the posttest electrical and infrared scan inspections showed no degradation of the power profile or of other FRS properties.

Length measurements indicated that the rod grew about 3 mm (0.120 in.), or about 0.2%. This growth, which is possibly but not necessarily caused by thermal ratchetting, had no adverse effect on rod properties.

However, the behavior of the four internal thermocouples indicated some problems. Two of the four failed before the 1000-h steady-state testing was completed, one at 263 h and one at 426 h. Both thermocouples had junctions located 150 mm above the lower end of the heating element.

The two thermocouples that survived the 1000-h testing exhibited erratic behavior early. One failed at 114 and the other at 170 cycles in the first 202-cycle test series. Both regained continuity when the rod was cooled to room temperature. Posttest evaluation showed that the grains in the Alumel thermoelement had grown enough to span the entire 0.075-mm-diam element cross section. Thermal expansion differences in the

Alumel and in the stainless steel cladding stressed the elements, causing boundary separation of the large grains.

Investigations of these and previous thermocouple failures resulted in (1) a much better understanding of failures and (2) major improvements in small-diameter thermocouple reliability. Chapter 5 reports on this effort.

After completion of steady-state and transient tests, GLR-L-7P was intentionally operated to destruction to define better the FRS low-power high-temperature maximum operation point. Table 4 summarizes this operation.

Table 4. Summary of GLR-L-7P final operation

Time (min)	Sheath temperature (°C)	Power (kW)
18	750	2.5
15	950	4.4
15	1000	4.9
25	1050	5.6
5	1100	6.4
5	1150	6.9
15	1200	8.5/6.5[a]
10	1250	7.1[a]

[a] Vacuum.

Failure occurred after 10 min of operation at 1250°C had been completed and while power was being increased to achieve 1300°C cladding temperature. The 316 stainless steel cladding and Nichrome V heating element melted in a region near the terminal end of the element. Subsequent analysis indicated that failure occurred in a 2.5-cm-long region at the upper (terminal) end of the heating element. The tantalum coating on the exterior of the rod cladding that was applied to enhance radiative heat transfer had not been properly extended during fabrication to cover the area that suffered the damage. The lowered emissivity in this area, compared with the rest of the heated section, resulted in the area reaching a temperature that was higher than expected or indicated.

In summary, the tests of prototype GLR-L-7P demonstrated that the swaged FRS is capable of long-time, steady-state operaton, of repeated thermal cycling, and of high-temperature low-power operation. The tests also identified weaknesses in thermocouple lifetime in the temperature range of 800°C and above and in thermocouple susceptibility to thermal cycling.

2.3 Phase II – Nonswaged FRS Development

The substantial deformation of cladding during swaging made the required cladding cold work difficult to achieve; at the same time, the tolerances on diameter, ovality, and straightness that are necessary to perform postswaging roughening of the cladding were difficult to maintain. Accordingly, we initiated the development of a nonswaged rod to overcome both of these difficulties.

A nonswaged FRS has several major advantages in addition to elimination of the swaging step:

1. elimination of the handling and shipping of rods to and from the manufacturer for roughening of the cladding,
2. cost savings by reduction in the number of FRSs having roughening defects,
3. improved final OD and straightness tolerances,
4. improved instrumentation and dimensional location of the heating elements,
5. FRS cladding cold work identical to that of the GCFR fuel rod cladding,
6. reduction in FRS fabrication costs, and
7. increased thermocouple lifetime.

The last advantage is crucial to long-term transient testing with the type K thermocouples installed in the FRSs that are used in CFTL test bundles. As reported, premature failure of FRS thermocouples occurred in most tests that used swaged rods.

However, a nonswaged FRS has two disadvantages compared with a swaged one. The nonswaged FRS will show some loss in uniformity of heat-flux profile, and it must be operated at lower maximum power for the same cladding temperature (assuming the same heating element material).

With the advantages and the disadvantages understood, a nonswaged FRS should satisfy three major criteria:

1. Heat flux profile, as defined by infrared temperature measurement, in a 1-s core transient should be within ±5%.
2. A reasonable thermal conductivity of the outer annular BN must be attained so the FRS can achieve the CFTL power-temperature requirements.
3. Most of the internal thermocouples must be able to withstand the thermal transients imposed upon them without premature failure.

These criteria (which also apply to the swaged FRS) guided the development of the nonswaged FRS described in this section.

Prototype GNR-L-8P was the first nonswaged FRS to be fabricated. Several improvements were incorporated into the fabrication technology. The major improvements were the use of (1) high-energy (70-kJ/m^2) crushing techniques in filling the inner preforms and (2) annular preforms with an initial density of 1.8 g/cm^3 that is 80% theoretical density (TD).

The resultant preform density (after fill) of the volume between the coil and the nickel rod (inner annulus) was 1.82 g/cm^3 compared with 1.6 to 1.7 g/cm^3 for previous swaged prototypes after filling and prior to swaging. The higher density of the inner annulus preforms, combined with a preform density of 1.85 g/cm^3 in the volume between the heating element and the cladding (outer annulus), made the concept of a nonswaged FRS feasible for the first time. Because the thermal conductivity of the BN powder is a strong function of density, a minimum of 80 to 85% of TD is necessary to achieve a moderately high heat flux (100 to 200 W/cm^2).

The transient infrared scan variation of prototype -8P was a disappointing ±16.7%. This poorer-than-expected result using relatively high-density preforms made of grade HCM BN powder* caused us to investigate

---

*HCM and other BN powders such as TS-1325 are designations or trademarks of Union Carbide Corporation, Carbon Products Division.

the usefulness of several other BN powders. Table 5 summarizes pertinent properties of these powders.

The known higher final density of the HCM grade of BN powder led to its initial selection as the major candidate for nonswaged FRSs because greater profile uniformity and higher thermal conductivity were expected to accompany higher density. Table 5 reveals, however, that this assumption was not valid. Although higher preform density is possible with HCM powder, the much larger particle size reduces strength and impedes achieving intimate contact with the ID of the cladding (analogous to the degree of surface contact of gravel vs sand in a glass jar). Better thermal contact with the cladding for preforms made of both TS-1325 powders is indicated by their strength. Relative strength for all three preform materials was based on the difficulty of removing the crushed powder from the annular area. Core transient infrared scan data also indicated enhanced

Table 5. Property evaluation of several types of BN preforms

Powder	TS-1325		HCM die-body lubrication
	1/2-1/2 lubrication[a]	1 camphor lubrication[b]	
Powder particle size, µm	7–20	7–20	50–750
After pressed density, g/cm^3 (%)	1.84 (82)	1.86 (83)	1.94 (87)
After purified density, g/cm^3 (%)	1.58 (70)	1.76 (78)	1.89 (84)
After filled density, g/cm^3 (%)	1.69 (75)	1.85 (82)	1.89 (84)
After filled strength	Strong	Very strong	Weak
Transient infrared scan profile deviation, %	±5–7	±3–4	±5–10

[a] 1/2% dodecane–1/2% dodecanol by weight in BN.

[b] 1% camphor by weight in BN.

contact of the TS-1325 powders but showed that final density is also a factor. From these data, preforms made of camphor-treated TS-1325 powder were determined to be the best candidates for a nonswaged FRS.

Preforms fabricated of camphor-lubricated grade TS-1325 BN powder were used in the fabrication of prototype GR-L-9P. Although this prototype was subsequently swaged, it served primarily to evaluate TS-1325 camphor preforms and the newly developed techniques for crushing inner annulus preforms. This was also the first FRS to be fabricated with a variable width Nichrome V heating element.

During filling of the preforms in the outer annulus, the internal thermocouples became crossed. Attempts to uncross them were unsuccessful, so the terminal region was cut to within 7.5 cm of the heating element to eliminate the crossed section. Although the shortened length precluded testing the rod in the SRSL, all the other physical, electrical, mechanical, and infrared scan evaluations were acceptable.

Radiographic examination of the rod indicated that the upper 2.5 cm of the variable width heating element stretched more than was anticipated and thus caused the turns to become distorted and the coil diameter to increase. Although this result has little effect on profile uniformity, the change in heating element diameter caused binding of the preform tamping tool, which subsequently led to the crossing of the thermocouples. The additional movement of the heating element turns resulted from use of the camphor-treated TS-1325 BN powder. Crushing of the TS-1325 preforms individually in the rod during fabrication caused a 3 to 4% density increase compared with no measurable increase in the previous use of HCM preforms. This density increase was accompanied by greater axial movement of powder and, therefore, of the heating element. Although the incremental heating element movement per preform crushed was small (~0.05 to 0.1 mm per 15 mm preform), it resulted in disturbing the last three or four turns of the heating element and the subsequent binding of the tamping tool.

The infrared scan, although skewed because of coil movement, indicated that local variations were within the ±5% requirement of criterion 1. This result was the first positive indication that the newly developed fabrication techniques and the camphor-treated TS-1325 preforms might yield an acceptable nonswaged FRS.

Although prototypes GNR-L-8P and GR-L-9P were primarily associated with development of the nonswaged FRS, prototype -10P was of the swaged design. Although neither -8P or -9P was operated, several major fabrication innovations that were developed with them were applied to prototype GR-L-10P. It, in turn, led to the solution of a fabrication problem affecting both swaged and nonswaged rods. Rod -10P was successfully fabricated, but problems were encountered with metal spalling from the copper center terminal. The braze connection of the nickel-copper rods left the copper very soft. The action of the preform tamping tools caused copper to spall off into the inner annulus during preform filling. The problem was corrected by an elongation of about 1%, which hardened the copper rod sufficiently to prevent further metallic spalling. This simple but effective way of eliminating copper spalling was incorporated into the evolving fabrication procedure for subsequent FRSs.

The GR-L-10P prototype was tested in the SRSL; it was gradually brought up to 29.9 kW at a cladding temperature of 715°C. Operation at these conditions was sustained for 47.5 h until the crowbar protection system terminated the tests. Radiographic examination revealed that an insulation breakdown had occurred in the terminal region 250 mm above the top of the heating element, the region where copper spalling had occurred during fabrication. Even though it was known that a filling problem had occurred, the radiographic and insulation checks appeared to warrant operational testing. This result emphasizes how critical the fabrication process is to subsequent proper operation of an FRS.

Because of the success of the nonswaged development, GR-L-10P was the last swaged prototype to be fabricated. The information gain from fabrication and operation of -10P was successfully applied to subsequent nonswaged prototypes. Additionally, the elongation test provided a key to the solution of the perplexing problem of obtaining a practical inspection of the rod and tubular braze joints between the copper terminals and nickel leads.

Nonswaged prototypes GNR-L-11P and -12P were then fabricated by using the information gained on FRSs -8P and -9P. Some binding between the heating element and the tamping tool was encountered on −11P, but the prototype was successfully fabricated. Fuel rod simulator −12P was filled after further modifying the fabrication procedure to allow extension of the internal thermocouples beyond the exit at the closed end of the FRS. Annular preforms were then filled from each end of the longitudinal center of the heating element; the previous, normal procedure had been to fill all preforms from the terminal end only. The new filling procedure allowed use of tamping energies of 70 $\mathrm{kJ/m^2}$ during both inner and outer preform crushing and eliminated the binding problem that was encountered previously with TS-1325 preforms.

Nonswaged prototypes −11P and −12P both met all postfabrication inspection requirements, including being within the allowable ±5% tolerance on heat flux profile uniformity. However, swaged prototype −10P had met criteria 1 and 2, but not 3, prior to failure, and nonswaged rods were yet to be tested for meeting criteria 2 and 3.

Thus, GNR-L-11P would be tested in the SRSL to determine how well it met criterion 2. Because of the lower BN density in a nonswaged FRS compared with a swaged FRS and the resultant reduced contact pressure between BN and cladding, we anticipated that the effective thermal conductivity of the BN would be lower, possibly by a factor of 5. Thus, maximum power operation might be limited to about 10 kW at 1000°C sodium stream temperature. Table 6 summarizes these tests and indicates that higher-than-anticipated thermal conductivity was achieved.

Failure occurred as a result of the melting of the Nichrome V heating element [T_{mp} I, ~1400°C] about 250 mm from the end of the heating element, nearer to the closed end of the FRS. The location is in the region of the maximum expected temperature, based on a cosine heat generation profile and the sodium coolant temperature at that point. Melting at that point is a strong indication of uniform BN properties. By using the local heat flux and temperature conditions, we found the calculated BN thermal conductivity to be about one-third of that evidenced by a fully swaged FRS. Based on the calculated BN conductivity, the physical dimensions of the FRS, and a maximum safe heating element temperature of 1300°C, an anticipated operation curve for the nonswaged FRS (Fig. 3) was obtained.

Table 6. SRSL operational tests of GNR-L-11P

Power[a] (kW)	Sodium stream temperature (°C)		Time (h)
	Inlet	Outlet	
20	445	620	5.0
20	550	825	1.0
24	650	1000	2.0
28	550	1000	1.5
29	550	1000	1.5
31	550	1000	1.3
34	550	1000	0.7[b]

[a] Power data do not include 2% of power dissipated in terminals.

[b] Failure occurred.

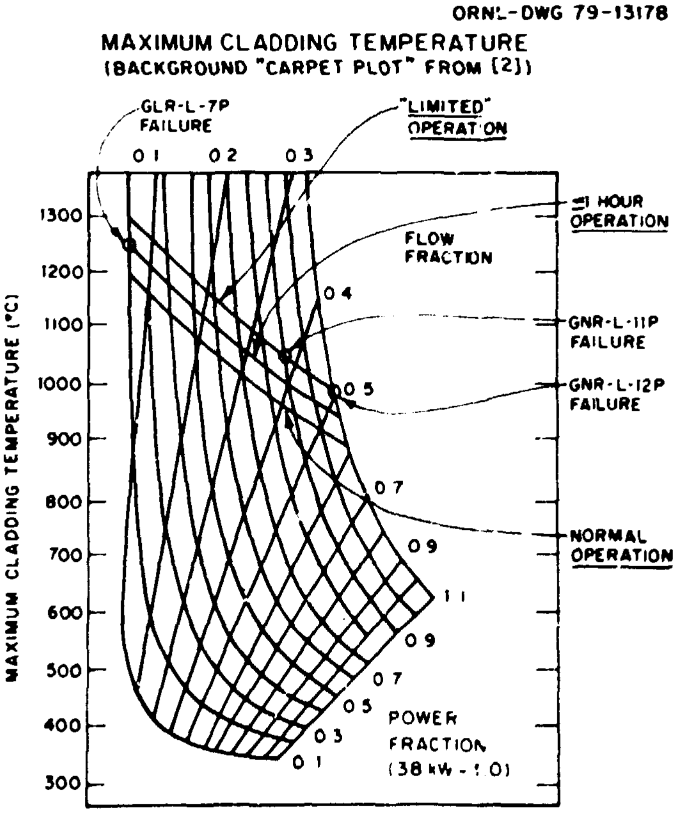

Fig. 3. Maximum expected operating capability of CFTL FRS.

Figure 4 is a plot obtained from V. Casal, Kernforschungsventrum (KfK), Karlsruhe, Germany, of BN thermal conductivity k vs density ρ for a powder-filled FRS. The calculated thermal conductivity for GNR-L-11P is also plotted. Two items of interest are (1) the Casal data show that k is strongly dependent on ρ for ρ > 70% and (2) the conductivity for -11P is approximately double the Casal anticipated value at the 83% density. This

ORNL-DWG 79-13170

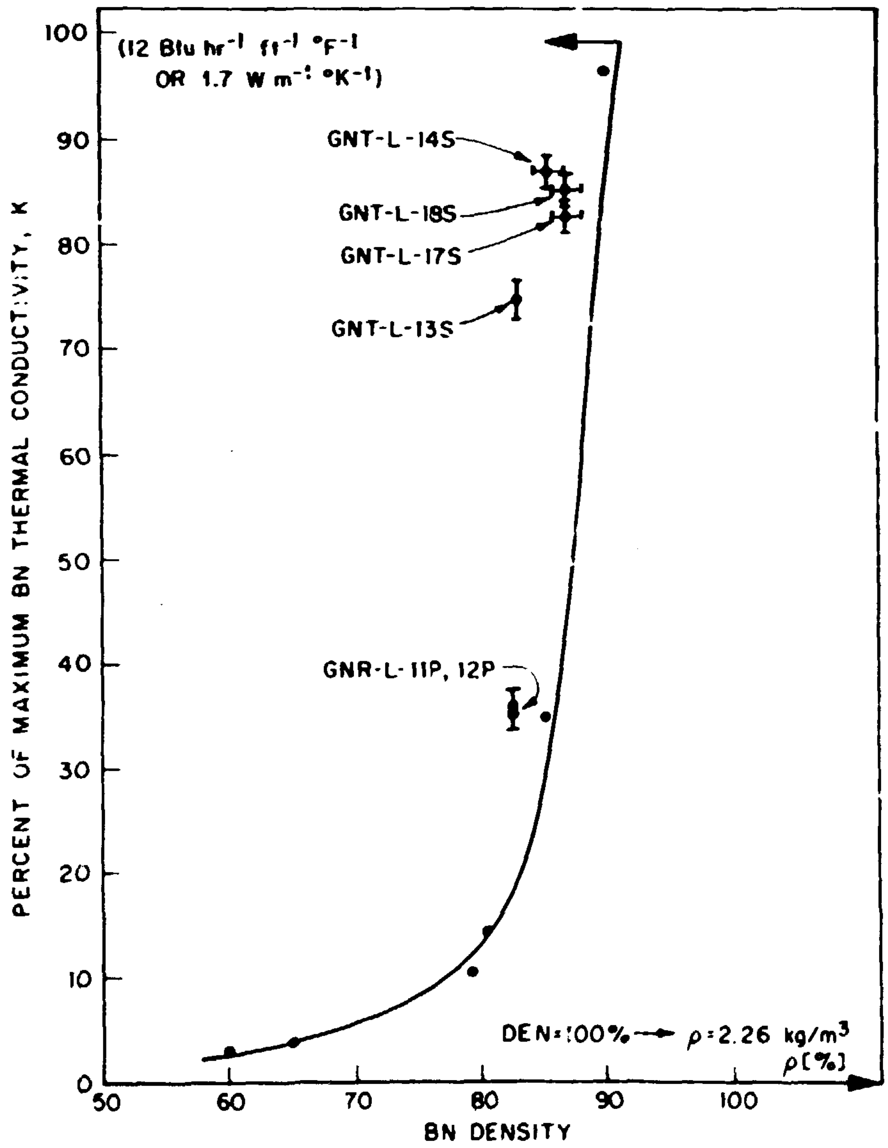

Fig. 4. Thermal conductivity as a function of BN density for CFTL FRSs and thermal conductivity cells vs German powder-filled FRSs.

higher-than-anticipated conductivity is probably the result of a high degree of radial orientation that was achieved with cold-pressed preforms; the Casal data are for random-to-axial favored orientation. The data also appear to indicate that an increase of about 5 to 7% in as-filled preform density in an unswaged FRS may yield values of BN thermal conductivity nearly as high as those for a fully swaged FRS.

Based on this information, we initiated plans to fabricate a series of thermal conductivity cells for further investigation of the thermal conductivity vs the density relationship of BN preforms. Meanwhile, prototype GNR-L-12P was installed in the SRSL for tests. Our intent was to qualify the nonswaged FRS at 110% power (42 kW) and 1000°C and to determine its thermal cycling capability. Table 7 summarizes this test operation.

Prototype GNR-L-12P survived more than 700 h of tests, endured more than 2150 thermal transients, and operated at 110% of design power and at 975°C cladding temperature before failure. The initial larger part of the operation, 693 h, was at steady-state test conditions that were similar to those expected in many of the CFTL bundle tests. The rod was then subjected to thermal transients that approximately simulated those anticipated in CFTL tests in number and duration. At the completion of these steady-state and transient tests, both prototype -12P and three of the four internal thermocouples were still operational. The remaining internal thermocouple broke at the terminal end during installation of the FRS in the test loop. Posttest continuity checks indicated that this thermocouple was also still operational.

Fuel rod simulator -12P was then intentionally operated at conditions approaching expected failure. Failure occurred within about 25°C of the predicted failure of 950°C at 42 kW. Worth noting is that, in both this test and in that of GNR-L-11P, operation was normal up to the point of melting the Nichrome V heating element. This result indicates that the electrical resistance of the central BN preforms is adequate for operation up to about 1400°C without failure. The central annular BN preform had previously been perceived to be one possible weak point in FRS ability to operate at high temperatures.

Table 7. Summary of test results for nonswaged rod GLR-L-12 in SRS6

Test No.	Operation method[a]	Power			Maximum cladding temperature (°C)	Transient ΔT (°C)	Period (min)	Number of cycles (required/completed)	Total tim (h)
		Total kW	V	A					
1	SS	29.4	261	113.3	760				693
2	Tran.	29.0	260	112.0	760	236	1.0	0/305	5.10
3	Tran.	30.5	265	116.0	760	56	1.0	150/184	3.10
4	Tran.	30.5	265	116.1	760	255	2.0	20/241	8.0
5	Tran.	31.0	266	117.0	760	114	2.0	1200/1420	47.3
6	Tran.	31.0	266	117.0	760	250	2.0	0/34	1.0
7	SS	28.8	255	113.0	710				0.25
8	SS	34.6	280	123.5	800				0.08
9	SS	39.4	300	131.5	900				0.02
10	SS	43.4	315	137.8	900				0.58
11	SS	45.0	322	140.0	900				0.28
12	SS	43.3	315	136.0	900				0.08
13	SS	43.3	315	136.0	932				0.67
14	SS	43.3	315	136.0	968				0.17
15	SS	43.3	315	135.8	972				0.37
15	SS	43.3	315	135.8					

[a] SS = steady-state operation; Tran. = transient operation.

The radial temperature difference (ΔT) between the sodium stream and the internal thermocouple indications was higher in a nonswaged than in a swaged FRS. An average ΔT of 115°C that was measured at 30 kW and 760°C sodium outlet temperature in nonswaged prototypes GNR-L-11P and -12P compares with 78°C for swaged prototype GR-L-10P that was measured under the same conditions. The large ΔT for a nonswaged FRS was expected and is attributed to the lower BN thermal conductivity and the lower contact pressure between the heating element and the stainless steel cladding and thermocouples that is caused by the elimination of swaging during fabrication.

2.4 Phase III – Conductivity Cell Fabrication and Testing

A series of conductivity cells was fabricated and tested to obtain information about the effective thermal conductivity of the crushed cold-pressed BN preforms in an FRS. Information was needed on the relationship of conductivity to inner and annular BN density, FRS power, cladding temperature, and the fabrication process. Test cells were a simple, effective means of obtaining this information. Nine test cells were fabricated in parallel with the last two phases of FRS development, and information gained from them is summarized in this section.

The conductivity cell configuration is similar to that of the CFTL FRS (Fig. 2) except that it has a heated length of 30.5 cm and the center terminal (current return) is replaced with a 1.5-mm thermocouple. The current return is provided by attaching the far end of the heating element to the cell cladding and grounding the cladding to complete the electrical circuit. Some cells contain the FRS sheath thermocouples, and some do not (Table 1).

A Water Cooled Test Stand (WCTS) was fabricated to test the cells. Each test cell was mounted horizontally in the WCTS. Two or three thermocouples were attached to the outer cladding surface in an intrinsic junction configuration. All junctions were located in the radial plane that contains the junction of the central thermocouple and at equidistances around the perimeter.

Figure 5 summarizes thermal conductivity k vs power for the WCTS tests of the conductivity cells. The data were repeatable to within ±10%. Pertinent information gleaned from the conductivity cell tests includes:

1. Thermal conductivity k is sensitive to the differential thermal expansion of the heating element and the BN insulation.

2. In test cells -13S–18S, thermal conductivity reached a maximum value of about 80% of that achievable with a powder-filled swaged rod, cells -20S and -31S demonstrated a thermal conductivity about equal to that of a powder-filled swaged rod, and -30S achieved a value about equal to swaged, BN preform rods.

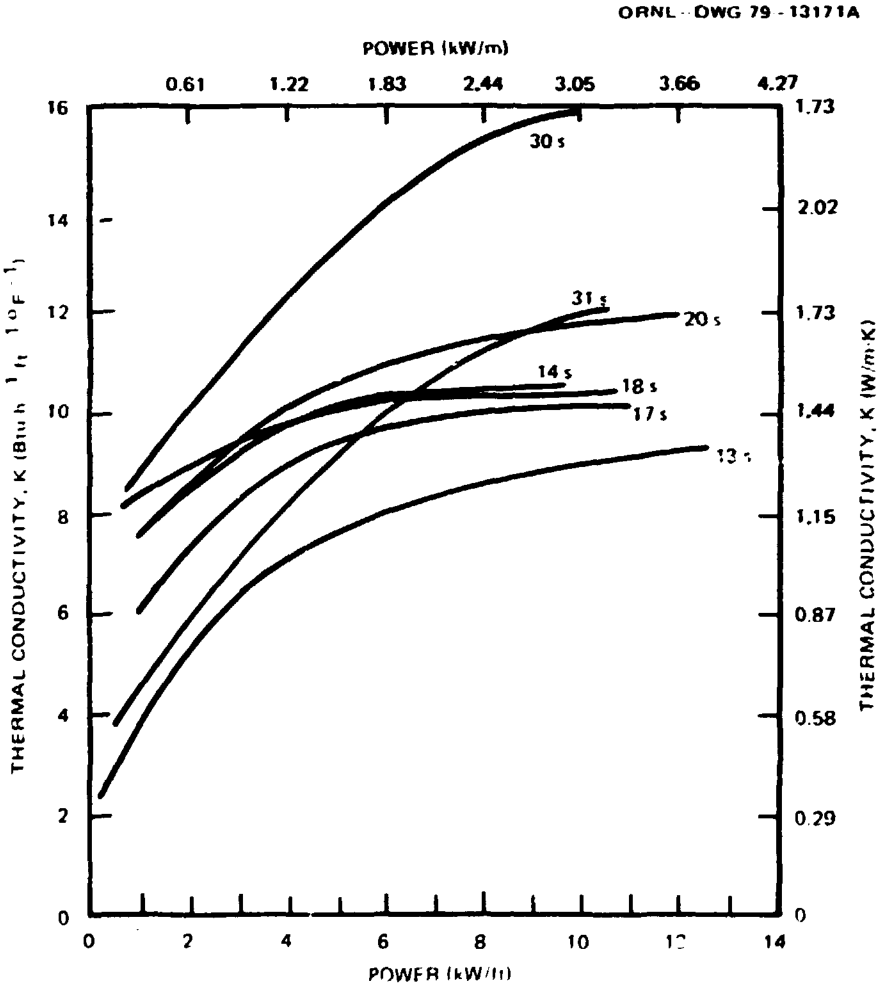

Fig. 5. Thermal conductivity as a function of power for several conductivity cells tested in the CFTL WCTS.

3. Thermal conductivity is sensitive to the density of both the inner and outer annular preforms. The degree of the dependence is not clear, but the major dependence appears to be on the outer annulus preforms.

4. The value of thermal conductivity as a function of density is always higher for the conductivity cells than is the value from the Casal[8] data for powder-filled FRS (Fig. 4).

The cladding was held at an approximately constant temperature in the boiling water in the WCTS. The cell center temperature, measured with the central thermocouple, varied with heat flux and reached temperatures as much as 250°C higher than the heat sink temperature at the high heat flux values. The thermal expansion associated with this radial ΔT tightens up the internal cell components and increases the contact pressure between the heating element BN and the internal surface of the cladding. The leveling off of the thermal conductivity vs power (heat flux), because of internal thermal expansion, indicates the maximum effective thermal conductivity that we achieved.

The variations in k from test cell to test cell were primarily caused by annular BN preform density. Test cell -30S, fabricated with TS-1449 powder, had the highest annular density of ~90% TD. Orientation also has a contributory effect but appears less important. Chapter 3 discusses BN preforms in detail.

Test cells GNR-L-19S and -20S were fabricated primarily to evaluate the effects of fabrication techniques and inner preform material on the effective outer annular thermal conductivity.

Cell -19S was fabricated to be similar to -17S and -18S but with a Kanthal A-1 heating element. The newly developed Kanthal-to-nickel laser butt weld, joining the heating element to the tubular terminal, was evaluated from both fabrication and operational standpoints. The test cell was successfully fabricated and tested in the WCTS. The weld joint endured several hundred severe thermal transients without failure or degradation. On the basis of this question, the decision was made to fabricate several Kanthal A-1 elements for full-length prototypes.

Test cell GNT-L-20S also contained a Kanthal heating element but was primarily fabricated to test newly developed 85% MgO-BN central preforms, The hybrid preforms were intended to provide increased internal thermal expansion and thus increase the thermal conductance at the outer annular preform interfaces. The preforms were developed and fabricated locally and contained BN only to increase their pressability. The postpurification strength was less than that previously experienced with BN preforms but was adequate for fabrication.

Figure 5 demonstrates the increase in effective annular BN thermal conductivity of test cell -20S by comparison with a similar test cell, -14S, which contained central BN preforms but equivalent annular preforms. An increase in thermal conductivity of 10 to 15% is evident for cell -20S, indicating that the MgO-BN preform is effective. However, low-power thermal conductivity is still relatively low, and the maximum values obtained are less than those measured for the swaged construction. Although the use of MgO-based central preforms improves operational conditions, this improvement alone apparently will not increase maximum power for the nonswaged FRS sufficiently to match that of the swaged FRS.

To investigate further the dependence between thermal conductivity and operating conditions, conductivity cell GNT-L-14S was tested in the SRSL to higher temperatures than achieved in the WCTS. Figure 6 summarizes the test results. Although the value of thermal conductivity was reasonably constant as a function of power, it decreased with increased cladding temperatures. The thermal expansion of the stainless steel cladding apparently offsets the salubrious effects of the thermal expansion of the FRS internal components and, thus, lowers the effective thermal conductivity.

2.5 Phase IV - Extension of FRS Capabilities

The successful fabrication and operation of nonswaged FRSs GNR-L-11P and GNR-L-12P and the good nonswaged annular thermal conductivity demonstrated with the test cells led to the program decision to use the nonswaged FRS as the reference design. However, some sacrifice in uniformity of heat-flux profile occurs during a power transient, as indicated by infrared scan and by rod reliability. Additionally, some reliability is

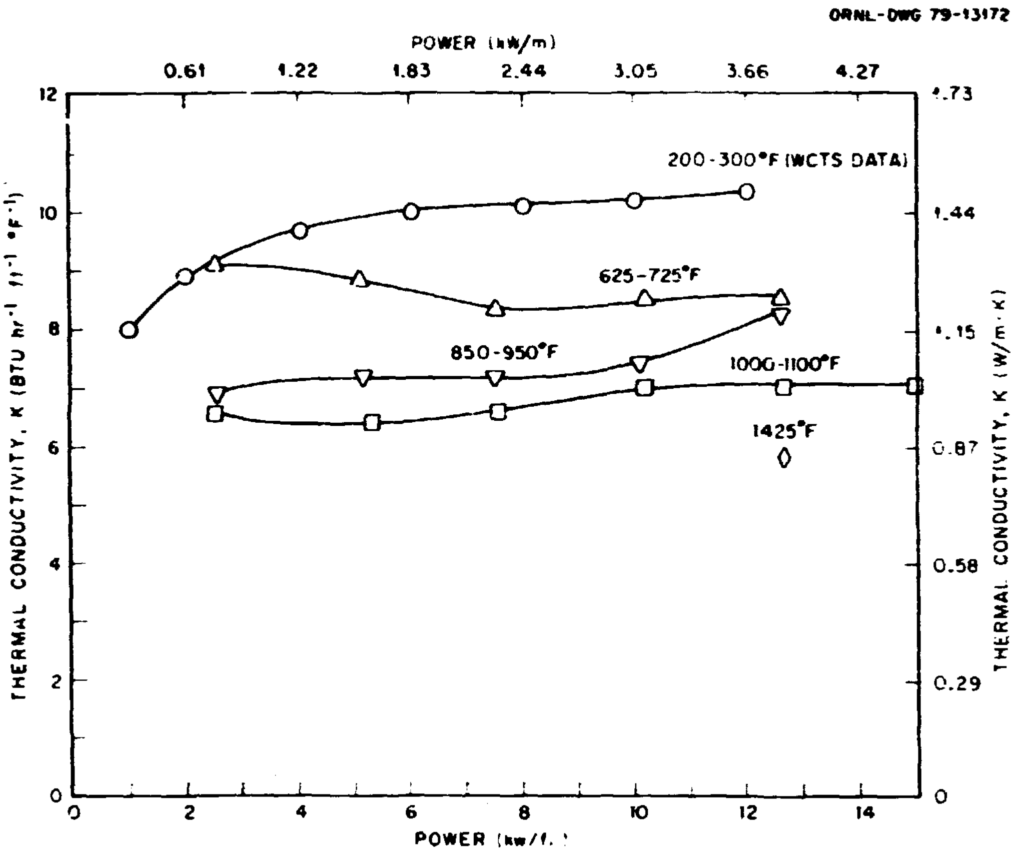

Fig. 6. Thermal conductivity as a function of power at several different temperature levels for CFTL conductivity cell GNT-L-14S.

sacrificed because the heating element reaches necessarily a higher temperature in the nonswaged FRS for a given operating condition when compared with the swaged FRS. Both sacrifices are the direct consequence of reductions in the thermal conductivity and in the density of BN that can be achieved with a nonswaged FRS.

However, areas where both operational capability and reliability of the nonswaged FRS can be improved are:

1. increase in BN preform density and consequent thermal conductivity,
2. further improvements in fabrication techniques, and
3. the use of Kanthal A-1 instead of Nichrome V as the heating element material.

Items 1 and 2 were investigated through the fabrication and testing of thermal conductivity cells, reported in Sect. 2.4. Item 3 is the subject of prototype GNK-L-15P and -16P (the K in GNK denotes a Kanthal A-1 alloy heating element).

Prototypes -15P and -16P were fabricated primarily to test the capability of the Kanthal material to withstand the fabrication operations and the thermal cycling of CFTL FRSs. The postfabrication inspections of prototype -15P revealed that the laser weld joint between the Kanthal heating element and the associated tubular nickel lead had failed. Although previous weld tests with Kanthal had been successfully completed, the new procedure was obviously not successful with prototype -15P.

Prototype -16P, which contains a constant width heating element made of Kanthal A-1 alloy, was fabricated successfully. Extensive prefabrication testing of the weld joint at the nickel-Kanthal interface proved it to be very durable. The prototype was tested in the HTS; Table 8 summarizes these tests.

The primary intent of the -16P tests was to determine the stability of the laser-welded butt joint between the Kanthal and the adjoining nickel tube under high thermal stress conditions. Thermal transients were conducted in which the rise rate and then the cladding temperature were

Table 8. Summary of rod GNK-L-16P operational tests in the HTS

Test	Power (kW)	Maximum cladding temperature (°C)	Transient ΔT (°C)	Period (min)	Number of cycles	Total time (h)
1	2.3	730	380	3.0	81	4.05
2	3.5	870	520	3.0	112	5.60
3	6.0	860	520	3.0	70	3.50
4	6.0	1010	675	3.0	42	2.10
5	7.5	1065	705	3.0	160	8.00
6	7.6	1075	705	3.0	224	11.20
7	1.8	700	*a*			11.00
8		1180	*b*			1.0+

[a] Steady state.

[b] Slow increase to failure.

increased with each test. The second objective was to determine thermocouple lifetime under relatively large and rapid thermal transient conditions, such as in tests 2–7.

The Kanthal-nickel tube butt weld operated normally through 689 transients and 46.5 h of operation before failing. The weld area has been sectioned and analyzed to obtain more detailed information. Its successful operation throughout the severe transients and the results of the metallurgical examination indicate that the weld is reliable enough to permit the use of Kanthal A-1 heating elements in GCFR-CFTL FRSs.

Rod GNK-L-16P contained three modified-grounded-junction thermocouples and one grounded-junction thermocouple. Table 9 lists the cycles to failure of each.

The thermal transients in the -16P tests were more severe than those anticipated in the first CFTL test bundle. The failure of all three modified-grounded-junction thermocouples before failure of the grounded-junction type is an indication that the modified-grounded junction is less reliable than the grounded junction. The modified-grounded junction is a low-mass junction that is welded directly to the cladding and, hence, should experience the effects of differential thermal expansion more directly than the grounded-junction thermocouple. However, insulated-junction thermocouples have been shown to be the most reliable, possibly because additional thermal shock resistance is supplied by the insulator material.

Table 9. Rod GNK-L-16P thermocouple transient cycles before failure

Thermocouple	Junction type	Cycles to failure
1	MGJ[a]	305
2	MGJ	347
3	MGJ	505
4	GJ[b]	684

[a] Modified-grounded junction.

[b] Grounded junction.

A series of six rod prototypes, GNK-L-21P through -26P, were fabricated and tested. Prototypes -21P, -23P, and -25P were tested in the HTS while -22P, -24P, and -26P, were tested in the SRSL.

Tests in the HTS were intended to (1) determine the reliability of rod internal thermocouples under thermal transient conditions, (2) determine the capability of an FRS to withstand 1000 to 1200°C operation, and (3) determine if operation of the FRS was possible at or near the melting temperature (1375°C) for the cladding.

All prototypes contained Kanthal A-1 heating elements, and all heating elements were variable width except that of -21P. Table 1 summarizes the pertinent components of each prototype.

Tables 10 and 11 summarize the steady-state and transient operations, respectively, of the three rod prototypes tested in the HTS.

Rod GNK-L-21P survived 309 h of steady-state tests, including over 40 h at 1100°C, and successfully completed almost 4000 thermal cycles typical of or more severe than those expected in CFTL operation. Although the thermocouples began to experience errors as the testing progressed, none failed because of thermal element grain growth and thermal expansion induced strains. This was significant and demonstrated that, in the nonswaged rod, thermocouples are far less susceptible to these modes of failure. The Kanthal-to-nickel laser butt weld also successfully survived all operational tests.

At one point during tests of rod -21P, rod power was inadvertently increased from near 5.5 to 15 kW for 9 s while operating at 1100°C cladding temperature. Although all thermocouples went off scale, the cladding temperature was estimated to have reached 1350°C. The internal temperature of the nickel rod almost surely reached the melting point during this excursion, although no evidence of damage could be detected with electrical checks. However, the rod failed later while being operated at 1100°C cladding temperature for thermocouple calibration checks. Failure occurred by melting of the cladding at several places along the heated length, indicating severe temperature variations.

The tests conducted on GNK-L-23P were approximately the same as those conducted on GNK-L-21P. A total of 284 h of steady-state operation was logged, 32 h at 1100°C cladding temperature. Nearly 5000 thermal cycles

Table 10. Steady-state operation of rod prototypes in the HTS

Rod	Power (kW)	Maximum cladding temperature (°C)	Time (h)	Medium
GNK-L-21P	1.9	700	125	
GNK-L-21P	3.1	870	121.5	
GNK-L-21P	4.4	1000	19	
GNK-L-21P	5.5	1100	40.5	
GNK-L-21P	6.8	1200	1	
GNK-L-23P	0.2	350	1	
GNK-L-23P	1.5	700	119	
GNK-L-23P	2.4	870	23	
GNK-L-23P	2.7	930	90	
GNK-L-23P	3.4	1000	19	
GNK-L-23P	4.6	1100	32	
GNK-L-25P	1.6	700	95	Vacuum
GNK-L-25P	2.6	820	0.033	Vacuum
GNK-L-25P	3.0	920	0.02	Vacuum
GNK-L-25P	3.4	995	0.03	Vacuum
GNK-L-25P	3.7	1102	0.03	Vacuum
GNK-L-25P	4.0	1220	0.05	Vacuum
GNK-L-25P	4.2	1310	0.03	Vacuum
GNK-L-25P	4.3	1380	0.03	Vacuum
GNK-L-25P	4.7	1400	0.02	Vacuum
GNK-L-25P	1.6	700	3	Helium
GNK-L-25P	2.2	795	0.025	Helium
GNK-L-25P	3.1	905	0.05	Helium
GNK-L-25P	4.2	1005	0.08	Helium
GNK-L-25P	5.5	1100	0.02	Helium
GNK-L-25P	6.2	1200	0.02	Helium
GNK-L-25P	7.2	1250	0.03	Helium
GNK-L-25P	7.4	1260	0.03	Helium
GNK-L-25P	7.9	1300	0.02	Helium

were completed with no damage to the FRS and no failure of the thermocouples. The rod failed after 32 h at 1100°C operation. Failure was apparently caused by a decreasing value of cladding emissivity caused by breakdown of the tantalum coating. Without the tantalum coating, "thermal polishing" of, and consequent high temperatures in, the stainless steel cladding can occur within a matter of minutes. Failure analysis of the thermocouples indicated that both Chromel and Alumel thermoelements were

Table 11. Transient operation of rod prototypes in the HTS

Rod	Power (kW)	Maximum cladding temperature (°C)	Time (h)	Cycles	Transient ΔT (°C)
GNK-L-21P	0–3	750	106.6	3425	330
GNK-L-21P	0–7	870	6.2	371	345
GNK-L-21P	0–14.9	950	2.5	150	450
GNK-L-21P	0–14.9	1300	0.02	1	350
GNK-L-23P	0–1.5	750	2.3	68	325
GNK-L-23P	0–3	750	10.7	640	200
GNK-L-23P	1–2	750	134.0	4020	150
GNK-L-23P	0–1.5	750	0.8	22	330
GNK-L-23P	0–6	870	3.8	230	320
GNK-L-25P	0–1.6	700	3.3	200	350

ductile, even though grains were large, as were the thermoelements in rod prototype GNK-L-21P, which underwent similar tests.

The primary intent of tests on rod prototype GNK-L-25P was to obtain operational data at temperatures approaching the melting point of the cladding. Approximately 100 h of steady-state operation at 700°C was logged to ensure that the rod was reliable before approach-to-melting of the cladding (ATCM) tests were run. All thermocouples were operational at the start of the tests.

Two test series were run. The first (see Table 10) involved operation in vacuum from 700 to 1380°C (as measured by a type S thermocouple welded to the cladding). Power was increased stepwise to provide temperature increases of about 100°C. Measured cladding temperature increased incrementally to 1400°C. At this point, the rod lost power, apparently because of an open circuit. We subsequently determined that an over-temperature switch, set at 1400°C, had terminated the test. A total operational time of 11 min from 1000 to 1400°C was sustained without damage.

The second test series involved operation from 700 to 1300°C in low-pressure (~70 kPa) helium (Table 10). A total operational time of 11 min at temperatures from 1000 to 1300°C was sustained before failure occurred at 7.9 kW and 1300°C cladding surface temperature. Because of the helium environment, the power at the highest temperature was twice that in the previous vacuum test.

Failure in rod -25P was caused by the melting of the nickel center rod. The increased heat flux, compared with the vacuum test, raised the rod internal temperature sufficiently to cause the nickel to melt ($T_m \approx 1425$°C) at a cladding temperature of 1300°C. These tests indicate stable operation to cladding temperatures approaching 1300°C at power levels larger than anticipated for GCFR depressurization tests.

High-temperature and transient tests on these three prototypes verified that operation in the 1000 to 1200°C regime is possible and that very limited operation is possible up to and including melting temperature of the cladding.

No rod internal thermocouples were lost during testing, although all three prototypes encountered conditions more severe than anticipated in the CFTL. Failure analysis of thermocouples in the prototypes indicated that, unlike the thermocouples in swaged prototypes that encountered similar testing, the thermoelements were very ductile. This is despite the fact that grains were very large and often traversed the entire cross section.

This serendipitous, but unexplained, phenomenon was discussed with Dr. Brian Ralph from Cambridge University, England, during his visit to ORNL in 1979. He is a metallurgist who has spent considerable time examining material grain boundaries and materials properties associated with them. Consulting with Dr. Ralph during his brief visit led us to suspect strongly that void growth during FRS testing, caused by levels of 5 to 10% cold work (prestrain) either residual from thermocouple fabrication or put into the thermocouples during FRS fabrication, is responsible for the brittle behavior of thermocouples in previously tested swaged rods, such as -7P.

Apparently, when the thermocouples are strained (by FRS swaging, pulling to straighten, or other causes), microcracks appear around material inclusions. These sites result in the nucleation and growth of voids later during high-temperature operation, which causes material recrystallization. The voids form at grain boundaries, reduce the grain boundary cross section, and drastically weaken the material. Although lower levels of prestrain (<1%) associated with nonswaged rods probably result in a minor degree of microcracking, they apparently do not add enough energy to the system to induce void nucleation and growth. Thus, it appears that the major necessary ingredient for successful long-life high-temperature operation of 0.5-mm type K thermocouples is simply to keep the prestrain levels <1 or 2%, which is intrinsic with the nonswaged rod design.

Results from testing rod prototypes -22P, -24P, and -26P in the SRSL were not as encouraging as those obtained with HTS operation of -21P, -23P, and -25P. Tables 12 and 13 summarize the steady-state and transient test operations, respectively.

Rod GNK-L-22P endured 928 transient cycles and operated a total of 247.5 h at steady state before failure. Most transient cycles were from 350 to 600°C sodium temperature (365 to 650°C cladding temperature) and of 1 to 2 min with step changes in power between 18.8 and 41 kW. Most of the steady-state operation was at 30 kW and 650°C maximum cladding temperature.

The rod failed when being cycled from 0 to 30 kW at 1000°C cladding temperature. Failure was caused by a crack in the nickel center conductor

Table 12. Steady-state operation of rod prototypes in the SRSL

Rod	Power (kW)	Maximum cladding temperature (°C)	Time (h)
GNK-L-22P	20	650	25
GNK-L-22P	30	650	221.4
GNK-L-22P	30	1000	1.0
GNK-L-24P	8.5	500	3.0
GNK-L-24P	8	500	1.0
GNK-L-24P	20	650	0.5
GNK-L-24P	30	750	0.5
GNK-L-24P	38.5	710	8.8
GNK-L-26P	10.6	750	2.0
GNK-L-26P	19.1	750	10.5
GNK-L-26P	28.7	780	21.0

Table 13. Transient operation of rod prototypes in the SRS6

Rod	Power (kW)	Maximum cladding temperature (°C)	Time (h)	Cycles	Transient ΔT (°C)
GNK-L-22P	19–41	600	23.1	925	250
GNK-L-22P	0–30	1000	0.05	3	300
GNK-L-24P	0–30	750	5.5	495	300
GNK-L-26P	0–19.1	750	3.3	290	250

at about 25 mm (1 in.) from the ground end of the heating element. Apparently, the combination of rapid rise in power and cladding temperature brought the nickel rod to the point of failure. The four type K, insulated-junction thermocouples endured all the thermal transient operations without failure.

Fabrication problems had occurred at the ground end of the heating element with -22P. The variable width Kanthal A-1 heating element is very strong at room temperature and difficult to work. The fabrication process required that the nickel end plug, inserted before the inner BN preforms were installed, should be removed after preform installation to permit electrical checks. The removal and reinsertion of the end plug proved to be difficult, disturbing the adjacent BN preforms and causing loss of density and good heat transfer contact.

Although the fabrication procedure was modified, essentially the same conditions were experienced during fabrication of rod prototype GNK-L-24P. The infrared scans of -24P indicated that the density and contact loss was even more severe than that on -22P, but we decided to test the prototype because useful information could still be obtained.

The rod endured about 10 and 9 h, respectively, of transient and steady-state operation at a maximum cladding temperature of about 750°C and power levels to 38 kW before failure. Postfailure examinations revealed that failure occurred in the nickel center conductor near the ground end at the point of minimum annular BN density as indicated on the infrared scan. The reduced density (and thus thermal conductivity) resulted in about 25% reduction in expected rod capability.

The end plug fabrication procedure was changed for GNK-L-26P so that the nickel end plug could be removed with the heating element still encased. Although this modification resulted in an absolute minimum of disturbance to the inner BN preforms during fabrication, we learned that even spot welding the heating element to the nickel end plug partially loosened the preform adjacent to it, again resulting in lower than anticipated local BN density. These problems also occurred on rod prototypes tested in the HTS, but the lower power levels of operation and a relatively constant axial temperature made the consequences much less severe.

Because the low-density region was less severe than with -24P, we decided to test -26P in the SRSL. Operation was normal throughout the tests, which were conducted for about 6 to 7 h each day. On the beginning of the ninth day, we discovered that the current-carrying circuit was open. The rod was removed, inspected, and found to have an opening in the central nickel rod about 10 mm from the end plug. The nickel rod was pulled apart by thermal stresses; it had operated very close to its melting point, similarly to rod prototypes -22P and -24P. There was also evidence of a low-melting (1080°C) boron-nickel eutectic formed at the grain boundaries of the nickel rod, and the grains within the rod were very large, with some traversing the entire 2.16-mm cross section.

The boron-nickel eutectic was located primarily at the nickel grain boundaries, indicating that the eutectic was formed at a temperature below the melting point (~1425°C) of the nickel. However, rod prototypes -11P and -12P had been tested previously at more severe conditions, and the eutectic had not formed. Therefore, it can only be assumed at this point that the low inner BN density is the primary cause. This is also supported by the occurrence of the failure adjacent to the end plug, which should have been at a lower temperature than the "hot spot" region located about 0.25 m up into the heating element.

2.6 Phase V — Development of 8-mm Nonswaged FRS

Rod GNK-L-27P was the first 8-mm-diam prototype for the CFTL FRS to be fabricated. It contained no thermocouples and was fabricated with preforms pressed locally. Several fabrication problems were encountered, primarily with tooling, as is normal when a major dimensional redesign of a rod occurs. The same problems with low density of the inner BN preforms were again encountered in the nickel end plug region, largely because of the increased rigidity of the variable width heating element. The heating element diameter had been increased from 4.24 to 4.75 mm, and the nickel rod diameter increased from 2.16 to 2.59 mm as part of the design change. These changes resulted in less internal terminal heating and increased strength of the central nickel rod and the heating element.

The rod was tested in the SRSL, and the operation is summarized in Table 14. The rod failed at 35.3 kW power with the cladding temperature near 950°C. Failure analysis showed that the ground end of the nickel rod had been close to the melting point, and there were several cracks along the nickel rod adjacent to the heated section. These results closely paralleled those for rod -26P, except that the nickel rod of -26P exhibited failure near the ground end only.

The fabrication procedure was further modified to correct the localized low-density region. A fixture was devised to eliminate virtually all movement of the heating element near the end plug area during inspection and welding.

The presence of a boron-nickel eutectic that was found in the rod was considered to be cause for concern no matter what the conditions. Boron

Table 14. Summary of operational testing of rod prototype GNK-L-27P

Rod power (kW)	Sodium outlet temperature (°C)	Time at conditions (h)
10.0	704	6.8
19.0	704	21.5
19.0	777	20.5
20.0	927	7.3
26.6	500	0.5
26.0	927	3.0
30.0	927	10.0
35.3	927	0.1

has very little solubility in nickel, so a eutectic phase can occur above 1080°C at levels of 280 ppm boron in nickel. This boron must form from the BN to be available. No reliable data have been found on dissociation of BN to boron, but probably very little BN will dissociate at our operating temperatures. Both the dissociation and the eutectic phase formation depend on time. Although this may limit the useful life of the FRS at high temperatures, tests in the HTS at similar high-temperature conditions of the nickel rod did not show the formation of the boron-nickel eutectic to be a problem. Because of the possible time-temperature limitation of a boron-nickel eutectic formation and because of the probable increase in operating capability, the use of MgO central preforms as a substitute was pursued.

Eagle-Picher Industries, Incorporated (EPI), the BN preform fabricator, agreed to fabricate a small quantity of MgO preforms for our evaluation. Upon their receipt, a short test cell was fabricated to evaluate filling procedures. Severe spalling occurred when the preforms were in the copper region. The copper rod was reduced in diameter by swaging from 4.02 to 3.78 mm, but the spalling persisted. Spalling did not occur in the nickel terminals region. Evidently, the soft copper (annealed during brazing the nickel and copper rod and tubular terminals) interacts with the hardened, relatively spherical MgO particles. MgO, unlike BN, does not slide along the material surface, but instead "digs" into it.

Discussions with the preform manufacturer, as well as our own investigations, indicated that MgO powder properties, such as maximum particle size, particle size distribution, hardness, and particle shape, contributed to these poor results. Magnesia crystallites are harder than those of BN and are approximately spherical, whereas BN crystallites are flat, thin platelets, which tend to slide over each other.

These discouraging results made it clear that if cold-pressed MgO preforms were to be made usable for the CFTL FRS, then a thorough analysis and optimization of the powder properties for fabricability was needed. A decision was made to retain BN preform for use in the FRSs for the first bundle and to continue the investigation into a potentially useful MgO preform.

Nonswaged rod prototype GNK-L-29P was uninstrumented and contained inner BN preforms fabricated from TS-1449 powder made by EPI and outer BN preforms fabricated locally from the same powder. The TS-1449, a new, high-purity powder similar to HCM, was developed by Union Carbide Corporation, Parma, Ohio, in cooperation with ORNL.

Arcing and breakdown of the inner BN insulation was encountered, and investigation of the defect revealed a very thin (~2.5 mm) "mill scale" on the surface of the Kanthal A-1 starting material used to fabricate the variable width heating elements. Although the heating elements were subjected to extensive quality assurance activity, the scale had not been detected. When the Kanthal sheet material was cut and then wound into heating elements, regions of the scale became loose on the surface. When some of the coils were used subsequently to fabricate active component assemblies, pieces of the loose scale chipped off and were deposited within the inner annular BN. Electrical high-potential tests subsequently indicated that the insulation was contaminated.

Efforts to remove the scale were unsuccessful, so the heating elements had to be rejected. The Kanthal Corporation, supplier of the material, replaced the defective strip at no cost. Heating elements fabricated from the new material, as well as from Kanthal A-1 from another lot, were acceptable.

The short circuits in the rod prototype were partially cleared, and a decision was made to test it in the HTS. Table 15 summarizes these tests.

Table 15. HTS operational tests of rod prototype GNK-L-29P

Rod power (kW)	Maximum clad temperature (°C)	Transient ΔT (°C)	Number of cycles	Time of operation (h)
0.39	360	SS[a]		0.5
1.03	710	SS		73.0
1.0	680	SS		47.0
12.0	900	600	3	0.1

[a] SS = steady-state operation.

The rod prototype operated normally for 120 h at ~700°C clad temperature. The power was being adjusted for transient operation, and the rod had reached 900°C cladding temperature on a 12 s ramp at 12 kW when the heating element shorted to the nickel return rod through the inner BN insulation. Postfailure examination showed that the short circuit occurred in the region that was contaminated with Kanthal scale during fabrication.

Rod prototypes GNK-L-32P and GNK-L-33P were successfully fabricated with the new Kanthal A-1 heating elements. GNK-L-32P contained six type K, Inconel-sheathed thermocouples procured from Groth-Mazur Industries (GMI) for CFTL FRS; GNK-L-33P contained four GMI thermocouples and two type S (Pt vs Pt-60% Rh) thermocouples sheathed in platinum.

Table 16 summarizes operational tests on -32P in the SRSL. Steady-state operation of prototype GNK-L-32P was initially completed while a 500-kV CFTL power supply was being installed adjacent to the SRSL. The prototype was then thermally cycled using this new power supply for more than 4 d continuously before failure. The failure was caused by the central nickel rod melting and occurred during weekend operation, so an accurate assessment of conditions leading to the failure was not possible. However, all normal expected CFTL operational conditions were met or exceeded before failure, and more than four times the anticipated CFTL thermal transients were completed without a single rod thermocouple failure.

Rod prototype GNK-L-33P was tested in the HTS. Table 17 summarizes its operation.

Table 16. Operational tests of rod prototype GNK-L-32P in the SRSL

Rod power (kW)	Loop temperature (°C) Inlet	Loop temperature (°C) Outlet	Maximum cycling ΔT (°C)	Number of cycles	Total operating time (h)
0	350	350			175
29.0	370	650			442
32.8–3.3	370	700	165	220	2.5
28.0–0	370	650	125	7892	90
Total time					709.5

Table 17. Operational tests of rod prototype GNK-L-33P in the HTS

Rod power (kW)	Cladding temperature (°C)	Total operation time (h)	Number of thermal cycles
0.3	370	50	
1.0	720	265	
1.2	700 720[a]	914	
0–2.5	700–870[b]	137.5	8,250
0–8.6	425–1000[b]	106	4,240
Total time		1,472.5	
Total number of thermal cycles			12,490

[a] Temperature change at constant power was because of cladding emissivity changes.

[b] Thermal cycling operations.

A total of 1472.5 h was logged on -33P, of which 1229 were steady state, and most of these (914) were at ~700°C. The rod endured a total of 12,490 thermal cycles in 243.5 h of operation. Over 4000 very severe (425 to 1000°C in 15 s) cycles were conducted before rod failure. All four type K (Chromel-Alumel) thermocouples remained operational throughout the entire test. This is additional verification that the short lifetime of type K small-diameter thermocouples experienced with earlier prototypes has been increased considerably. Both of the type S (Pt vs Pt–10% Rh) thermocouples failed early in the operation.

Rod failure was caused by a short between the heating element and the central rod located ~40 cm from the upper terminal. This placed the entire potential of 148 V across ~0.6 Ω, resulting in a heat flux of approximately twice the design rating of 200 W/cm^2 during the "on" position of the thermal cycle. This resulted in temperatures high enough to melt the heating element and nickel rod in a region about 25 cm long. Failure occurred when internal pressure blew a hole in the stainless sheath, ejecting molten nickel and Kanthal A-1 alloy and causng an open circuit.

Table 18 summarizes operational tests on rod prototype GNK-L-34P, the last CFTL prototype to be fabricated and tested. This prototype contained

Table 18. Operational tests of rod prototype GNK-L-34P in the SRSL

Rod power (kW)	Loop temperature (°C)		Maximum cycling ΔT (°C)	Number of cycles	Total operating time (h)
	Inlet	Outlet			
0	350	350			75
28.6	350	600			415
28.6–0	350	655	125	5800	66
Total time					556

six Inconel 600 sheathed, type K thermocouples that were procured for the bundle AG1. All six thermocouples operated normally throughout 415 h of powered, steady-state testing and 66 h of thermal transient testing that included 5800 thermal cycles. The rod failed in a manner similar to that of -32P. Analysis indicated the presence of a low melting boron-nickel eutectic reaction. The reaction appeared to proceed quite slowly but weakened the Ni control rod, eventually causing failure. The reaction, when complete, reduces the equivalent nickel melting point from 1450 to ~1000°C, which limits both lifetime and thermal cycling ability of the rods. This problem could be eliminated with the use of central MgO cold-pressed insulators. However, project closeout did not permit us to try to accomplish this goal.

All normal requirements were met, and long-term transient operation was demonstrated. Completion of testing on this prototype ended fabrication and testing on CFTL FRS. The task of obtaining a usable MgO central preform was not completed. Although operational requirements could be met with the FRS in their present design state, the increased thermal expansion of a central MgO preform would enhance operation by increasing annular radial thermal conductivity and eliminating the boron-nickel reaction.

3. BN PREFORM DEVELOPMENT

The need for high-reliability, state-of-the-art FRSs for use in high and low heat flux high-temperature transient experiments for several ORNL programs has accelerated the development of manufacturing techniques for cold-pressed BN preforms. The initial preform development and use are more fully detailed in Ref. 5.

The major advantages of BN preforms include (1) ease of FRS manufacture; (2) closer dimensional control; (3) more uniform insulation density and, therefore, more uniform thermal conductivity and heat flux; (4) improved inspectability and purification of BN preforms with appropriate rejection of contaminated items; (5) almost complete elimination of process-induced contaminants during the installation and compaction of BN preforms; (6) lower FRS internal temperature because of higher thermal conductivity and, thus, better reliability; (7) improved (essentially perfect) heating element concentricity with the FRS sheath; and (8) improved transient and high-temperature (>1000°C) lifetime for FRS internal thermocouples by elimination of swage-induced cold work.

Because of the advantages inherent in the use of preforms, the increased need for FRS reliability in large bundles, the greater severity of testing conditions, and the strict FRS procurement schedules dictated by large bundles, a vigorous BN preform development effort was initiated some years ago. This development effort has recently culminated in the ready availability of high-quality preforms on a production basis.

The fabrication process for cold-pressed BN preform consists of powder pretreatment, pressing, and purification. Prior to the development of automatic lubrication techniques for preform die bodies, pretreatment was necessary for successful pressing. It is now an option, depending upon the preform properties desired. Pretreatment is useful if radial crystallite orientation (and thus thermal conductivity for a given preform density) is to be enhanced or if increased structural integrity is desired.

Pressing development included utilization of double-acting presses and the determination of appropriate pressure, dwell time, final density (and density variation), lubrication, and pellet expansion parameters.

Processes have also been developed to press cylindrical preforms with axial grooves. Purification techniques were developed to reduce the concentration of fabrication-induced impurities to levels that would permit high-temperature operation (1300°C and higher).

3.1 Powder Pretreatment

Pretreatment consists of ball-milling the powder in reagent-grade hexane with an alumina ball mill for 4 to 12 h to achieve a submicron particle size. The powder is then slurried in a solution of organic lubricant such as camphor or acetone-1 wt % stearic acid in hexane, the mixture is allowed to settle before the liquid is decanted, and the remaining slurry is dried by evaporation. A small amount of the lubricant (<0.5%) remains on the particle surface to lubricate and to act as a pressure-transmitting agent during pressing. The powder is prepressed in ~100-g batches at 280 to 840 kg/cm². The resulting large pellet is then broken up with a mortar and pestle and screened through sizing sieves. This produces a powder composed of agglomerates 0.05 to 0.5 mm in diameter, having a tap density of 0.5 to 0.7 g/cm³. Tap density is the BN density after the measuring vessel is lightly tapped.

3.2 Preform Pressing

The development of cold-pressed BN preforms was initiated at ORNL using low-volume laboratory-scale techniques. Similar high-quality preforms are now provided on an automated basis by EPI, Miami Research Laboratory, Miami, Oklahoma. To obtain preforms that are of uniform density (±1%) and that have a length-to-diameter ratio of 2:1 (or more) requires a double-ended hydraulic press that can supply a constant pressure up to 5250 kg/cm² for a minimum of 1 s. Lubrication of the die wall contacting the outer surface of the preform is required in most cases, even with the use of lubricated powders. Of the several agents tested, a solution of 1% stearic acid in acetone was found to be the most suitable for die body lubrication.

A typical die designed for manually pressing tubular preforms is shown in Fig. 7. Although simple in construction, the die must be fabricated to very close tolerances to prevent seizure from powder buildup on its inner and outer faces. Additionally, the die body cavity and contacting parts must have hard, smooth, low-friction surfaces. Dies for automatic production of BN preforms are more sophisticated. They contain tool-steel punches having a hardness value of Rockwell C58 to 60, with a die body containing a tungsten carbide insert. The die body has a 7.5° bevel for 19.0 mm on the top to facilitate gradual expansion of the preform as

ORNL PHOTO 6383–77

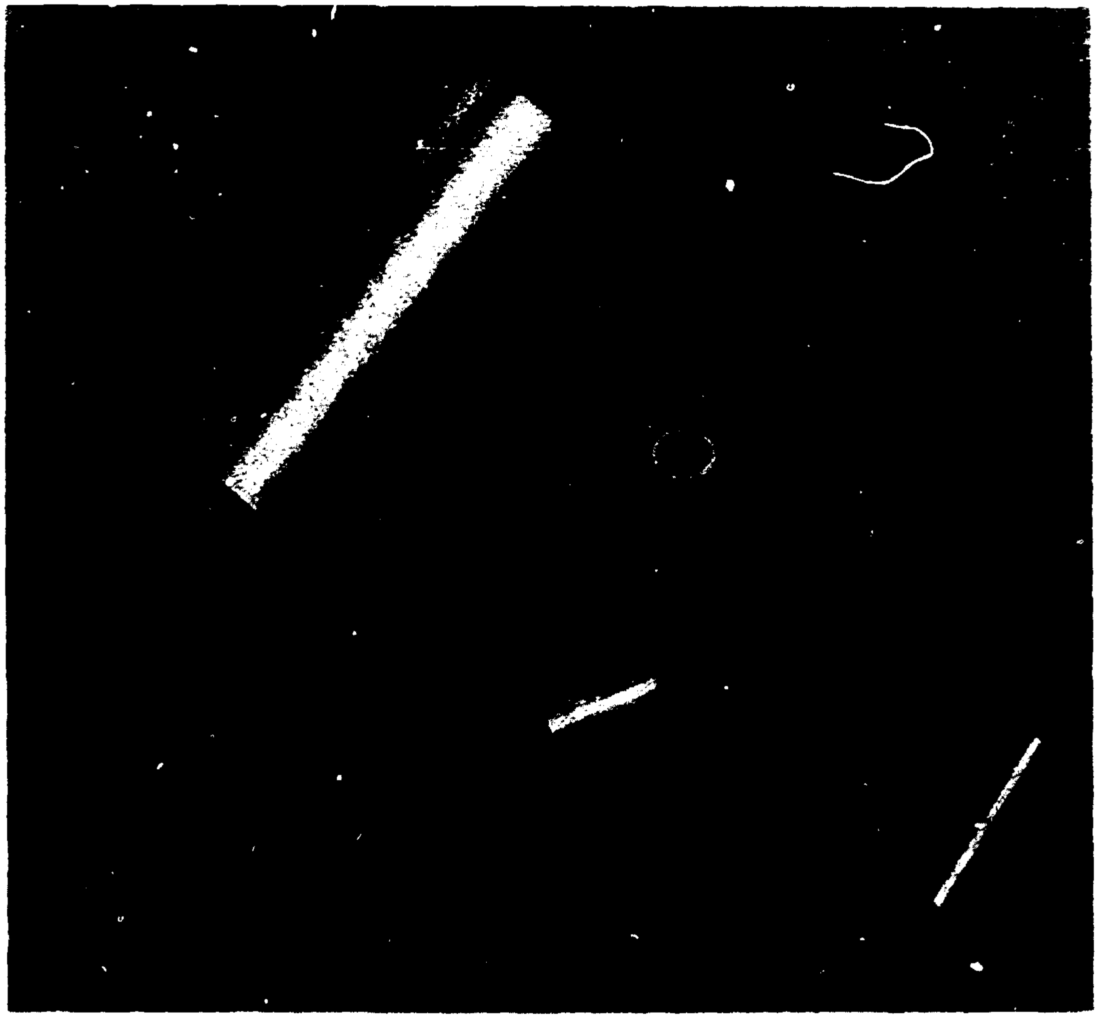

Fig. 7. BN preform die for manually pressing preforms.

it exits from the die. Approximately 2.5% increase in OD and 1.75% increase in ID occur as the preform is removed from the die and purification subsequently takes place.

Initially, only solid or cylindrical preforms were pressed. For those FRSs that contained internal thermocouples, annular BN preforms were initially grooved using a broaching device. Instrumented FRSs for the CFTL have been successfully fabricated with BN preforms grooved by this method for the last several years. However, 5 to 10% breakage occurs during grooving, the process is not adequate for FRSs containing six or more thermocouples or for annular width <1 mm, and BN preforms made of Union Carbide Corporation—Carbon Products Division (UCC-CPD) grade HCM powder, the standard BN powder for die lubricated preforms, cannot be grooved. The larger particle size of the HCM powder causes the BN preforms to be severely weakened structurally at the grooves. Many (~30 to 50%) break during grooving, and those that do not are too fragile to use for subsequent filling. The BN preforms made with pretreated powder do groove adequately, but powder preparation increases the costs of this type of preform.

To eliminate the above disadvantages, a BN preform pressing die containing splines that produced grooved BN preforms was designed by engineers at ORNL and at EPI, Miami Research Laboratory. This die, shown in Fig. 8, allowed the pressing of BN preforms for the latest CFTL FRS design that contained six 0.5-mm grooves spaced in 60° intervals. Although the die cost is approximately twice as much as a similar nongrooved die, the 5 to 10% grooving loss is avoided, the quality of BN preform is enhanced, and HCM powder can be used without pretreatment.

Studies have been conducted to optimize the following important pressing parameters: pressure, dwell time at pressure, and optimum length-to-thickness (or length-to-diameter) ratios for preforms as functions of final density and variation in final density. Percent expansion after pressing was evaluated to enable accurate final preform size control.

Figure 9 shows a typical density-vs-pressure relationship for pressed TS-1325 powder. The increase in density with pressure is almost linear until 3.5×10^6 kg/m^2, where it levels off to an apparently optimum density of 1.89 kg/m^3 (84% TD). Because the 3.5×10^6 kg/m^2 pressure allows

ORNL PHOTO 7006-80

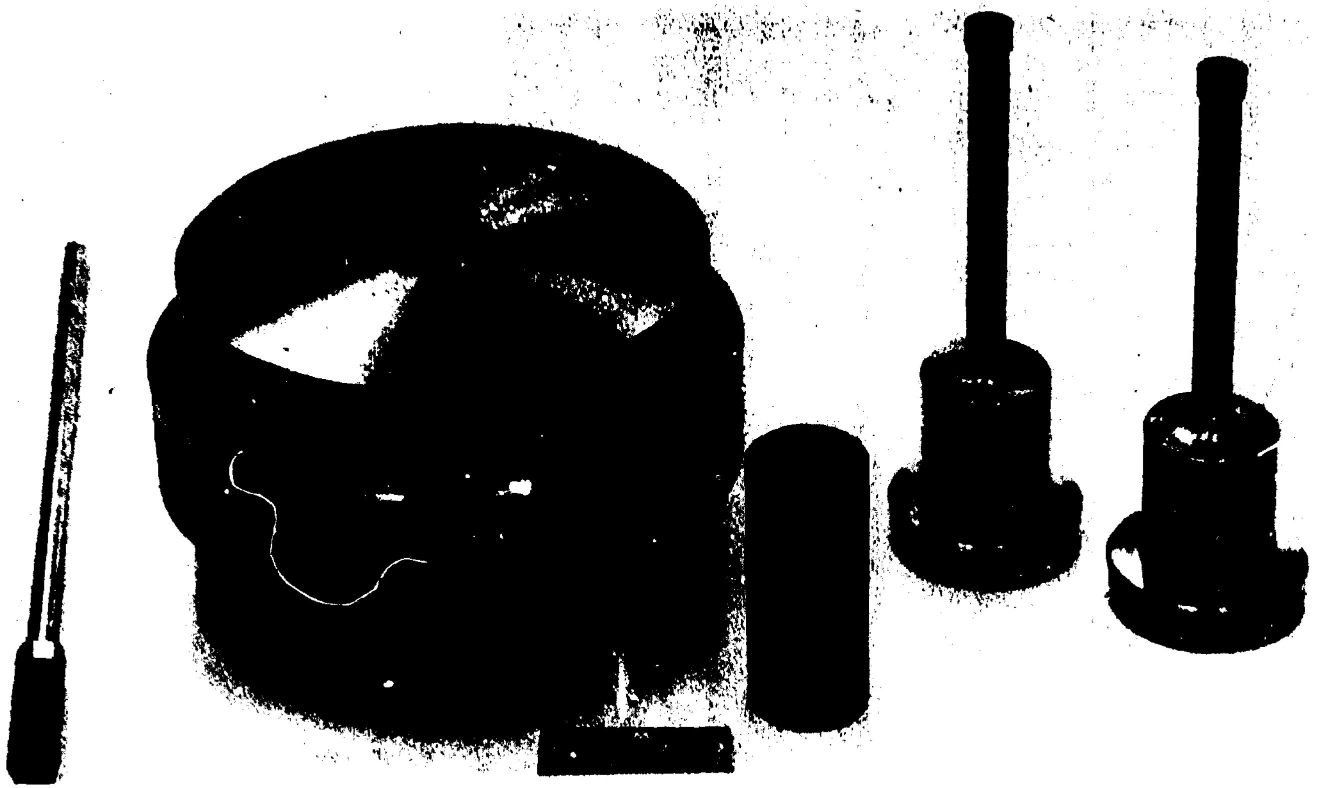

Fig. 8. BN preform die for automatically pressing grooved, annular preforms. The die body contains a shrink-fit tungsten carbide insert that bears electro-deposition machined grooves.

ORNL-DWG 76-2052A

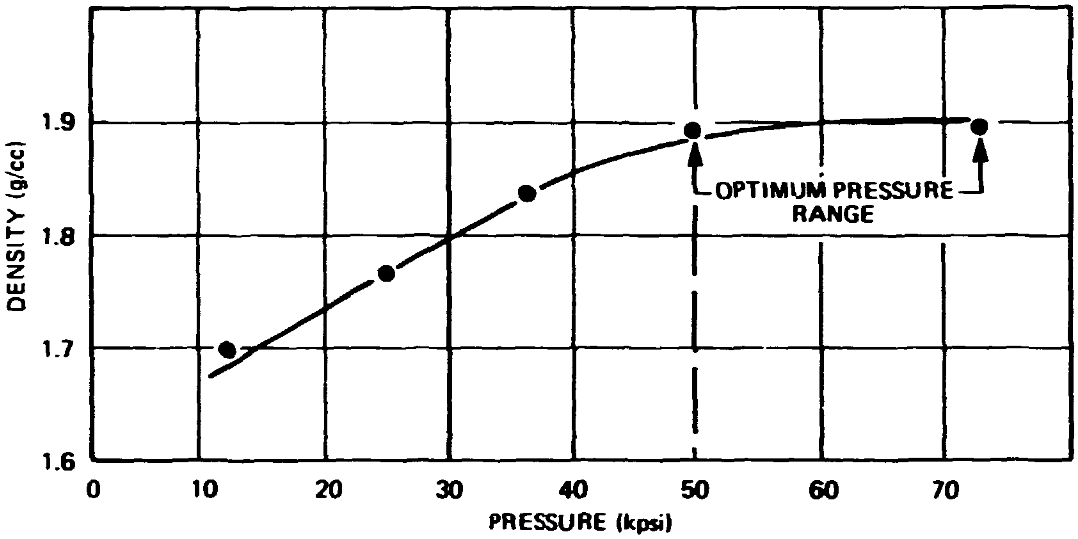

Fig. 9. Density vs pressure for a pressed TS-1325 BN powder.

manual pressing with tool-steel dies without major die jamming, this pressure was used in most ORNL applications. However, pressures as high as 5.625 x 10^5 kg/m^2 have been used in automatic pressing.

Dwell-time measurements at constant pressure are difficult to obtain, but experience has shown that short dwell times (<0.5 s) do not allow sufficient time for adequate particle movement or for release of entrapped air. As a result, density variations along the preform length can be excessive, and the structural quality suffers. Dwell times in excess of 3 s are unnecessary because all entrapped air has escaped within that time period.

3.3 Preform Purification

Removal of lubricating and pressure-transmitting additives to reduce the carbon and oxygen impurities to acceptable levels is now a routine part of the preform fabrication process. This is accomplished by first subjecting the preforms to a bakeout at 232°C in a 1.33- to 4-Pa vacuum for 8 to 24 h to remove most of the readily vaporized organics. Following the bakeout, preforms are treated for 8 to 12 h in an anhydrous ammonia atmosphere at 900 ± 25°C. Carbon and oxygen impurities are removed via the following reactions:

$$3C + 4NH_3 \rightarrow 3CH_4 + 2N_2 ,$$

$$3O_2 + 4NH_3 \rightarrow 6H_2O + 2N_2 ,$$

and

$$CH_4 + H_2O \rightarrow CO + 3H_2 .$$

An Inconel or molybdenum boat is used to decrease the possibility of contamination, and care is taken to ensure that the preform surface area available to the ammonia vapor is as great as possible. The furnace is swept with nitrogen gas at the completion of purification and is cooled to ambient under a nitrogen blanket. Initial purification operations were performed at ORNL. However, a microprocessor-controlled purification furnace was purchased by EPI, and automatic purification techniques were developed by them. Preforms are now received in their final, purified condition.

The ultimate test of the purification process is the direct measurement of adequate electrical insulation resistance at high temperatures (>1 MΩ-cm at 1000°C). Figure 10 shows the results of such tests on a test cell fabricated with preforms of TS-1325 powder. These preforms were (1) pretreated with hexane-1% camphor, (2) pressed at 3.5×10^8 kg/m² using an acetone-1 wt % stearic acid die body lubricant, (3) dried in a vacuum, and (4) baked in anhydrous ammonia at 925°C for 8 h. High-temperature resistance decreased at the rate of a factor of 10 per 125°C and was above 100 kΩ-cm at 1250°C. Extrapolation of these data gives a resistivity of 10^4 Ω-cm at 1400°C, which is adequate for all FRSs designed to date.

3.4 Quality Control

The single most critical part of an FRS is the BN preform. Approximately 350 preforms are used to fabricate one full-length GCFR-CFTL FRS.

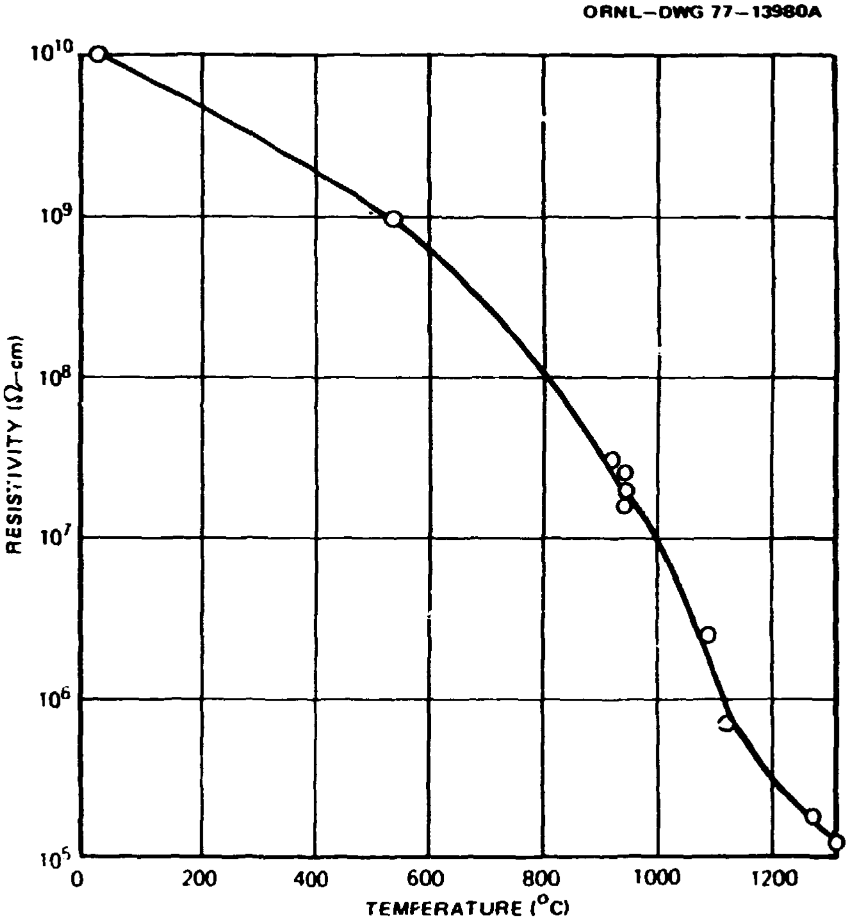

Fig. 10. Resistivity vs temperature for preform test cell fabricated with pretreated, lubricated, and purified TS-1325 BN.

The preforms must insulate as much as 350 V at temperatures up to 1400°C. In the 1120-mm heated section, the preforms must also have extremely uniform density and thermal conductivity. Additionally, dimensional tolerances of the preforms should be within ±0.025 mm. An organic impurity or metallic inclusion in only one preform per FRS (0.3%) can result in the rejection of an entire FRS.

In the past, no established quality criteria for BN powder, preform dies, or preforms have existed. Part of our developmental effort was directed towards establishing criteria that would result in low FRS rejection rates while not imposing too stringent time and cost restraints on the inspection process. Efforts to improve the BN powder quality are discussed in Ref. 7 and will be summarized in this section. Determination and control of die and preform quality criteria gradually evolved throughout this effort as a result of feedback from FRS electrical and radiographic inspections and FRS operational performance.

The HCM powder, as initially procured from UCC-CPD, met procurement specifications for <0.5% total impurities. Even so, it contained enough conducting metallic inclusions to prevent its use in FRS fabrication. A joint effort by UCC-CPD and ORNL resulted in the elimination of ~90% of the particles via magnetic separation without significantly affecting other powder properties.

The major inspections now required for acceptance of BN powder are: (1) radiography, (2) a spark-source mass spectrometer scan, (3) oxygen analysis (by neutron activation), and (4) a carbon Leko analysis. Additionally, an electrical conductivity test cell is fabricated from each new lot of BN powder, and the BN resistivity is tested to 1200°C with a 500-V megger. It must attain a minimum resistivity at that temperature of 10^5 Ω-cm and remain stable for a minimum of 60 min. The impurity criteria now established are summarized in Table 19.

An ultra-pure BN powder designated TS-1449 has been supplied to ORNL by UCC-CPD through a joint development that spanned 18 months. This powder was produced to the specifications of Table 19 using improved and more

Table 19. Contamination limits on BN powder

Contaminant	MAX limit impurities
O_2, %	0.2
C, %	0.1
Fe, ppm	10
C_a, ppm	30
Ti, ppm	30
Other metals (each), ppm	30
Borates, %	0.2
Total impurities, %	0.5
Metallic inclusion, in. (cm^3)	
>0.007 (0)	
0.005 ≤ 007 (0.3)	
0.003 < 0.005 (1.5)	

stringently controlled processing steps than previously employed with HCM grade powder, which is similar. High-gradient magnetic separation was used to eliminate most metallic impurities during the Orocessing. Because of this effort, a process now exists that can routinely produce powder of high quality when needed.

Dies for the automatic production of BN preforms are ordered to very strict requirements. Figure 8 shows a photograph of a typical annular preform die with grooves. The ID and OD tolerances are set at a maximum of 5.1 µm. Die body upper and lower surface parallelism, surface finish, and hardness of all contacting parts are also critical and are closely controlled. The most difficult dimension to control is that of the lands and grooves of the relief region at the top of the die body. The requirement of 1 mm taper per millimeter on both lands and grooves is critical if the preform is to expand equally on its outer surface as it is removed from the die. Unequal expansion causes preform deformation or cracking.

Automatic pressing of the BN preforms requires setup and control of up to 62 separate functions. Although many parameters, once determined for one preform type and dimension, are fairly similar for some preform types, this is not true for many others. Therefore, initial optimization of pressing parameters requires an experienced engineer, and thorough training of qualified operators is a necessity.

Figure 11 shows the Hydramet-American Model 12-B hydraulic electronic press employed for BN preform automatic pressing. There are three hydraulically driven rams, the upper and lower punch rams and a core rod ram. Each permits individual control of prepress dwell time, rate of movement (in and out), press dwell time, eject dwell time, and pressure.

An automatic die body lubrication system (DBLS) was designed specifically for BN preform pressing. Its functions are to spray a lubricant into the die body ID and core rod (for tubular preforms) and to dry this lubricant prior to die powder feeding. This DBLS has become an integral part of the Hydramet-American press.

Another feature unique to BN preform pressing is the oscillating-vibrating powder feed shoe. This device is necessary because the poor flow characteristics of camphor-treated TS-1325 powder (used for some of the preforms) and the thin wall of many of the tubular preforms made it

ORNL PHOTO 3071-82

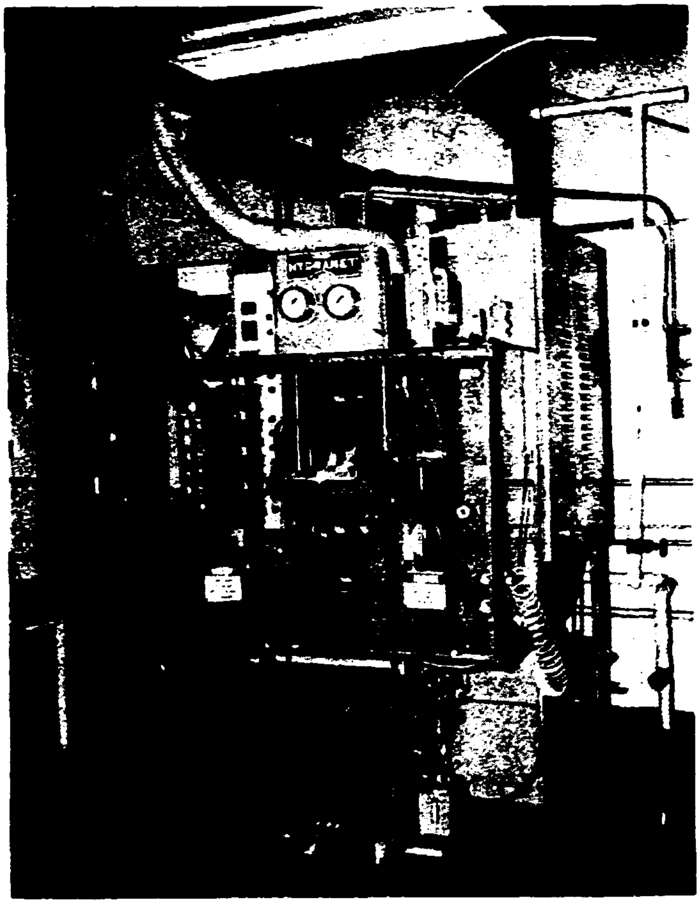

Fig. 11. Hydramet-American model 12-B hydraulic-electronic press used by EPI to cold press BN preforms.

very difficult to feed powder into the die. The time and number of oscillations to fill are individually controlled so that the die cavity is completely filled prior to pressing.

During the production of preforms, quality must be monitored on a continuous basis. Small variations in such aspects as powder quality, humidity, and press temperature may produce variations in preform properties that will result in rejection. Preform quality is monitored by continuous visual checks on all preforms during pressing and by density checks on 5% of them. Visual inspections include checks for chipped ends, soft parts, significant length variations, or foreign matter on the preform surface.

When completed and purified, preforms are stacked in 10-cm-diam, 1-cm-high petri dishes; packing powder (rejected BN powder) is poured in to fill all voids, and lids are put on and taped to the dishes. Several dishes are then wrapped with air-cushioned wrapping material, and the packages are enclosed in a box filled with pieces of polystyrene foam. The preforms are shipped via air carrier. This method of packing and shipping does not introduce contamination and has resulted in only a very small number of broken preforms.

When the preforms are received at ORNL, they are unpacked, and the packing powder is removed and stored. The preforms then undergo a series of receiving inspections, and an archive sample is taken.

Table 20 shows the preform physical property data sheet on which the inspection data is accumulated. It includes the preform type, powder used, the archive sample number, type of lubricant used in pressing, and record of the total length received. The ID, OD, and density data are also recorded before the preforms are purified and again after purification.

The most important incoming inspection is the radiographic inspection that is performed on 100% of the preforms. After receiving inspections are complete, most of the preforms still remain in the petri dishes. The dishes are then visually checked to remove bad preforms, and the remaining preforms are packed in the dishes so tightly that no movement can occur. The dish tops are then replaced, tightly taped, and the dishes numbered and marked with a zero degree reference.

Radiographs are then taken of the dishes in groups of four. Lead numbers and reference markers are used that correspond to those marked on the dishes. The film is developed, and the radiographic images of preforms are inspected for metallic inclusions. Any preform with a metallic inclusion >0.13 mm is rejected, and preforms with more than one visible metallic inclusion of any diameter within a 90° section are rejected. After the inspections are completed, the radiographs are compared with the petri dishes and reject preforms are removed.

Total radiographic inspection of preforms has virtually eliminated FRS rejection because of metallic inclusions within the insulating region.

Table 20. BN SHEET

PREFORM TYPE:
POWDER USED:
AVG. LENGTH: _____ in.
TOOLING:
CORE ROD OD _____ in.
DIE BODY ID _____ in.

ARCHIVE SAMPLE NO.:
LUBRICANT:
TOTAL LENGTH: _____ in.
TOTAL WEIGHT: _____ g
TOTAL LENGTH: _____ in. (after purified)
TOTAL WEIGHT: _____ g (after purified)

ITEM	BEFORE PURIFICATION	AFTER PURIFICATION
INSP. INITIALS		
DATE		
OD (in.)		
ID (in.)		
DENSITY (g/cm^3)		

PURIFICATION SCHEDULE:

	TIME	TEMPERATURE	ATMOSPHERE
1			
2			
3			
4			
5			

OTHER TESTS:

CHEMICAL ANALYSIS -
CONDUCTIVITY CELL -
RES. AT ROOM TEMPERATURE = _____ ohms
RES. AT _____ °F = _____ ohms
HOLD TIME AT T_{MAX} -
FRS/TEST CELL NO. _____

This inspection has been the most important factor enabling the fabrication of large bundles of very high reliability FRSs.

A spark-source mass spectrographic analysis and carbon and oxygen analysis are obtained on sample purified preforms from a new lot of powder or from a new process. Additionally, an archive sample is taken from every lot of preforms after purification. Traceability of preforms is maintained throughout FRS fabrication. Thus, samples are available for analysis if subsequent fabrication problems arise that may result from defective preforms.

A conductivity test cell is also fabricated from preforms from each new lot of powder or from those fabricated with a new process. High-temperature resistivity tests from these test cells provide operational performance data that indicate powder quality.

Final precautions taken with the preforms are to (1) store them in a furnace at 250°C and at 13.3 mPa for 24 h prior to use, (2) keep them above 100°C (by using a hot plate) during FRS fabrication, and (3) perform a 250°C, 13.3 mPa bakeout of the assembled FRS.

4. VARIABLE WIDTH RIBBON HEATING ELEMENT DEVELOPMENT

As the power-generating component of an FRS, the heating element is required to operate under conditions approaching the maximum capability of the material. The heat flux profile for the GCFR-CFTL FRS is generated by a coiled ribbon heating element embedded in BN insulation within the stainless steel sheath. Chopped cosine (cosine profile chopped at either end so that power goes to zero abruptly) heat flux profiles have been generated by varying the helical pitch of a constant width ribbon. This method, while acceptable for steady-state tests, resulted in unacceptable profile perturbations during transients in heat flux.

This paper describes the materials selection, fabrication development, and joining of variable width, helically wound heating elements, which eliminate the disadvantage of variable pitch ribbons while providing other important advantages of an evolving FRS fabrication technology.

4.1 Heating Element Materials

Heating element materials of three types have been used during the evolution of the GCFR-CFTL FRS. Table 21 summarizes some of their important properties. Because the maximum operating temperature and heat-flux product depends on the heating element melting point, the Pt-8% tungsten alloy would apparently be the best choice despite such obvious disadvantages as the relatively high temperature coefficient of resistivity (TCR) and the cost. This material was investigated for both the breeder reactor program (BRP) and GCFR programs. A thorough summary of development in support of the BRP is presented in Refs. 5 and 9. The principal findings of this previous work were (1) the material was subject to excessive grain growth when prestrained and then operated above about 1300°C, and (2) boron from the BN insulation reacted to form a low melting (~1000°C) boron-platinum eutectic. The reaction initiated in, and progressed from, the grain boundaries when the material was operated near 1400°C.

As part of the GCFR-sponsored effort, methods to retard grain growth, to protect the heating element from boron attack, and to eliminate the

Table 21. Heating element materials used in GCFR-CFTL FRS prototypes

	Designation		
	Nichrome V	Kanthal Al	Pt-W
Composition, wt %	Ni-20 Cr	Fe-22 Cr-5.5 Al-0.5 Co	Pt-8 W
Melting point, °C	1400	1510	1870
Maximum use temperature, °C	1350	1450	700
Resistivity at room temperature (μΩ-cm)	108	145	76
TCR[a] x 10^{-6}, °C	70	35	270
Coefficient of linear exp x 10^{-6}, °C	17.0	15.0	8.9
Relative high-temperature tensile strength	Medium	Low	High
Weldability	Very good	Poor	Good
Fabricability	Very good	Good	Poor

[a] Temperature coefficient of resistivity, room temperature to 1000°C.

free boron in BN were studied. Of these, the most successful was the grain-growth retardation effort.[10]

After several attempts, excellent grain-growth retardation was achieved using a homogeneous dispersion of 0.1% MgO into a powder of platinum-8% tungsten. The material, when processed by powder-metallurgy methods, exhibited stabilized grain growth both at high temperatures (up to 1600°C) and at medium temperatures (1200°C) for long periods of time. Figure 12 (a and b) shows the modified and unmodified platinum-8% tungsten alloy, respectively. The grain size of the modified alloy, after treatment at 1200°C for 97 h in vacuum, is essentially the same as it was at room temperature, while the control sample exhibits excessive grain growth.

Following this investigation, several feet of the modified alloy were prepared. Electrical resistivity, thermal expansion, and mechanical property tests were conducted. Except for a slight discontinuous increase in

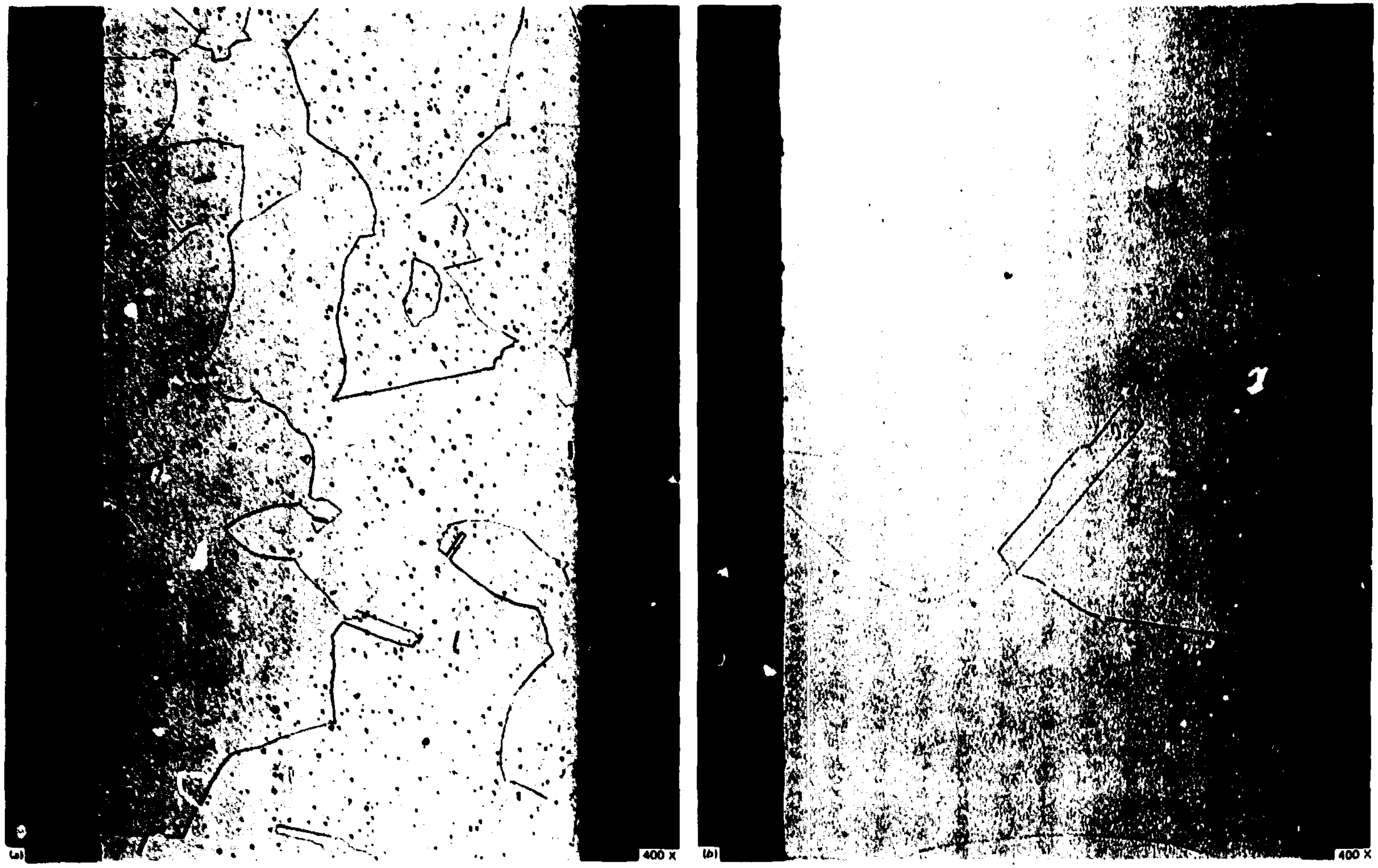

ORNL PHOTO 3072-82

Fig. 12. Modified and unmodified platinum-tungsten alloy after treatment at 1200°C for 97 h in vacuum. (Original reduced 50%)

the thermal expansion above 1600°C and a small amount of uniformly distributed porosity, the modified alloy was equivalent to the unmodified one. Welding tests showed that, with slight modification of the procedure, welds were obtained that were equivalent to the unmodified sample.

Finally, a series of compatibility tests of the modified and unmodified alloys in intimate contact with the cleaned and purified BN were conducted. These results, illustrated in Figs. 13–16, showed that boron attack of the modified alloy was enhanced over that of the unmodified alloy, even though its grain size remained smaller. Apparently, porosity present in the modified alloy contributed to increased diffusion rates and accelerated attack. In view of these data, it was concluded operating time at high temperature (~1600°C) must be limited to a matter of minutes for rods fabricated with either alloy.

Concurrent with the above-mentioned tests, conductivity test cells made with each of the two alloys were fabricated locally. Identical series of tests were conducted on each in the SRSL, culminating in operation at 1000°C and at 270 W/cm^2 with the unmodified alloy (first) test cell, while the modified alloy (second) test cell operated at an even higher power of 320 W/cm^2. Note that the second cell operated at a heat flux almost twofold higher than the maximum power level of CFTL rods. The central heating element reached a maximum temperature of 1354°C in the second cell. These results suggest that (1) grain-growth retardation is at least as important as protection from boron attack, and (2) the modified alloy may be somewhat of an improvement over the unmodified version.

The inability to eliminate boron-platinum eutectic formation and unfavorable effects of thermal expansion mismatch of the platinum-tungsten/molybdenum FRS (Sect. 2) finally led to increased emphasis on the other two, nonrefractory heating elements materials, Nichrome V and Kanthal A-1 alloy.

Nichrome V (see Table 21) is a widely used heating element material for obvious reasons. It has a low TCR, good high-temperature strength, and good welding and fabricating characteristics. Its melting point of ~1400°C is the lowest of the three candidate materials and essentially the same as the FRS cladding. This precluded its use in FRSs that would be tested under approach-to-melting conditions for the cladding. It became

M&C PHOTO
Y150119

Fig. 13. Platinum-8% tungsten alloy imbedded in BN, treated at 1200°C for 97 h. (Original reduced 27.5%)

M&C PHOTO
Y150127

Fig. 14. Platinum-8% tungsten and 0.1% MgO alloy, imbedded in BN, treated at 1200°C for 97 h. (Original reduced 28%)

M&C PHOTO
Y150106

Fig. 15. Platinum-8% tungsten alloy imbedded in BN, treated at 1500°C for 1 h. (Original reduced 27%)

M&C PHOTO
Y150138

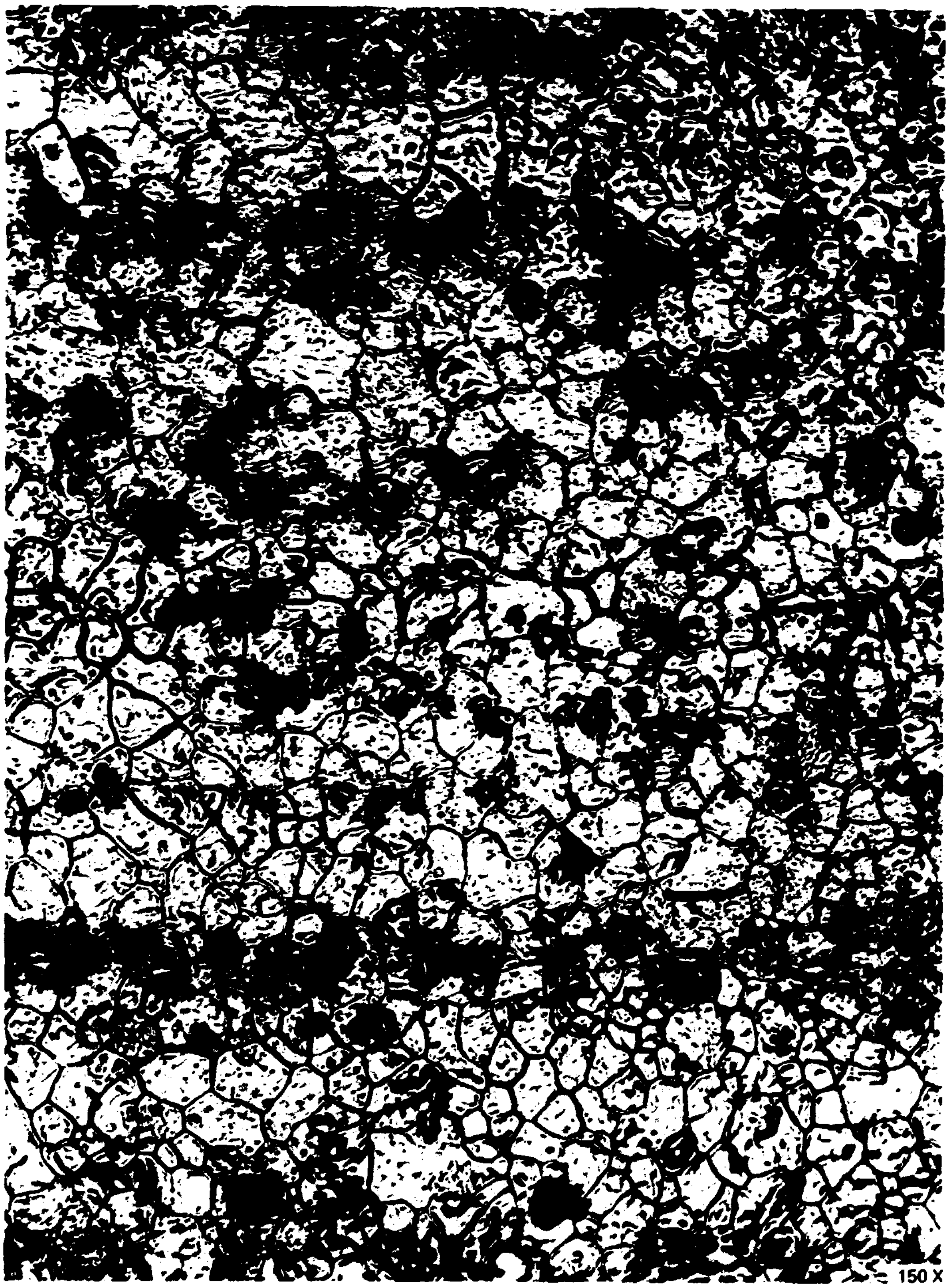

Fig. 16. Platinum-8% tungsten and 0.1% MgO alloy imbedded in BN, treated at 1500°C for 1 h. (Original reduced 28%)

the reference heating element material and proved very successful for FRS testing up to 1000°C cladding temperature. However, the need to conduct approach-to-melting tests and the higher radial ΔT associated with nonswaged FRSs led to the investigation of Kanthal A-1 as a high-temperature heating element material.

Kanthal A-1 (Table 21) has a melting point ~100°C higher than Nichrome V and a lower TCR but has poor weldability and low high-temperature strength. The weldability disadvantage was overcome by the use of precise laser welding techniques.[11] Because the material was to be tightly contained within a ceramic insulator and, as a coil, would not be subjected to high thermal stresses, low strength at high temperature could be tolerated.

Subsequent fabrication and testing of FRSs containing variable width Kanthal A-1 heating elements validated this assumption. Based upon these results, reported in Sect. 2, Kanthal A-1 became the reference material for the GCFR-CFTL FRS.

4.2 Heating Element Fabrication Development

For peak FRS performance, the heating element, as the power generating component, is required to operate under conditions approaching the maximum capability of the material. The geometry of, and the configuration within, the FRS must be optimized based upon careful consideration of the thermal, mechanical, and electrical properties of FRS materials for the operational range. Reference 12 presents the detailed design, fabrication and inspection of variable width ribbon heating elements. A summary of this work as pertains to the CFTL FRS is presented here.

Under high heat flux conditions the nonswaged FRS will have a radial temperature profile as high as 160°C/mm so that the radial distance from the OD of the cladding to the ID of the heating element directly determines maximum operating conditions for the heating element at a given cladding temperature. Generally, the heating element diameter should be as large as possible while maintaining an appropriately thick electrically insulating layer of BN between the heating element and the FRS cladding. This annular region, which contains the FRS internal thermocouples, must maintain acceptable insulation resistivity at the required operational temperatures and must withstand the voltage potential between heating element and cladding or thermocouples without dielectric breakdown.

Because FRS peak internal temperature will increase as the ribbon thickness is increased, the thickness of the heating element should be as small as practical. Problems in forming or fabricating the ribbon, as well as handling, assembling, and swaging of ribbons and FRSs, place practical limits on the minimum ribbon thickness. The heating element must be capable of withstanding differential thermal expansion without permanent deformation during transient testing. As the ribbon thickness decreases, normal variation in its thickness becomes much more significant to local heat generation, in as much as the generation (with constant current through the ribbon) is inversely proportional to thickness. A practical ribbon thickness and tolerance limit is 0.25 ± 0.0125 mm.

Because transient operation of the CFTL FRS is of paramount concern, the heating element configuration must be carefully analyzed under transient conditions as part of the design effort. Heat capacity effects become pronounced in the transient heat flux profile, and axial and circumferential conduction do not smooth out the profile as they do under steady-state conditions. Furthermore, with the use of BN preform technology, axial conduction is much lower than radial conduction because of the anisotropic nature of thermal conductivity in BN preforms. Thus, under transient conditions, such properties as the turn-to-turn spacing, ratio of coil surface area to sheath surface area, coil diameter variation, coil turns per unit length, and eccentricity of the heating element become important.

Evaluation of thermal, mechanical, and physical properties of the heating element material provide design limits for the variable width coil and assure that it can be fabricated and will be suitable to its environment. Electrical considerations provide the design basis for the exact configuration to meet FRS operating requirements.

4.2.1 Design

Design of the heating element is dependent upon current and voltage available from the power supply. For parallel connection of the FRS to the power supply, a heating element resistance "window" can be calculated by

$$R_{max} = V^2/P \; , \qquad (4.1a)$$

and

$$R_{min} = P/I^2 \; , \qquad (4.1b)$$

where V is voltage, P is power in watts, and I is current. Factors such as resistive heating of the terminal, FRS dielectric breakdown, and material TCR must also be considered in optimizing the element resistance.

Once the resistance has been determined, the design of a constant width, rectangular ribbon heating element can be accomplished using the method illustrated in Fig. 17. From this, ribbon width w is derived in terms of the physical and dimensional parameters of the heating element:

$$w = \left(\frac{\pi D \rho C}{Rt}\right)^{1/2} \; . \qquad (4.2)$$

The ribbon thickness t, coil pitch diameter D = OD − t, material resistivity ρ, wound element resistance R, and axial heated length C are the input parameters that, along with the ribbon width w, completely define the wound coil.

Once the width has been determined, factors describing the FRS power profile are needed. These are peak/average power P_p/P_a, peak/minimum power P_p/P_m, and coil axial length C. Figure 18 shows a typical chopped cosine profile where P_p, P_a, P_m, and C are defined. The power profile of Fig. 18 can be defined by

$$P = P_p \cos \phi \; , \qquad (4.3)$$

where ϕ is the angle that relates the power profile to the coil axial length C. By definition, $\cos \phi_p = P_p/P_p = 1$, and $\phi_p = 0°$ at P_p. The

ORNL DWG 80-5573A ETD

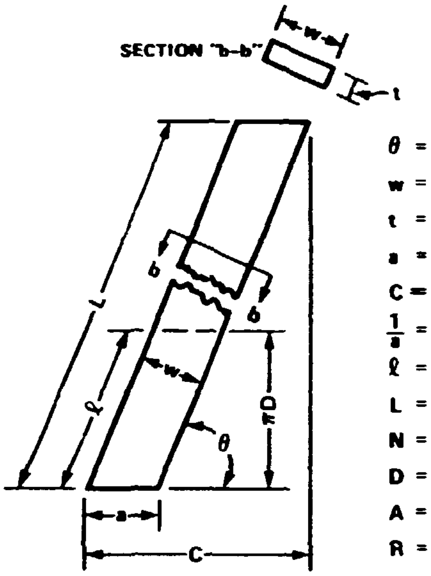

DEFINITIONS

θ = WINDING ANGLE
w = WIDTH OF HEATING ELEMENT
t = THICKNESS OF HEATING ELEMENT
a = AXIAL LENGTH OF WIDTH
C = AXIAL LENGTH OF HEATING ELEMENT
$\frac{1}{a}$ = TURNS PER CENTIMETER
ℓ = LENGTH OF RIBBON FOR 1 TURN
L = OVERALL LENGTH OF RIBBON
N = NUMBER OF TURNS IN COIL
D = PITCH DIAMETER OF COIL
A = CROSS-SECTIONAL AREA OF RIBBON
R = RESISTANCE OF HEATING ELEMENT

DERIVATIONS

$$\sin\theta = \frac{\pi D}{\ell} = \frac{w}{a},\ \cos\theta = \frac{a}{\ell} = \frac{w}{\pi D},$$

$$N = \frac{C}{a} = \frac{C\sin\theta}{w} = \frac{C}{\pi D}\tan\theta,\ L = N\ell = \frac{C}{\cos\theta},$$

$$A = \frac{\rho L}{R} = \frac{\pi D\,\rho\,C}{Rw},\ \text{SO}\ w = \frac{A}{t} = \left(\frac{\pi D\,\rho\,C}{Rt}\right)^{1/2}$$

Fig. 17. Considerations of winding a ribbon of length L on a pitch diameter D for an axial length C results in an equation that defines ribbon width in terms of material and dimensional properties.

ORNL DWG 80 5572A ETD

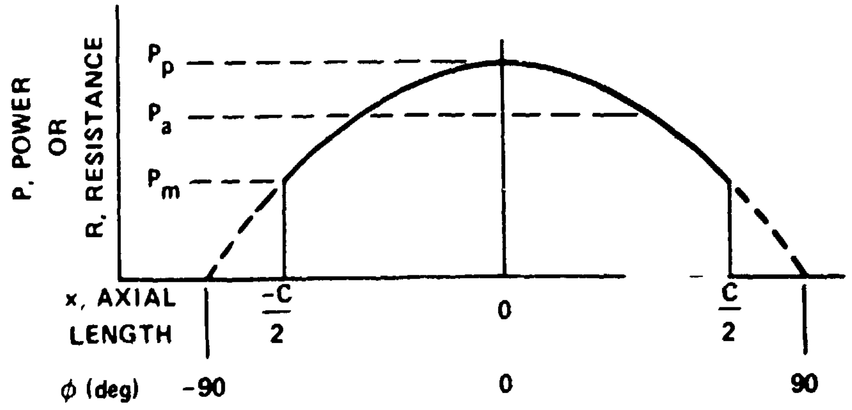

Fig. 18. Variable heat flux chopped cosine profile.

angle at P_m where $x = \pm C/2$ is now

$$\phi_m = \cos^{-1} (P_m/P_p) \ . \tag{4.4}$$

The profile can now be described within the chopped region by

$$P = P_p \cos \phi = P_p \cos \left[\frac{2x}{C} \cos^{-1} (P_m/P_p)\right] . \tag{4.5}$$

Equation (4.5) relates the chopped cosine profile analytically to the axial power variation.

Because current is constant through the heating element, power is proportional to resistance. The local peak resistance R_p is in the center of the profile and is given by

$$R_p = \frac{R}{C} \cdot \frac{P_p}{P_a} \ , \tag{4.6}$$

as shown in Fig. 18.

The ribbon width at the peak of the profile w_p (where $P = P_p$) can now be calculated from Eq. (4.2) by replacing R with R_p of Eq. (4.6) and taking C to be of unit length:

$$w_p = \left(\frac{\pi D\rho}{R_p t}\right)^{1/2} \ . \tag{4.7}$$

The design of a ribbon profile to give a specific axial heat flux distribution was first reported by D. L. Clark and T. S. Kress.[11] The local heat flux distribution was established to be

$$P = \frac{I^2\rho}{w^2 t} \ , \tag{4.8}$$

where P is the local power per unit area, w is the local ribbon width, and I is the current.

From Eq. (4.8), the local ribbon width w is

$$w = \left(\frac{I^2\rho}{Pt}\right)^{1/2} . \tag{4.9}$$

If Eq. (4.9) defined the power at some reference position, such as the center where $P = P_p$ and $w = w_p$ (Fig. 18), then the local width w, with respect to the reference width, is

$$W = \left(\frac{P_p}{P}\right)^{1/2} w_p . \tag{4.10}$$

Equation (4.10) can be used to establish the relative width anywhere along the ribbon. However, knowing just the width is not sufficient. The ribbon must be wrapped around a mandrel to form the coil of the desired diameter and length L. Figure 19 shows the uncoiled ribbon contour and the coiled configuration. For the coil to wind properly, the vertical

ORNL-DWG 80-5574A ETD

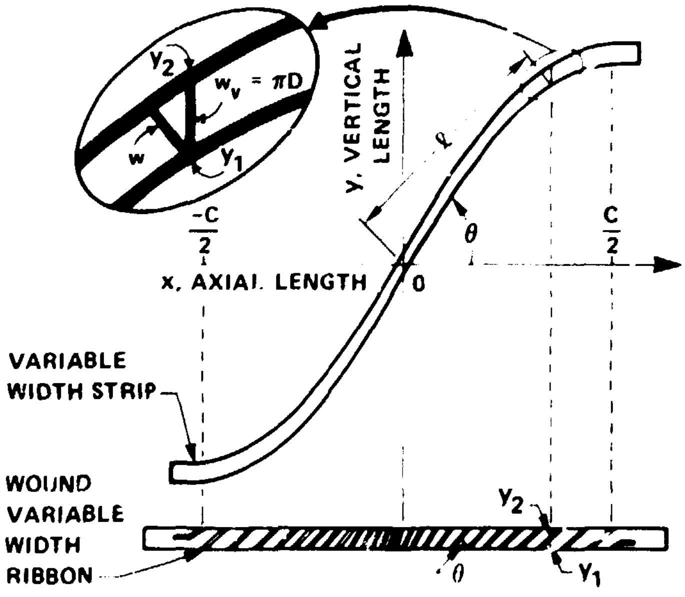

Fig. 19. Variable width contour is designed with a constant vertical width $W_v = \pi D$. Local width W varies with winding angle 0 to allow coil to be wound on a circumference πD with no variation in gap between turns.

contour angle θ must be the same on both sides of the ribbon at any position along the abcissa shown in Fig. 19. Thus, for the gap $G_v = 0$, the vertical component of the width of the ribbon w_v is constant and is

$$w_v = \pi D \ , \tag{4.11}$$

where D is the ribbon pitch diameter as defined previously. The local width w is given in terms of the contour angle θ by

$$w = \pi D \cos\theta \ , \tag{4.12}$$

or in terms of a reference angle θ_p at P_p, w_p by

$$\cos\theta = \left(\frac{P_p}{P}\right)^{1/2} \cos\theta_p \ . \tag{4.13}$$

The vertical contour or winding angle θ can now be determined in terms of the specific profile information by substitution of Eq. (4.5) into Eq. (4.13):

$$\cos\theta = \left[\frac{1}{\cos\left(\cos^{-1} P_m/P_p\right) \frac{2x}{C}}\right]^{1/2} \cos\theta_p \ . \tag{4.14}$$

Then local width w is calculated using Eq. (4.12). This defines the ribbon contour in terms of θ and w at any axial length x for $-C/2 \leq x \geq C/2$.

The final task is then to determine the ribbon length ℓ and the vertical length y in terms of x for a given ribbon contour and to compile the information in a form that can be used to generate magnetic tapes for machining and winding the ribbons.

From Fig. 4.8:

$$\ell = \frac{x}{\cos\theta} \ , \tag{4.15}$$

and

$$y = x \tan\theta \ , \tag{4.16}$$

where ℓ is the length of one turn. Equations (4.12), (4.14), (4.15), and (4.16) completely define the parameters of a variable width ribbon in terms of the axial length x. These data, computed from a programmable calculator, are then used as input to generate ribbon machining and winding control tapes.

4.2.2 Machining

The objective of the machining phase of ribbon development is to convert the ribbon contour information into ribbons of variable width that have a precisely controlled contour. The major requirements are to hold the width variation and the x and y locations describing the ribbon contour on the x-y plane (and therefore the angle) to within 1% throughout the ribbon length.

Early attempts to machine the ribbon contour on a numerically controlled (NC) horizontal milling machine were unsuccessful because (1) these tolerances could not be held, (2) excessive ribbon edge burring occurred, and (3) machine time per ribbon was excessive.

These difficulties prompted investigation of the use of grinding techniques to permit simultaneous fabrication of a number of heating elements stacked on the machine table. This method eliminated edge burrs and reduced fabrication time. Dimensional inaccuracies were overcome by using a high-precision NC template grinding machine (Fig. 20), which is equipped with a 50.8-cm-diam aluminum oxide grinding wheel with an adjustable vertical oscillating stroke, mounted on the y axis or main slide. It has been retrofitted with a vertical milling attachment that is mounted on the grinding wheel housing. However, the x axis or cross slide machine travel was only about two-thirds as long as was needed to machine current ribbon designs. This limitation was overcome by using a staging technique to effectively extend the cross slide travel from 137 to 245 cm. Thus, adequate slide travel was provided to machine the element contour of all design configurations of interest.

Ribbons are machined from strips of base stock up to 15.2 cm in width and 259.1 cm in length; up to 15 of these strips are stacked together and clamped between steel plates. Figure 21 shows the heating element geometry within the base stock.

Y-12 PHOTO
194617A

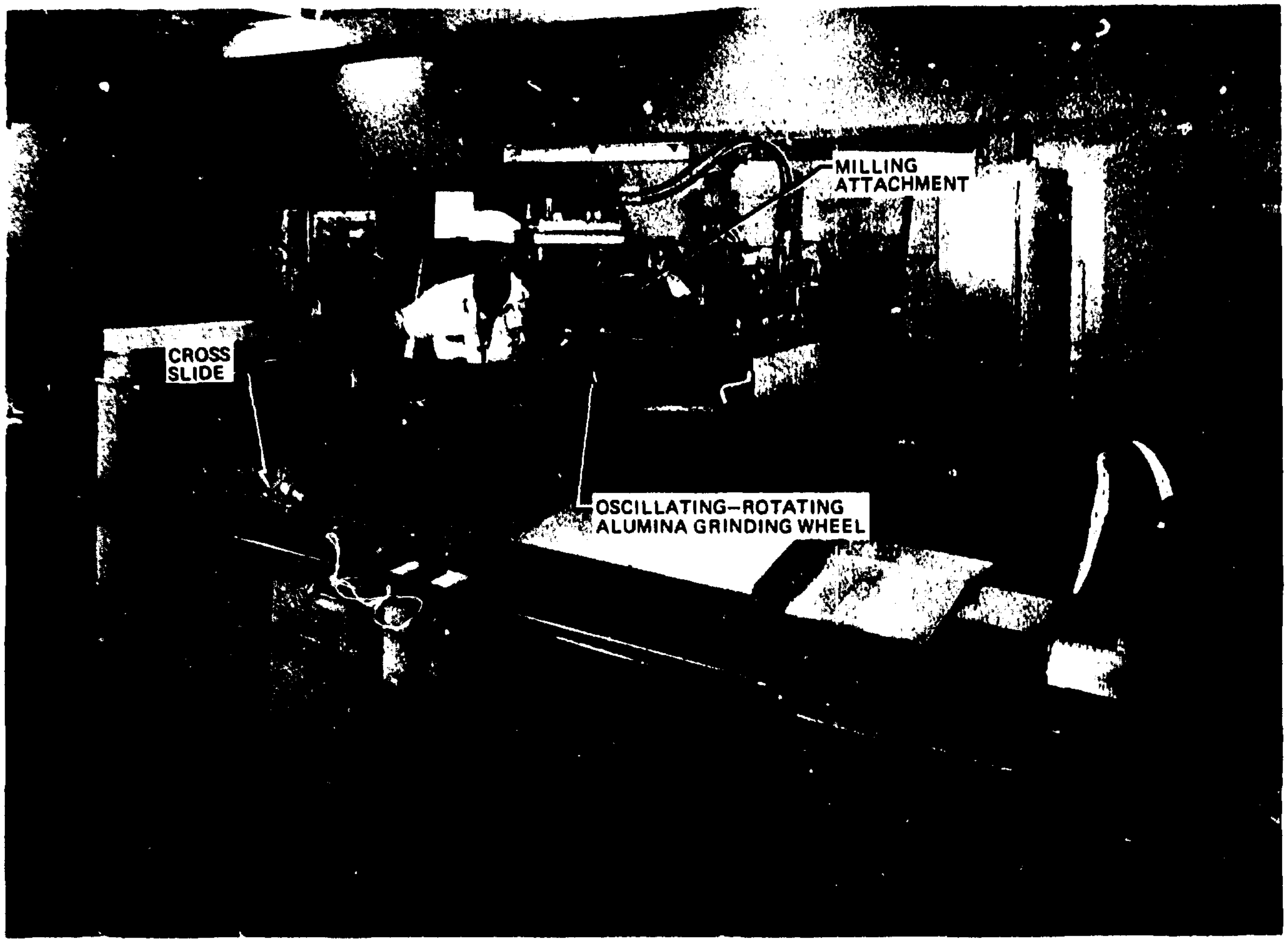

Fig. 20. Numerically controlled template grinding machine.

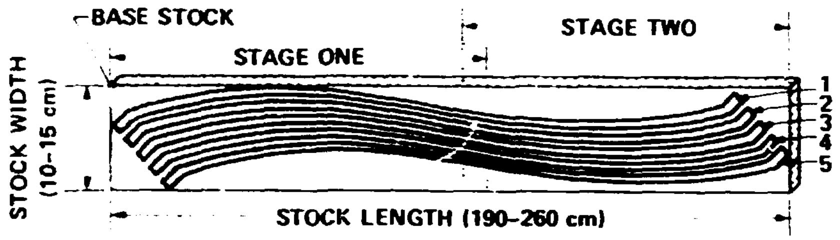

Fig. 21. FRS heating element geometry within ribbon stock.

As the figure shows, up to 5 sets of 15 stacked ribbons can be obtained from one stock assembly. The machining sequence is as follows:

1. The upper left surface of stack one is machined.
2. The upper right surface of stack one is machined.
3. The stack is reversed and remounted on the machine.
4. The region between stacks one and two is milled, and the first stack of 15 strips is separated from the rest of the assembly.
5. The upper left surface of the first stack is completed.
6. The upper right surface of the first stack is then machined, completing the first stack.

Stacks 2–5 are completed similarly, resulting in up to 75 ribbons with precisely controlled contours.

4.2.3 Winding

The variable width ribbons are formed into spirally wound coils on a stainless steel mandrel by a high-precision automated winding machine. To obtain reproducibility of coil parameters, the winding equipment must have a controllable variable lead rate (centimeters per revolution). This lead rate must be programmed to maintain a variable vertical speed defined by the variation in ribbon width at points along the ribbon contour. Rotational velocity remains constant throughout the process.

The Black-Clawson four-axis NC winding machine, depicted schematically in Fig. 22, was selected to fabricate the coils. Only the y axis and the θ axis motions are required for winding.

A typical coil winding operation uses an appropriately sized stainless steel rod loaded under tension between the headstock (machine base)

ORNL–DWG 80–5639 ETD

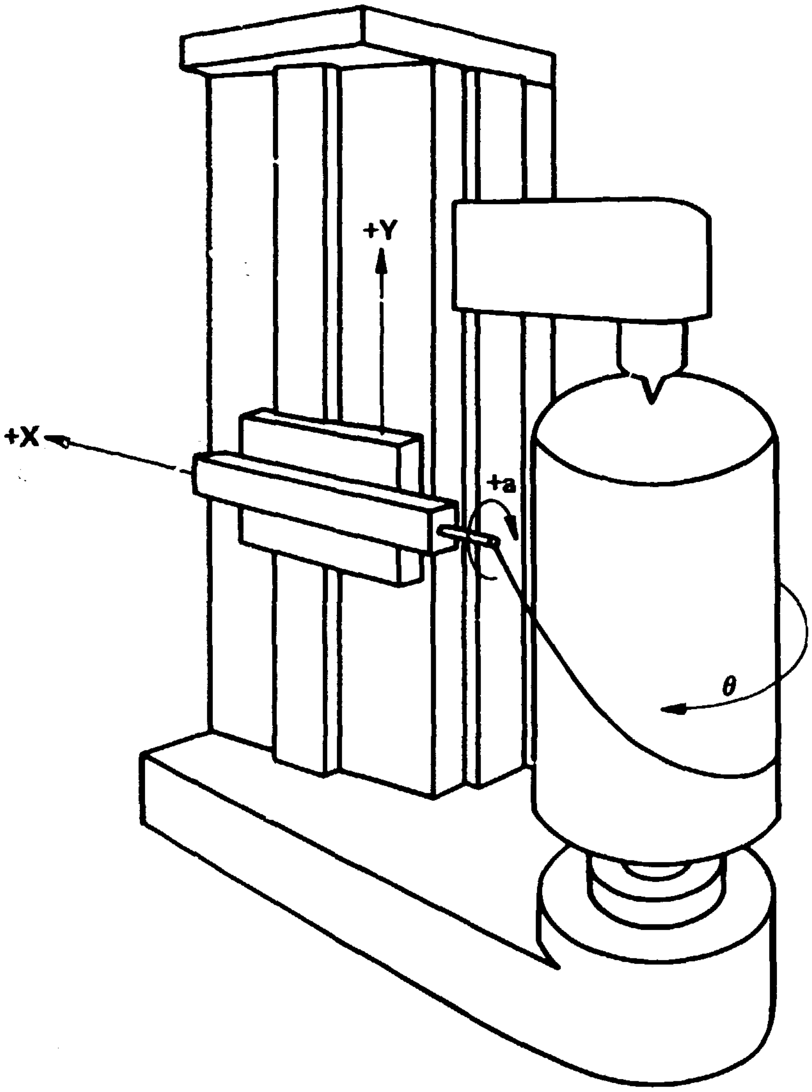

Fig. 22. Schematic layout of Black-Clawson winding machine.

and the tailstock. With a winding die attached to the machine ram, the headstock rotates as the ribbon is fed into the winding die. The die is advanced by the ram in a controlled vertical movement. Figure 23 depicts the machine in operation, and Fig. 24 provides a close-up of the headstock chuck and the coil winding die affixed to the machine ram.

4.2.4 Swaging and inspection

A final processing step, swaging, sets the coils to final dimensions and required tolerances prior to installation of the coils in the FRS.

Y-12 PHOTO
169102

Fig. 23. A variable width ribbon being wound into a coil. Inset shows how ribbon is formed on rotating mandrel by die.

Y-12 PHOTO
169106

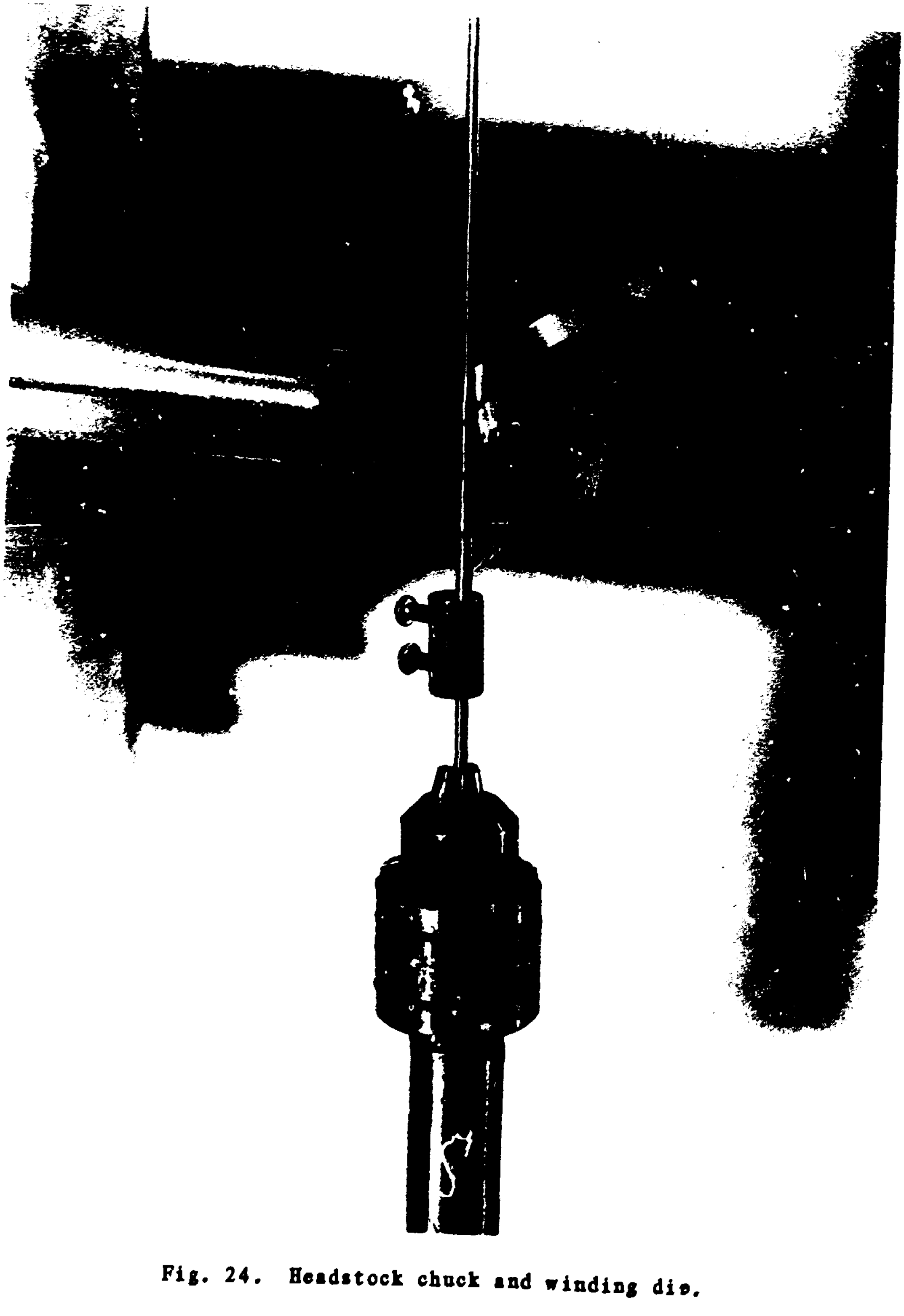

Fig. 24. Headstock chuck and winding die.

First, the coils are rewound tightly on a hard, stainless steel mandrel with the turns touching. Both ends are attached to the mandrel, one with a clamp and the other by spot welding. The coil is then carefully swaged to lock it into this configuration. After swaging, it is removed from the mandrel. Swaging supplies cold work to the coil to lock the turns in place, sets the required diameter, removes the concavity introduced by winding, and decreases the surface roughness.

Additional cold work put into the coils by swaging makes them rigid and mechanically similar to a spring. Then, gaps between turns are produced by stretching the coil about 5% of its length. The coil does not plastically deform under these conditions; thus, the gaps between turns no longer depend on the local material yield stress and are quite uniform. The coil OD can be controlled to within ±0.013 mm using this method.

Coils are dimensionally inspected with a micrometer, cleaned in a vapor degreaser, and cut to the exact length after swaging. To maintain a symmetrical chopped cosine profile, equal amounts of material are cut off each end.

Infrared scanning techniques were used to evaluate how well the heat flux distribution produced by the coils fits the design criteria. The most acceptable technique for coil evaluation is (1) to paint the coil with a black paint (to increase surface emissivity), (2) to insert a close-fitting insulated arbor into the center, (3) to stretch the coil on the arbor about 2% of its length, and (4) to scan it after applying a power of about 25 W for 4 min. Much more sensitive analysis of coils is possible by using higher power, shorter time scans, and/or by close, narrow range scans. The 25-W, 4-min scan of a bare coil was determined to be comparable to the 1-s core transient infrared scan commonly used in FRS inspections. These inspections indicate that coil OD variations of ±0.025 mm and coil gap variations of 0.05 mm are acceptable from a thermal profile standpoint.

5. SMALL-DIAMETER THERMOCOUPLE DEVELOPMENT

5.1 General

Each CFTL FRS is fabricated with six (four in earlier FRSs) type K thermocouples with insulated junctions (Fig. 2). These thermocouples are the primary means for obtaining thermal-hydraulic information in the CFTL. They are required to measure high temperatures (up to 1100°C) and encounter severe thermal transients (up to 100°C/s) during simulated reactor accidents in the CFTL. These extreme requirements, in addition to operational life requirements of up to 1000 h, place severe demands on the thermocouples.

This section delineates development efforts to improve the reliability of these thermocouples. Examination of thermally cycled thermocouples along with investigations of their time and temperature behavior yielded three criteria for improvement of thermocouple lifetime. Methods to eliminate thermocouple prestrain, reduce impurity content, and refine thermoelement grain size were developed. A new draw and anneal process was defined to enable manufacture of refined-grain-size thermocouples on a production basis.

Table 22 summarizes the requirements of the CFTL FRS thermocouples. As reported in Sect. 4, the thermocouples and FRS were qualified by operating the FRS at various steady-state conditions from 300 to 1100°C for 100 to 200 h, including 40 h at 1100°C. It was then subjected to more than 2000 thermal cycles for a total operation time of about 1000 h. Thermal transients were normally from 10 to 50°C/s, and the temperature changes during cycling were from 150 to 600°C.

In the early stages of our program aimed at providing reliable small-diameter thermocouples, we tested four swaged FRSs into which 13 (total) small-diameter insulated-junction thermocouples had been installed. About 1200 h of steady-state and transient-cycling tests were conducted on the four FRSs, and over 1000 thermal transients were conducted on one of them having four thermocouples. Most thermocouples failed in the initial steady-state portion of the tests. Those thermocouples that did survive the steady-state tests failed within a few hundred transient cycles.

Table 22. FRS thermocouple requirements

Type	K (Chromel-Alumel)
Sheath	Inconel 600
Insulation	MgO
Junction	Insulated
Length, mm	1550 to 2750
Diameter, mm	0.51
Lifetime, h	1000 minimum
Time at 1100°C, h	40
Time above 1100°C, min	~10
Thermal cycles	2000 minimum
Cycling range	
Normal, °C	300 to 800
<10 cycles, °C	300 to 1370
Ramp rate, °C/s	1 to 100
Accuracy, °C	±8 to 800 ±15 from 800 to 1370

Failure in all cases was by development of an open circuit in one or both of the thermoelements (Chromel or Alumel) at elevated temperatures. When the FRS temperature was lowered, the thermocouples would again become operative. Photomicrographs of failed thermocouples showed voids at the grain boundaries of both thermoelements, and both were extremely brittle.

These negative results prompted investigation into the causes and mechanisms for failure. Our investigations were primarily directed toward lifetime improvement. Previous work by Potts and McElroy[14] and by Anderson and Kollie[15] showed that small-diameter thermocouples are susceptible to metallurgical, chemical, and mechanical changes that affect both lifetime and accuracy.

5.2 Thermocouple Investigations

To understand the factors that contribute to the premature failure of small-diameter thermocouples, both their structure and metallurgical state must be considered.

A thermocouple consists of two thermoelements, an insulating material and a metal sheath (Fig. 2). One thermoelement is Chromel-P* (the K+ alloy), a nickel-based alloy having chromium as the major alloying element. The other thermoelement is Alumel* (the K- alloy), a nickel-based

---

*Trade names of the Hoskins Manufacturing Company.

alloy containing aluminum as the major alloying element. The final grain size of both thermoelements is specified for CFTL use to be ASTM microgram size 7 (0.33 mm) or smaller. Thermoelement wires are contained in an MgO insulation having a particle size of ASTM micrograin size 7 or smaller. The sheath is Inconel 600,* a nickel-based alloy. The thermoelement wire diameter, the insulation between thermoelements and the sheath, and the sheath thickness are 0.0508 to 0.0762 mm. Thus, the thermoelement grain size and wire diameter are such that as few as two to six grains traverse the entire thermoelement cross section. Grain boundaries represent material discontinuities and are relatively weak and brittle compared with the rest of the material, especially at high temperatures;[16] regions along the thermoelement with large grains are, therefore, weak points within the structure.

Another closely related factor influencing lifetime is that of thermal stresses arising from differential thermal expansions between the thermocouple components and other FRS components. Figure 25 (Ref. 2) gives a comparison of thermal expansion of the 316 stainless steel alloy used as the FRS cladding, the Inconel 600 thermocouple sheath material, and the Chromel and Alumel thermoelement materials. At 1000°C, the 316 stainless steel alloy clad has expanded 20% more than the Chromel thermoelement and 30% more than the Alumel thermoelement. The thermocouple is intimately associated with the much more massive FRS clad, and both thermoelements are put into tension as temperatures are increased. These tensile forces, imposed on grains only slightly smaller than the thermoelement lead wires, are major contributors to premature thermocouple failure.

A third contributing factor is that of oxidation. Spooner and Thomas,[17] operating bare Chromel and Alumel in various environments, found that oxidation of both Chromel and Alumel thermoelements resulted in embrittlement and early failure, especially when the thermocouples were operated in the temperature range of 815 to 1038°C. They state that elimination of oxygen from the insulation matrix will extend the thermoelement lifetime indefinitely and speculate that operational temperatures close to the material melting point may be possible.

---

*Trade name of the International Nickel Company.

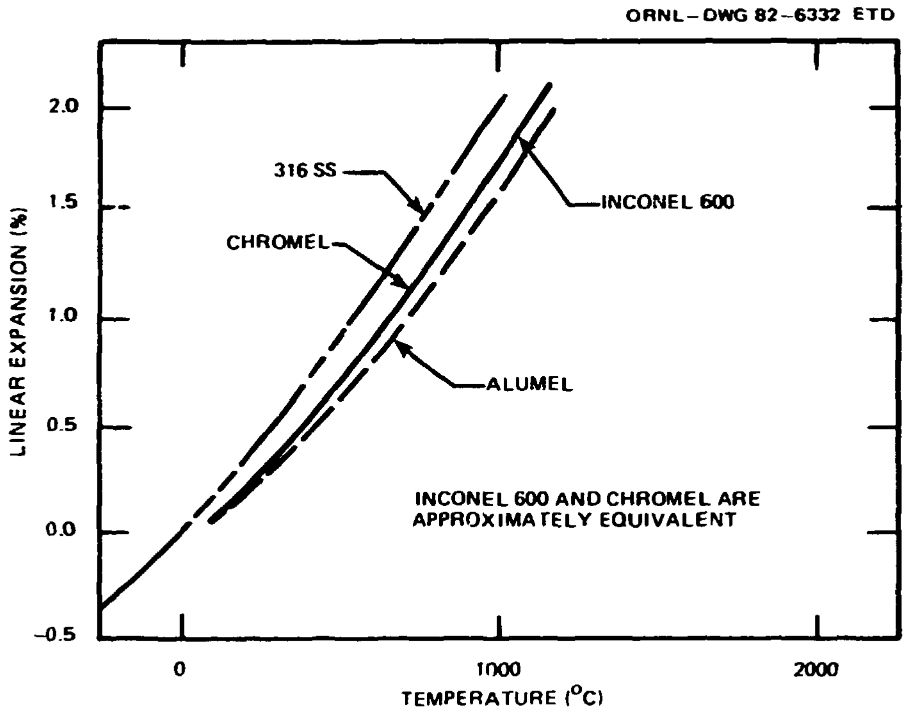

Fig. 25. Average linear thermal expansion of materials for CFTL FRS cladding and thermocouple components.

A final factor that has been found to make thermocouples susceptible to both early failure and temperature measurement errors is residual cold work, or prestrain, in the material prior to its use at temperatures above its recrystallization temperature.

Potts and McElroy[14] have shown the importance of a fully recrystallized microstructure, free of material cold work, as the final fabrication step for type K thermoelements. Cold working changes the thermal electric sensitivity of the material, and, during use in an FRS, the cold worked material will be annealed, again changing the thermal electric sensitivity. Such changes cause temperature measurement errors.

In addition to causing errors, small amounts of cold work have been shown to cause relatively large increases in grain size when a material recrystallizes, possibly by a factor of 2 or 3 for low values of cold work.[16] Figure 26 illustrates the effect of cold work on recrystallized grain size. With thermoelement grain size already on the order of the

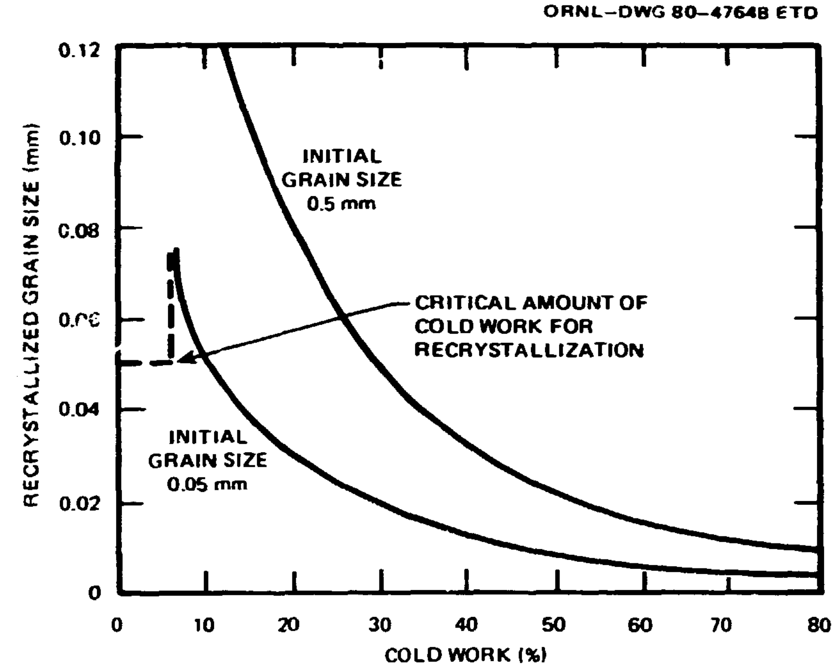

Fig. 26. Schematic curves of recrystallized grain size vs amount of cold work before recrystallization.

wire diameter, prestrain clearly should be avoided, if only to preserve a small grain size.

Anderson conducted tests to determine the combined effects of grain size, prestrain, and differential thermal expansion on thermocouple lifetime.[2] Material from two manufacturers was used. The first had a grain size of ASTM 7-8, and the second had a grain size of ASTM 6-7. Test samples were prepared by collapsing 1.5-mm-diam stainless steel tubing over a length of 0.5-mm-diam thermocouple material. The clamping of the collapsed tubing to the OD of the thermocouple sample was intended to simulate the strong mechanical connection that exists between the FRS cladding and thermocouples. The collapsed tubing was electrically heated through various thermal cycles, and the loop resistance of the samples was monitored.

Those samples with the smaller grain size (ASTM 7-8) were found to endure about 5000 cycles before failure, or two to three times the number imposed on those with the larger grain size. Also, prestraining the samples 5% prior to thermal cycling reduced their lifetime by a factor of 2.

Photomicrographs of most of the test samples showed void formation at the grain boundaries, as had our earlier photomicrographs. Anderson attributed these voids to aluminum and chromium oxides that apparently formed at the respective grain boundaries and were removed by metallographic sample preparation. In Anderson's findings (as well as ours) samples with voids were extremely brittle. This brittleness was attributed by Ludwig[19] to the brittle oxides that formed at the grain boundaries.

A quite different explanation of grain boundary voids has been offered by Dyson and Henn[20] and by Dyson and Rodgers.[21] They found in a study of a nickel-based alloy that prestrain introduces microcracks that nucleate to form grain boundary voids when the material is subsequently heated above its recrystallization temperature. Furthermore, the effect of stress is to enhance the formation of voids. Prestrain values of about 2% reduced the elongation-to-fracture of samples by a factor of 2 (Ref. 20), indicating that even small values of prestrain result in grain boundary voids.

Although not specified, most thermocouples are received with a residual cold work of 1 to 3%,[14] presumably to adjust the thermoelectric sensitivity to meet the calibration curve. Further, as part of their assembly into an FRS, the thermocouples are strained an additional 0.5%. Thermocouples assembled into the earlier swaged FRSs were prestrained an additional 4 to 5% by the swaging process. Thus, the thermocouples in a swaged FRS (like those initially tested) have a prestrain of 5.5 to 8.5%, and those in nonswaged FRSs have a prestrain of 1.5 to 3.5%.

As the effects of prestrain were surfacing, the design of the CFTL FRS was evolving toward use of the nonswaged fabrication technique, which, by its nature, reduced thermocouple prestrain to a level below which recrystallization occurs (Fig. 26). We had also incorporated a period of low-temperature operation at ~350°C for 1 to 2 d as part of the operational sequence. After these changes were adopted, lifetime tests of thermocouples in nonswaged FRSs were extremely successful, although there was still evidence of decalibration. Eight nonswaged FRSs with 27 thermocouples endured over 5,000 h of steady-state and transient testing, including over 36,000 thermal transient cycles. No thermocouples failed prior to

FRS failure, even though 4 rods endured more than 4,000 to 10,000 transients, many as severe as 50°C/s.

Figure 27 (samples a and b) compares photomicrographs of the Alumel thermoelement from a swaged FRS prototype and a nonswaged FRS prototype, respectively. Both FRSs endured about 1000 h of steady-state and transient operation and over 2000 thermal cycles. Sample 5.3(a) failed after ~200 h of steady-state operation and 400 thermal cycles, while sample 5.3(b) did not fail. Sample 5.3(a) was extremely brittle, but sample 5.3(b) was ductile even though the grains were relatively large.

ORNL PHOTO 0489-82R

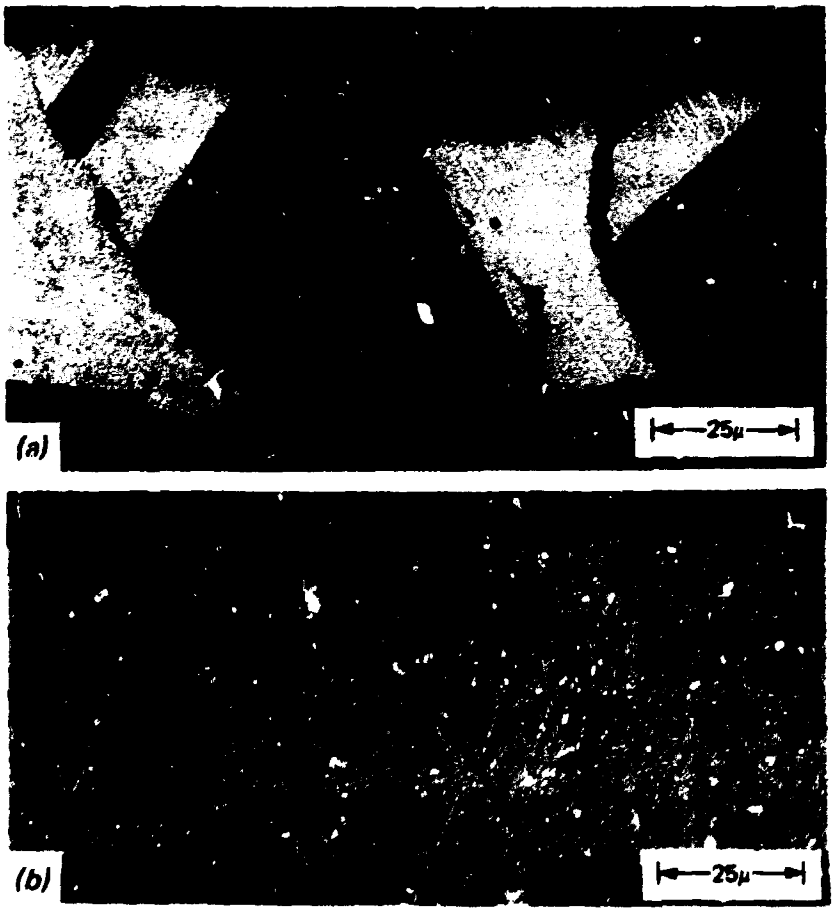

Fig. 27. Photomicrographs of Alumel thermoelement samples from (a) a swaged FRS and (b) a nonswaged FRS, both of which endured ~1000 h of operation with more than 2000 thermal cycles. Voids in sample render it very brittle, while the void-free sample is ductile.

Thus, while oxidation contributes to failure and should be minimized, we feel the major cause of premature failure of small-diameter thermocouples is prestrain-induced grain growth and grain boundary void growth, causing reduced thermoelement cross-section and grain boundary embrittlement.

From the thermocouple investigations we concluded that the thermocouples must have three characteristics if they are to meet CFTL operational requirements:

1. There must be a minimum of oxygen and moisture as well as hydroxides [such as $Mg(OH)_2$] or oxides (such as iron oxide) inside the thermocouple sheath. This requirement will help to reduce the source for oxidizing the chromium or aluminum in the thermoelements.
2. The final grain size of both thermoelement wires must be very small, with a recommended maximum of ASTM micrograin size 9 (~4440 grains/mm² or 0.016-mm diameter).
3. The thermoelements must be fully annealed when received. Any ensuing cold work occurring during fabrication of the FRS should not exceed 1% and should be removed prior to operating the thermocouples at or above their recrystallization temperature.

Adequate purity of thermocouple insulators can be achieved by a 1000°C, $\leq$10-μm vacuum bakeout prior to their assembly into the thermocouple sheath, followed by assembly of the thermocouple bulk material in an inert atmosphere. Satisfactory grain size of thermoelement materials can be achieved by optimization of the thermocouple fabrication process (Sect. 5.3), and a structure free of cold work can be obtained by (1) a recovery anneal below the material recrystallization temperature or (2) an anneal above the recrystallization temperature if the residual cold work is not in the critical range where thermoelement grain size might be adversely affected.

Groth-Mazur Industries of Addison, Illinois, was chosen to be the CFTL FRS thermocouple manufacturer. We provided guidance to GMI and conducted evaluations to ascertain that the three above characteristics would be met.

The purity requirement was not easily accommodated. Discussions with GMI personnel revealed that they intended to use their normal bakeout procedure (at ambient pressure and 200°C) on the insulators for this group of thermocouples and further that they intended to anneal the bulk thermocouple material (BML) after each reduction by drawing (~10% area reduction in most cases). Because there are known hydroxides that do not break up until well above this 200°C temperature (specifically as high as 900°C), it was apparent that such hydroxides would subsequently be available for oxidation of both chromium and aluminum. As a consequence, we obtained samples of insulators from GMI in both the "as-received" and "as-processed" conditions. These samples, when subsequently baked out in a vacuum furnace at ORNL, revealed a lower level of outgassing at low temperatures (<400°C) for the as processed insulators but also revealed subsequent release of CO_2, H_2, and other gases at temperatures up to about 950°C. On the basis of these results, GMI agreed to establish a high-temperature vacuum bakeout system and to load the MgO insulators into the BML sheath inside a glove box under argon cover gas.

The requirement for eliminating cold work from the as-received thermocouples was adequately achieved because the thermocouple specification required a 48-h "ordering" bakeout. This low temperature heat treatment was specified to order the Chromel thermoelement for measurement error reduction.[15] When conducted as specified on material that had been fabricated by procedures designed to optimize thermoelement grain size (discussed below), this heat treatment effectively removed any residual cold work.

5.3 Grain-Size Refinement

Achieving the required grain size was more difficult, however. The specification requires a maximum grain size of ASTM 7 (32-μm average diameter) for both thermoelements. Historically, this requirement has been difficult to attain; only one thermocouple manufacturer has had reasonably uniform success in achieving it. Initial samples from GMI were evaluated by ORNL, and it appeared likely that GMI would not meet the grain size requirement using normal fabrication processes. Therefore, ORNL worked closely with GMI, in their facility, to improve the process.

The development effort optimized both the drawing and annealing processes to achieve the finest grain size possible consistent with reasonable production times and material yields. A brief review of recrystallization and drawing theory as it pertains to thermocouple fabrication is warranted before discussing process development.

5.3.1 Recrystallization and drawing

Recrystallization. Material recrystallization is a nucleation and growth phenomenon, the completion of which is dependent on annealing temperature, time, and cold work performed before annealing, as well as on composition variations. A schematic representation of the effect of prior cold work and initial grain size before cold working on the recrystallized grain size is shown in Fig. 26. The schematic suggests that a large amount of cold work is desired to refine grains by subsequent recrystallization; small amounts of cold work must be avoided unless they are too small to initiate recrystallization.

Because it is a nucleation and growth process, the amount of material transformed during recrystallization follows a sigmoidal distribution with time.[6] The time at temperature generally follows an Arhennius-type relationship with the material activation energy as the exponential variable.

If the grain size of two materials is to be minimized and if they must be annealed at the same temperature (as is the case with the Chromel-Alumel system in a thermocouple), then the amount of recrystallization of the material with the highest activation energy (Chromel) determines the annealing time. Thus, the extent of recrystallization necessary for subsequent cold working of that material without fracture must be determined. This amount of recrystallization will determine the annealing time for the system and, therefore, the grain size of the material with the lowest activation energy (Alumel).

Drawing. Reference 22 provides an excellent review of drawing theory, part of which is presented here. The general equation for drawing is

$$\sigma_d \approx (1/\eta) \int \sigma \, de \,, \qquad (5.1)$$

where

σ_d = draw stress,

σ = material stress at ε,

η = process efficiency,

ε = true strain in drawing (cold work).

For materials that obey the strain-hardening power law,

$$\sigma = K\varepsilon^n , \tag{5.2}$$

where K is a strength coefficient and n is the strain-hardening exponent. In this case, Eq. (5.1), after integration, becomes

$$\sigma_{d_1} = \sigma_{\varepsilon_1}\varepsilon_1/\eta(n + 1) , \tag{5.3}$$

and for a second-draw psss, becomes

$$\sigma_{d_2} = (\sigma\varepsilon_2\varepsilon_2 - \sigma\varepsilon_1\varepsilon_1)/\eta(\eta + 1) , \tag{5.4}$$

where σ_ε is the flow stress of the material exiting the die, and

$$\varepsilon = l\eta(A_0/A_1) , \tag{5.5}$$

where A_0 and A_1 are the entering and exiting areas, respectively.

Figure 28 shows typical material stress and strain plots during steady-state drawing as described by Eq. (5.3). The material flow stress σ increases in accordance with Eq. (5.2) and is σ_ε at the die exit. The material is strained to $\varepsilon = \ln A_0/A_1$ at the die exit, and the draw stress σ_d acts on the reduced, strain-hardened material.

Figure 29 shows the drawing operation for a first draw described by Eq. (5.3) for $\eta < 1$ and $\eta = 1$ as well as Eq. (5.2) for the material. The material is influenced by the draw die as it passes through but is again in pure tension, in a work-hardened state, as it exits. It is normally work hardened enough so that it will neck and break if it yields. To prevent this, σ_d must be less than σ_ε so that the drawing limit is reached when $\sigma_d = \sigma_\varepsilon$. This is shown in Fig. 29 as the intersection between the

ORNL-DWG 81-16141ETD

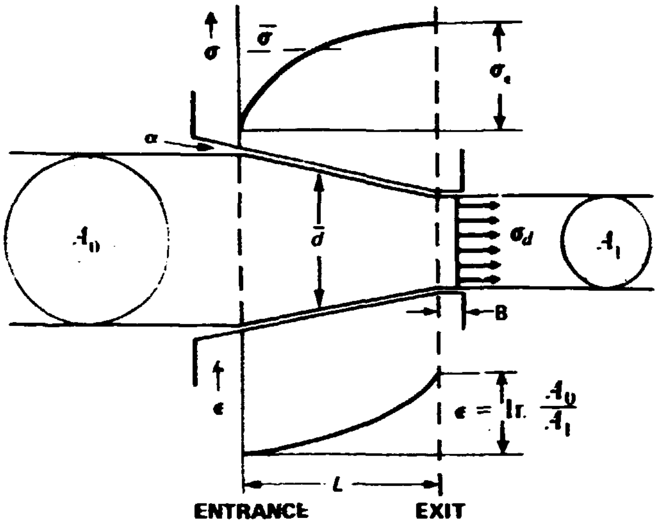

Fig. 28. Steady-state drawing operation.

ORNL-DWG 80-47668 ETD

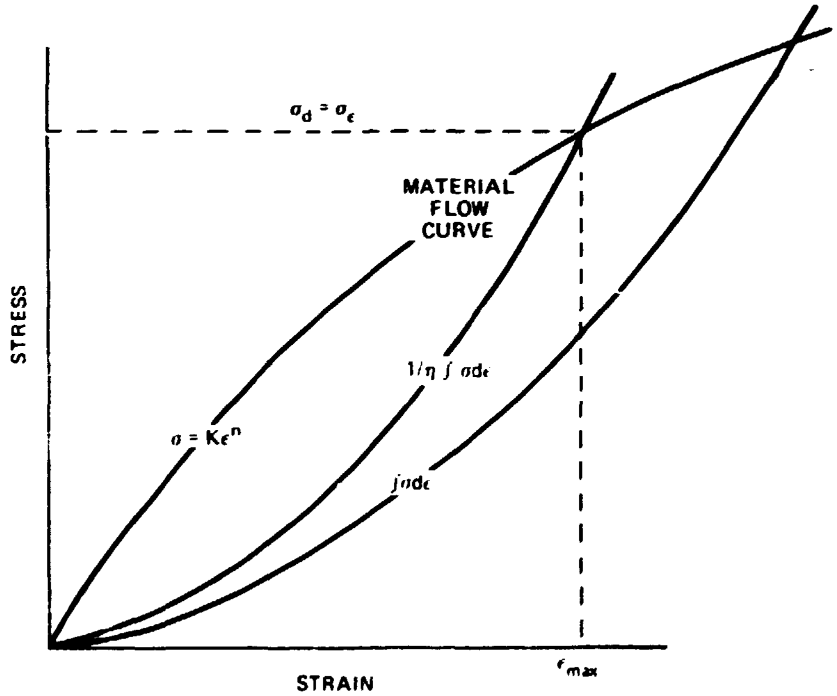

Fig. 29. Flow-curve (Kϵ) for a solid wire exhibits strain hardening as well as work curve for ideal ($\int \sigma d\epsilon$) and typical ($1/\eta \int \sigma d\epsilon$) drawing process.

σ_d and σ_g curves. For this case, Eq. (5.3) becomes

$$[\varepsilon_{max}]_{draw} = \eta(n + 1) \ . \qquad (5.6)$$

For pulling in pure tension,

$$[\varepsilon_{max}]_{pull} \approx n \ . \qquad (5.7)$$

Comparison of Eqs. (5.6) and (5.7) indicates that a maximum additional 100% elongation is possible with drawing as compared with pulling in pure tension. The amount achieved depends on η, the drawing efficiency. For a second drawing pass, the material flow curve would start at σ_g, and, because the material is strain hardened, the σ_{d_2} curve would rise more sharply so that $(\varepsilon_2 - \varepsilon_1) < \varepsilon_1$.

The drawing efficiency η has been shown to depend only on the product of process frictional and redundant work terms and is given as[22]

$$1/\eta = f\phi \ , \qquad (5.8)$$

where the process frictional work term is

$$f = (1 + \mu \cot \alpha) \ , \qquad (5.9)$$

and the redundant work term is

$$\phi = [1 + C(\Delta - 1)] \ , \qquad (5.10)$$

where

C = a constant (0.12 for wire),

μ = coefficient of friction,

α = draw die semiangle,

Δ = deformation zone geometry factor $\cong \bar{d}/L$ (Fig. 29).

From Eqs. (5.8–5.10), the process efficiency depends only on Δ, μ, and α. To maximize the total cold work ε between anneals, the product of the factors containing α and Δ must be minimized. (The friction coefficient μ depends primarily on the lubricant. Many factors go into its selection, and although some investigations were conducted, to further minimize μ was beyond the scope of this work.)

Process parameters α and Δ are related by

$$\Delta = \frac{\pi}{180}\,\alpha\,\frac{(1 + e^{-\varepsilon/2})^2}{(1 - e^{-\varepsilon})}\ . \tag{5.11}$$

The friction factor [Eq. (5.9)] asymptotically decreases with increasing α, whereas the redundant factor [Eq. (5.10)] linearly increases with Δ so that their minima is reached at some intermediate value of α and corresponding Δ.

5.3.2 Application to thermocouple drawing – the internal stress factor

The preceding analysis is adequate to arrive at optimum conditions for drawing of wire. For thermocouple drawing, however, drawability is normally limited by one of the internal thermoelements breaking (open circuiting). The drawing process must, therefore, be optimized based on the cold work and stresses occurring on these internal components. The friction factor [Eq. (5.9)] results from die-to-thermocouple surface forces; it should be independent of ε and can only influence the mean draw stress, not the radial stress distribution across the thermocouple.

The redundant term, however, has as its basis the occurrence of nonuniform die pressure and resultant internal stress and strain distributions as functions of the deformation zone geometry factor Δ. Figure 30 schematically represents stress and strain distributions as they might appear across a thermocouple cross section for $\Delta = 3$. The strain plot was extrapolated from hardness data[22] on lubricated wire for $\Delta = 6.9$ and lubricated strip for $\Delta = 4$, both with a true strain or cold work for $\varepsilon = 0.17$. From the plot, cold work can be seen to have a large variation across the cross section and is at a minimum internally. The average strain $\bar{\varepsilon}$ is increased above ε for the nonuniform distribution by the value of ϕ given in Eq. (5.10). For $\Delta = 3$, the average cold work on the thermoelements is

ORNL-DWG 81-16331 ETD

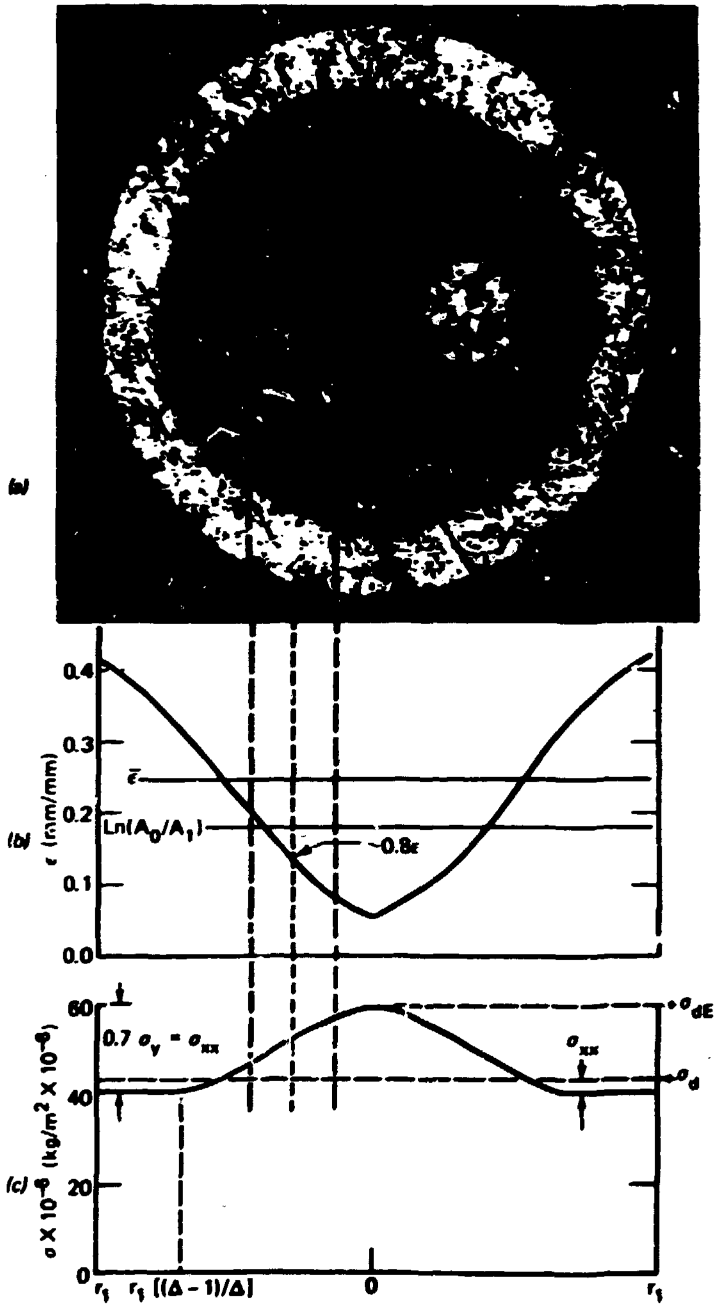

Fig. 30. Schematic representation of radial stress and stress pattern across a thermocouple drawn with $\Delta = 3$ and $\varepsilon = 0.17$. Average strain is increased to ε by nonuniform distribution, and strain of thermo-element is about 0.8ε. Internal stress is maximum in center and depends on yield stress as well as Δ.

only about 0.8 ε, while the sheath incurs ~2 ε. As Δ decreases towards one, the strain distribution becomes uniform. The implication is that low Δ drawing is more suitable to thermocouples if internal cold work is to be maximized as needed to refine thermoelement grain size.

The stress distribution of Fig. 30(c) further reinforces this notion. The distribution shown was derived from Hill's[23] slip-line field analysis (for frictionless plain-strain compression of a nonhardening material) and from Backofen's[22] maximum stress distribution analysis of Hill's data. Backofen showed that the variation in the internal stress distribution σ_{xx} from surface to center followed the same relationship with Δ as did the ratio of die pressure to surface yield stress ($\bar{P}/\sigma_y$) reported by Hill. The maximum in this internal stress variation is given by

$$\sigma_{xx_{max}} = 2\ \sigma_y\ \lambda\ , \tag{5.12}$$

where λ is the deformation zone slip-line apex angle and is 0 for $\Delta = 1$ and 0.43 π for $\Delta = 8.75$. By interpolation, the maximum centerline to surface stress with Δ is then

$$\sigma_{xx_{max}} = 0.35\ \sigma_y\ (\Delta - 1)\ . \tag{5.13}$$

The stress distribution shown in Fig. 30(b) for $\Delta = 3$ is constant from the surface inward for a distance $L/2 \cong r_1/\Delta$ (where L is as shown in Fig. 28), then rises approximately linearly to a maximum of ~0.7 σ_y (σ_y = 28 x 10^6 kg/m²) at the center. The draw stress σ_d is ≈0.1 σ_y larger because of this distribution, and the internal stress σ_{dE} is

$$\sigma_{dE} = \sigma_d + \sigma_\gamma = \sigma_d\gamma\ , \tag{5.14}$$

where

$$\sigma_\gamma \cong 0.35\ \sigma_y\ (\Delta - 1)\left[1 - \frac{2}{3}\left(\frac{\Delta - 1}{\Delta}\right)^2\right]\ , \tag{5.15}$$

and the internal stress factor γ is

$$\gamma = 1 + \frac{\sigma_\gamma}{\sigma_d} \ . \tag{5.16}$$

Equation (5.3) for the first draw in terms of the internal stresses now becomes

$$\sigma_{dE_1} \cong \phi_1 f_1 \gamma_1 \frac{\sigma_{\varepsilon_1} \cdot \varepsilon_1}{n + 1} \ . \tag{5.17}$$

If there is to be a second draw of the same material, the stress distribution of the first draw must be taken into account. This distribution σ_{xx} is additive to the internal stress developed in the second draw. However, for $\Delta \leq 2$ on the first draw (which should normally be the case), $\overline{\sigma_{xx}} \ll \sigma_{xx}$ so that $\sigma_\gamma \cong \sigma_{xx}$ and the internal stress distribution can be accurately represented by σ_{γ_1}. A second distribution described by Eq. (5.15) is developed for the second draw, which results in σ_{γ_1}. The internal stress after the second draw is the sum of these two stresses. Equation (5.4) for the second draw, in terms of the internal stress, becomes

$$\sigma_{dE_2} \cong \phi_2 f_2 \gamma_2 \frac{(\sigma\varepsilon_2\varepsilon_2 - \sigma\varepsilon_1\varepsilon_1)}{(n + 1)} \ , \tag{5.18}$$

where γ_2 is now

$$\gamma_2 = 1 + \frac{\sigma_{\gamma_1} + \sigma_{\gamma_2}}{\sigma_{d_2}} \ . \tag{5.19}$$

Equations (5.3) and (5.4) for the draw stress and Eqs. (5.17) and (5.18) for the internal stress together enable complete modeling of the thermocouple drawing process. In their application to thermocouple drawing, the assumptions of nonstrain hardening and homogeneity must be recognized, although the ability of the model to predict and improve the process will ultimately determine its usefulness. The strain-hardening assumption, although intended for nonstrain-hardening material, was shown by

Backofen to still provide a reasonable upper-bound estimate of redundant strain properties of strain-hardening materials.[29] The effect of nonhomogeneity will be discussed in the next section.

To examine the internal stress as the limiting parameter in thermocouple drawing, the friction, redundant, and internal stress factors in Eqs. (5.17) and (5.18) must be calculated for various α and Δ. Figure 31 plots the $\phi f \gamma$ product of Eq. (5.17) as a function of α for various amounts of cold work (ε). The deformation zone geometry factor Δ was determined for each α using Eq. (5.11). The draw stress σ_d was determined using Eq. (5.3), and K and n in Eq. (5.2) were determined to be 137.0 x 10^6 kg/m^2 and 0.16, respectively, from tensile tests of Inconel-sheathed, type K thermocouples.

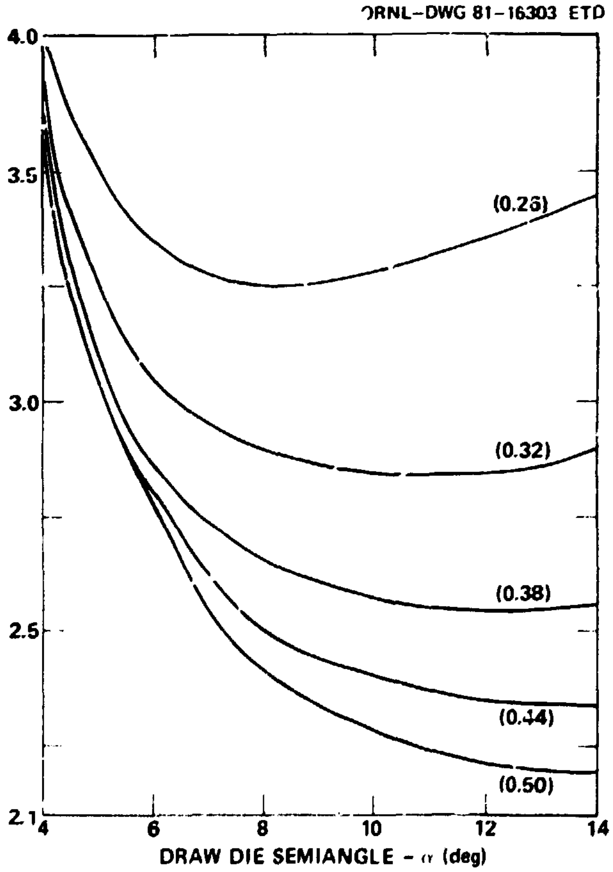

Fig. 31. $\phi f \tau$ product vs draw-die semiangle at various amounts of cold work (μ = 0.19).

The $\phi f\gamma$ product acts as a multiplier to the useful work in drawing $\int\sigma d\varepsilon$, which results in the internal stress σ_{dE}. As the useful work increases (with ε) the efficiency $\eta_\varepsilon = 1/\phi f\gamma$ improves. Figure 31 and Eq. (5.3) indicate that a first draw of $\varepsilon = 0.44$, with α between 10 and 12° and Δ between 1.6 and 1.9°, is optimum and will give a σ_{dE}-to-σ_ε ratio of ~0.7, adequate to account for process and model uncertainties.

Additional cold work before annealing can be obtained with a second draw. However, the cold work is less and process parameters are much more critical (Fig. 32). The internal stress, resulting from redundant strain and characterized by Δ, dominates the process for α above 3 or 4°, and friction dominates for α at <3°. The more pronounced minima and larger $\phi f\gamma$ product for the second draw results from the greatly increased yield

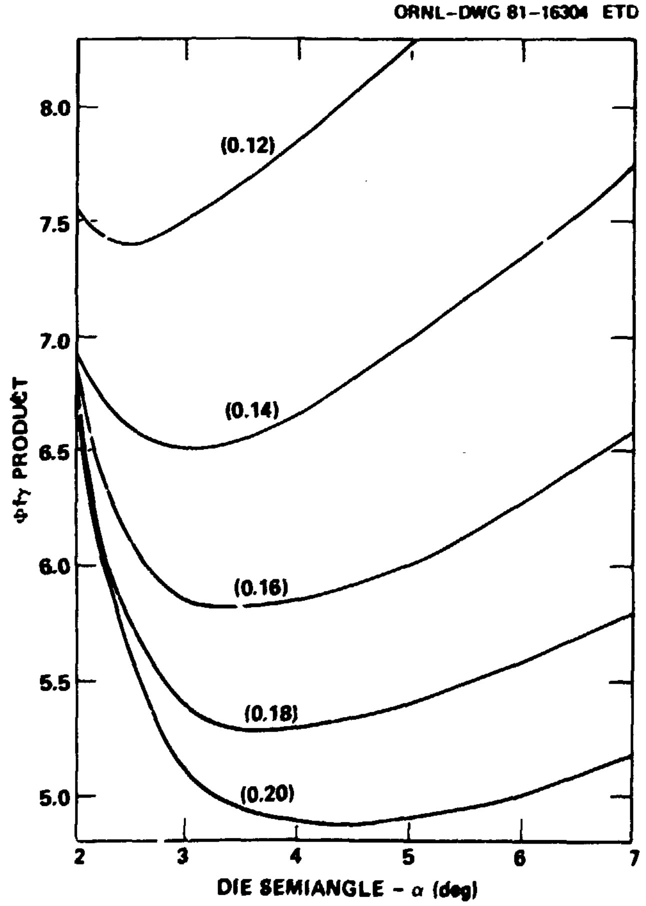

Fig. 32. $\phi f\tau$ product vs draw-die semiangle for various amounts of second-draw cold work ($\mu = 0.19$).

stress caused by strain hardening during the first draw. The yield stress, initially 35 x 10^6 kg/m^2, increases by a factor of 3 to 4 to σ_{s1} for the second draw. From Eq. (5.15), this proportionally increases the internal stress distribution with Δ. It is therefore extremely important to draw with Δ close to 1 on the second draw.

5.3.3 Thermoelement grain-size refinement

The development to produce the refined-grain thermoelements was performed by ORNL during fabrication of a quantity of bulk thermocouple material for ORNL by GMI. Using the actual production equipment avoided the effects on the final results of small variations in specific parameters such as deformation, furnace temperatures, and temperature gradients.

The fabrication process consisted of the following steps: (1) the MgO insulators were subjected to a 1000°C vacuum bakeout, and all materials were thoroughly cleaned; and (2) the thermoelement wires and MgO insulators were then assembled into an Inconel 600 sheath ~5 mm in diameter. The diameter of this assembly was reduced to 0.51 mm by a multiple-draw anneal cycle.

The development effort optimized both the drawing and the annealing processes to achieve the finest grain size possible, consistent with reasonable production times and material yields.

The new drawing and annealing schedule to obtain grain refinement was determined from (1) the preceding recrystallization and drawing theory, (2) literature information and physical property tests on the thermocouple components, and (3) industrial experience. The development consisted of three general tasks:

1. adjustment of annealing conditions to minimize grain growth of the Alumel thermoelement while still obtaining full recrystallization of the Inconel sheath and Chromel thermoelement,
2. definition of the existing drawing process in terms of Eqs. (5.3) and (5.4) and calculation of the friction factor f and coefficient of friction μ, and
3. determination of a new process to maximize the reduction between anneals by optimizing process parameters α and Δ in terms of Eqs. (5.17) and (5.18) and by comparison of draw and material stresses σ_{dE} and σ_s.

Annealing conditions were determined by drawing annealed samples of Chromel and Alumel wire and of assembled thermocouples to 20 to 50% cold work, followed by annealing at several time-temperature conditions. Elongation-to-failure tests, as well as metallographic and microhardness examination of annealed samples, were then used. Optimum annealing conditions were found to be 1025°C for 60 s for a 1-mm-diam thermocouple. The annealing temperature was then held constant and the time varied to account for thermocouple mass-per-unit-length changes with diameter. Annealing times ranged from 120 s at about 3-mm diameter to 30 s at 0.5-mm diameter.

The applicability of drawing Eqs. (5.3) and (5.4) to a nonhomogeneous thermocouple was investigated by (1) conducting tensile tests on Inconel, Chromel, and Alumel wires and on type K, Inconel-sheathed thermocouples and (2) conducting draw tests on samples of thermocouples and the Chromel thermoelement. Figure 33 summarizes the tensile tests. Comparison of

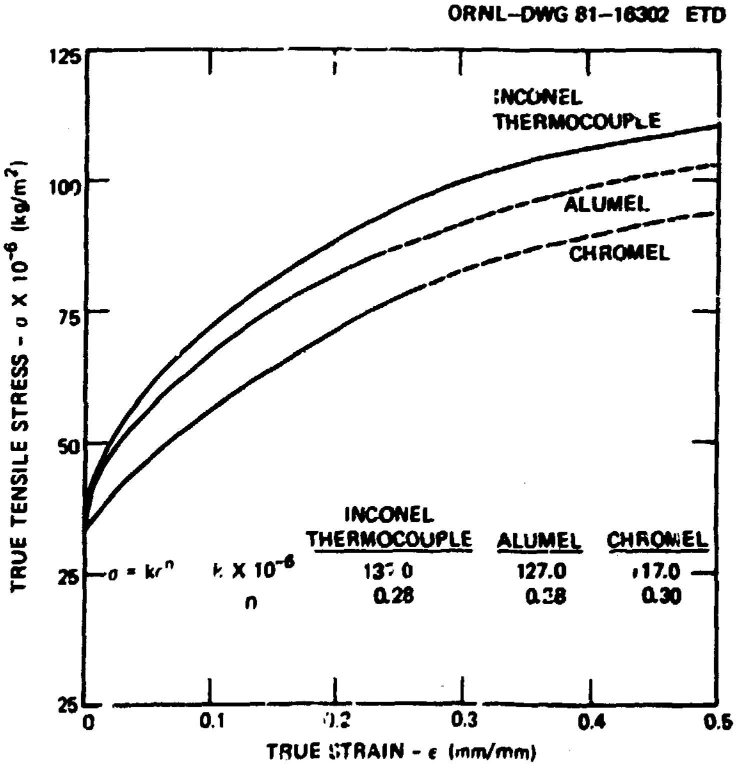

Fig. 33. True stress vs true strain for an Inconel-sheathed type K thermocouple and for Chromel and Alumel thermoelements.

plots of measurements on the individual thermocouple components with the thermocouple measurements indicates that MgO insulation substantially affects the tensile characteristics of the thermocouple even though it cannot itself sustain a tensile stress.

Strain-hardening constants for Eq. (5.2) were obtained by curve fitting using the thermocouple and Chromel stress-strain plot, and these values were used in Eqs. (5.3) and (5.4). Draw stresses σ_{d_1} and σ_{d_2} were measured with a standard spring balance placed between the draw bench-puller jaws and the thermocouple or Chromel wire being drawn. The friction factor f was then calculated for each of the samples. The results showed f to be ~35% higher for thermocouple drawing than for wire drawing. This apparently reflects the work associated with movement of the insulation as the thermocouple is reduced as well as relative movement of insulation material and thermocouple metallic components as the insulation transmits the draw stress to the thermoelement during thermocouple reduction. The insulation thus contributes to the work of deformation without supporting a balancing tensile stress.

The increased friction factor for thermocouple drawing serves to increase the draw stress for a given reduction or, equivalently, to reduce the maximum elongation possible for a given draw stress.

Calculation of the coefficient of friction μ was accomplished by drawing thermocouple samples with existing dies (with $\alpha = 6°$) from $\varepsilon = 10$ to 30% while measuring the draw stresses σ_{d_1} or σ_{d_2}. Strain-hardening constants from the thermocouple plot of Fig. 33 were used in Eqs. (5.3) and (5.4), and Eqs. (5.9) and (5.10) were used to calculate the frictional and redundant work terms, respectively.

Friction coefficient calculations from these measurements at first exhibited large variations. Draw dies that exhibited a larger-than-anticipated draw stress were replaced with new dies. In some cases, as much as a 40% decrease in draw stress was obtained for a new die under the exact drawing conditions imposed on the old one. This was attributed to die wear and variations in die bearing length B (Fig. 28). After die replacements, μ was measured to be 0.19 ± 10% for 90% of the dies tested, although variations up to 25% occurred.

The existing process consisted of drawing to 20 to 25% cold work in one step between anneals using draw dies with $\alpha = 6°$. During development, three new processes were obtained. In the first, the existing first-draw cold work (or slightly more) was retained, and a second draw of about 15% was added. Existing dies with $\alpha = 6°$ were used, in most cases, for both draws. In the second process, new dies with larger semiangles were designed, and the first-draw cold work was extended to about 42%. The final process combined the 40% maximum first-draw cold work with 15° second-draw cold work to obtain 55% cold work between anneals.

Optimization of the drawing and annealing schedule required continuity checks and elongation-to-failure tests of postannealed material. Excess stresses often did not immediately result in thermoelement open circuits. However, elongation-to-break tensile tests of postannealled thermocouples were excellent indicators of damaged or borderline material. Material correctly drawn and annealed experienced a true tensile elongation of 20 to 25% for both thermoelements and sheath, and the failure occurred initially in the sheath. Damaged material was characterized by initial failure of the Chromel thermoelement at a true strain of only 10 to 15% and, occasionally, failure of the Alumel thermoelement prior to that of the sheath as well. Material, once damaged, performed poorly in subsequent draws.

Table 23 summarizes part of the first process. As the table shows, the measured and calculated draw stresses for both first and second draws are in good agreement. However, internal stresses, calculated from Eqs. (5.17) and (5.18), are low on the first pass but high on the second pass. This is a direct result of the high Δ values produced by using the existing dies with $\alpha = 6°$. Open circuits of the Chromel thermoelement occurred on the second draw for σ_{dE}-to-σ_{ε} ratios of 108.4 and 99.8%. As development continued and the σ_{dE}-to-σ_{ε} ratio for the second draw was reduced by lowering α (and thus Δ), the incidence of open circuits decreased. All failures were caused by Chromel thermoelement opens; no sheath breaks occurred.

Table 24 summarizes the second and third draw-anneal processes. The second process used draw dies with a semiangle of 11°, based on the predictions of Fig. 31, and an attempt was made to limit die-bearing length

Table 23. Type K, Inconel-sheathed thermocouple
draw-anneal schedule for process I

Percent cold work (s)		Anneal time at 1025°C (s)	Draw stress σd (kg/m²)		Error (%)	Calculated internal stress σ_{dE} (kg/m²)	σ_{dE}/σ_b x 100 (%)	Process parameters	
Per draw	Total		Calculated	Measured				α	Δ
26.4			58.6	59.3	-1.2	66.0	69.9	6	1.6
15.3	41.7	90	52.7	51.9	+0.6	100.1	93.3	6	2.7
30.3			68.9	69.5	+0.6	74.1	75.4	6	1.4
12.2	42.7	60	45.5	45.7	-0.2	104.3	96.6	6	3.4
28.1			62.8	60.9	+3.1	66.5	69.3	6	1.5
9.7	37.8	45	40.4	50.8	-20.5	113.1	108.4	5	3.6
27.6			61.4	61.6	-0.3	67.2	70.3	6	1.5
12.5	40.1	45	45.6	47.8	-2.5	105.9	99.8	6	3.4
28.6			64.2	64.6	-0.6	70.2	72.7	6	1.5
11.5	40.1	30	50.6	46.7	+8.4	89.0	83.9	4	2.4

Table 24. Type K, Inconel-sheathed thermocouple draw-anneal schedule for processes II and III

Present cold work (%)		Anneal time at 1025°C (s)	Draw stress σd (kg/m^2)		Error (%)	Calculated internal stress σ_{dE} (kg/m^2)	$\sigma_{dE}/\sigma_s \times 100$ (%)	Process parameters	
Per draw	Total		Calculated	Measured				α	Δ
				Phase II					
40.8		90	74.4	84.7	-12.2	94.2	88.4	11	1.9
40.8		60	74.4	82.8	-10.1	92.3	77.7	11	1.9
37.8		45	68.2	86.4	-21.1	96.6	92.6	11	2.0
39.3		45	71.7	87.3	-17.9	97.5	92.4	11	2.0
41.8		30	76.0	99.6	-23.7	108.0	100.5	11	1.8
				Phase III					
41.5			76.1	89.9	-15.4	99.4	92.8	11	1.9
15.9	57.4	60	85.5	70.5	+21.3	90.7	77.3	3	1.3
42.5			77.6	101.7	-23.7	110.1	102.1	11	1.8
18.6	61.1	45	98.9	90.0	+9.9	101.6	85.1	3	1.1
43.4			79.7	110.6	-27.9	119.0	109.7	11	1.8
17.8	61.2	30	96.0	92.1	+4.2	108.1	90.5	3	1.2

to 15% of L (Fig. 28). Correlations between measured and calculated draw stresses decreased considerably with an additional 10 to 15% first-draw cold work. First-draw predicted values average 17% below those measured. Extrapolation of the strain-hardening constants to high cold work values or frictional behavior that results in the friction factor f increasing with cold work [Eq. (5.9)] could account for this.

Process III, presented in Table 24, summarizes the latest draw-anneal schedule, still under development, in which 55% cold work between anneals is achieved by drawing in two draws. Dies for the second-draw pass were designed with $\alpha = 3°$ in accordance with the predictions of Fig. 32. The measured first-draw stresses were also higher than those predicted by Eq. 5.3, but the measured second-draw stresses were lower in contrast to those of process I with lower first-draw cold work.

Errors in the strain-hardening constant n, the redundant work term θ, or the friction factor f at high first-draw cold work must have occurred to account for these discrepancies. Second-draw redundant work is high for process I and low for process III, so higher redundant errors would be expected in process I than in III if ϕ errors dominate. Some strain-hardening error at high cold work is probable. However, draw tests at $\varepsilon \cong 0.42$ that resulted in sheath breakage ($\sigma_{\varepsilon} = \sigma_{d_1}$) indicated that σ_{ε} is within about +8% of the value obtained from thermocouple strain-hardening constants. Because the apparent coefficient of friction μ is higher for thermocouple drawing than for wire drawing, an additional increase in μ at high cold work is reasonably assumed to account for much of the discrepancy in calculated vs measured draw stress. For this assumption to be true, μ, which is constant at 0.19 for cold work up to 30%, must increase sharply to $\mu \cong 0.3$ for cold work above 40%. No mechanism is yet available to account for this phenomenon.

The schedule developed in process I was used to produce thermocouple bulk material with an average length of about 50 m. Failure of the Chromel thermoelement caused by high internal stresses was the limiting factor. The process II schedule was used to produce thermocouple bulk material with an average length of about 100 m with sheath breakage limiting the process. Although long bulk material lengths are possible with process III above about 1 mm in diameter, development has not been completed to obtain 0.5-mm material in lengths comparable with those of process II.

First-draw cold work for both processes II and III is limited to a maximum of about 42% by sheath breakage. The process III second draw, while extending the cold work up to 20%, is limited on the low side of α by friction and on the high side by high internal stresses. When two draws are used to obtain maximum cold work, diametrical tolerances of both draw dies are critical to maintaining second-draw cold work within 10 to 20% as thermocouple diameter is reduced below about 1.5 mm.

More than 3500 m of bulk thermocouple material was produced during process development. Figure 34 shows the microstructure of the Chromel and Alumel thermoelements resulting from an average of 40% cold work between anneals. The micrograin sizes of the thermoelements are ASTM 11 and 9 (15,900 and 3,970 grains/mm²), respectively.

ORNL PHOTO 5019-80

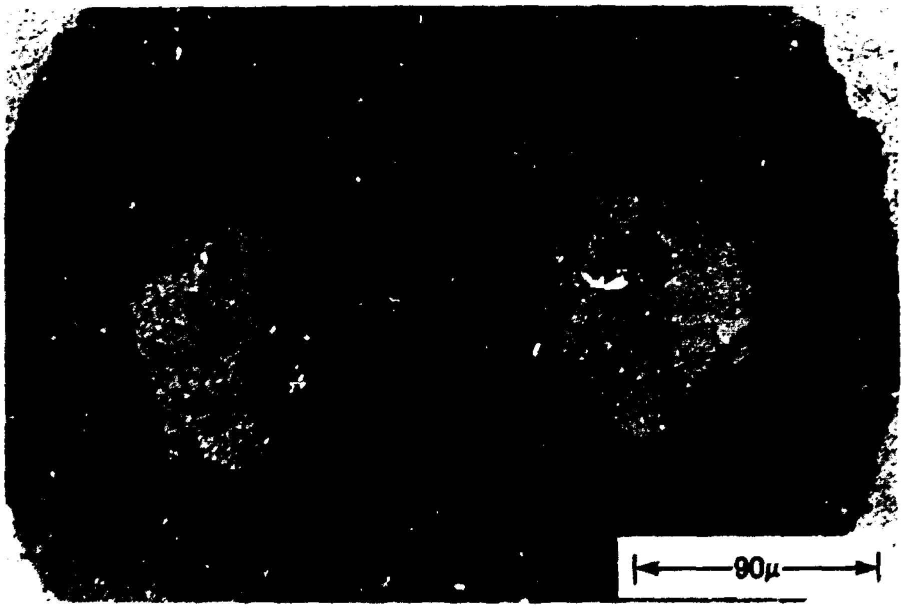

Fig. 34. Chromel (left) and Alumel average grain size is 9 and 17 μ (ASTM 11 and 9), respectively, after grain size refinement (400x).

5.4 Summary and Conclusions

Premature failure of small-diameter, type K Inconel-sheathed thermocouples required an investigation into the causes of failure and ways to improve lifetime. Failure was judged to be caused by thermoelement grain growth and embrittlement. The brittle condition was characterized by large grains with respect to thermoelement diameter and by voids and oxides formed along the grain boundaries. Major contributors to this condition were impurities introduced during thermocouple assembly and, particularly, critical amounts of cold work left in the thermocouple caused by incomplete annealing or introduced by swaging during FRS fabrication. The embrittled thermocouples subsequently failed when thermally activated expansion mismatched between them, and the FRS cladding imposed relatively small axial strains on the thermoelements, causing grain-boundary separations. Three characteristics were established as important to improved thermocouple performance under high-temperature, thermal cycling conditions:

1. elimination of prestrain in the thermoelements prior to operation of the thermocouple above their recrystallization temperature;
2. minimization of oxygen, moisture, and hydroxides within the thermocouple; and
3. refinement of the thermoelement grain size to meet ASTM micrograin size 9 or smaller (as a goal).

Significant improvements in thermocouple performance were demonstrated simply by eliminating small amounts of cold work in the material by a recovery anneal prior to their use. Additionally, a 1000°C vacuum bakeout of the insulators prior to their assembly into the thermoelement sheath, careful cleaning, and thermocouple assembly with an inert cover gas were added to the thermocouple fabrication process. Finally, refinement of thermoelement grain size to ASTM micrograin size 9 for Alumel and 11 for Chromel was accomplished by development of a new draw-anneal process.

Annealing conditions were established as 1025°C for 30 to 120 s, depending on thermocouple diameter. The drawing process was optimized by application of the general wire-drawing equation $\sigma_d = f\phi\int\sigma d\epsilon$ to thermocouple drawing. The equation was extended to describe internal stresses for multiple-pass drawing of thermocouples, and process parameters were evaluated and optimized to increase cold work between anneals from 25 to 60%. This maximum cold work level was achieved in two draws between anneals averaging 40 and 15%, respectively. High second-draw yield stress caused by first-draw strain hardening combined with frictional losses to limit second-draw cold work to 10 to 20% with a draw die semiangle of 3 to 4°. The friction factor $f = (1 + \mu \cot \alpha)$ was found to be about 35% higher for thermocouple drawing than for equivalent wire drawing and also appeared to be a function of the per-draw cold work level when cold work was >30%.

Improved grain size was most easily achieved by single-pass drawing to an average of 40% cold work between anneals. Although further improvement in grain size occurred with the 55%, multiple-pass process, diametrical tolerances were critical below about 1.5 mm because small diametrical changes in either draw die caused a relatively large second-draw cold work change.

REFERENCES

1. Uri Gat and P. R. Kasten, *Gas-Cooled Reactor Programs Annual Progress Report for Period Ending December 31, 1977*, ORNL-5426.

2. Uri Gat and P. R. Kasten, *Gas-Cooled Reactor Programs Annual Progress Report for Period Ending December 31, 1978*, ORNL-5560.

3. Uri Gat and P. R. Kasten, *Gas-Cooled Reactor Programs Annual Progress Report for Period Ending December 31, 1979*, ORNL-5675.

4. Uri Gat and P. R. Kasten, *Gas-Cooled Reactor Programs Annual Progress Report for Period Ending December 31, 1980*, ORNL-5808.

5. W. E. Baucum et al., *State of the Art of Fuel Pin Simulators for LMFBR Out-of-Reactor Tests Status Report*, ORNL-TM-5889 (September 1977).

6. R. W. McCulloch, P. T. Jacobs, and D. L. Clark, *Development of a Fabrication Procedure for MABT Fuel Simulator Based on the Use of Cold-Pressed Boron Nitride Preforms*, NUREG/CR-1111 (ORNL/NUREG/TM-362) (March 1980).

7. D. L. Clark, R. W. McCulloch, and R. E. MacPherson, *Fabrication Technology Development of Fuel Rod Simulators for Blowdown Heat Transfer Tests*, ORNL-5712 (to be published).

8. V. Casal, E. Grof, and W. Hartmann, *Heater Rods to Simulate Fuel Pins for Single-Phase Heat Transfer Tests in Liquid Metal Flows*, KfK 2258, (ORNL-tr-4360) (September 1976).

9. R. L. Ludwig, *Investigation of LMFBR Prototype 7A Heaters and the Metallurgy of the Platinum-8 Weight Percent Tungsten Alloy*, Y-2053 (September 1976).

10. D. E. Harasyn and R. K. Williams, *Grain Growth Control in Pt-8%W by Powder-Metallurgy Processing*, ORNL/TM-6615 (February 1979).

11. A. J. Moorhead et al., *Development of Joining Techniques for Fabrication of Fuel Rod Simulators*, ORNL-5673 (October 1980).

12. R. W. McCulloch, compiler, *Proceedings of the International Symposium on Fuel Rod Simulators-Development and Application, Gatlinburg, Tennessee, October 1980*, CONF-801091 (June 1981).

13. D. L. Clark and T. S. Kress, U.S. Patent No. 3,912,908, *Electric Cartridge-Type Heater for Producing a Given Non-Uniform Axial Power Distribution*, Oct. 14, 1975.

14. J. F. Potts, Jr., and D. L. McElroy, *Thermocouple Research to 1000°C — Final Report November 1, 1957–June 30, 1959*, ORNL-2773 (January 1961).

15. R. L. Anderson and T. G. Kollie, *Accuracy of Small Diameter Sheathed Thermocouples for the Core Flow Test Loop*, ORNL-5401 (April 1979).

16. R. E. Reed-Hill, *Physical Metallurgy Principles*, p. 144, Van Nostrand Reinhold Company, New York, 1964.

17. N. F. Spooner and J. M. Thomas, "Longer Life for Chromel-Alumel Thermocouples," *Met. Prog.* (November 1955).

18. P. G. Shewman, *Transformations in Metals*, p. 96, McGraw-Hill Book Company, New York, 1969.

19. Letter from R. L. Ludwig to R. L. Anderson, Jan. 15, 1979; Subject: Examination of Thermal Cycled Type K Sheathed Thermocouples.

20. B. F. Dyson and D. E. Henn, "The Effect of Room Temperature Prestrain on Grain Boundary Cavitation in Nimonic 80A," *J. Micros.* 97 (1/2), 165–70 (January–March 1973).

21. B. F. Dyson and M. J. Rodgers, "Prestrain, Cavitation, and Creep Ductility," *Met. Sci. J.* 8, 261–66 (1974).

22. W. A. Backofen, *Deformation Processing*, Addison-Wesley Publishing Co., Inc., Reading, Mass., 1972.

ORNL-5864
Dist. Category UC-77

Internal Distribution

1. S. J. Ball
2. A. J. Caputo
3. N. C. Chen
4. W. R. Clark
5. C. W. Collins
6. J. C. Conklin
7. R. G. Donnelly
8. J. R. Dougan
9. W. P. Eatherly
10. U. Gat
11-15. A. G. Grindell
16. W. A. Hartman
17. R. E. Heestand
18. R. E. Helms
19. P. G. Herndon
20. T. L. Hudson
21. W. R. Huntley
22-31. P. R. Kasten
32. W. J. Lackey, Jr.
33. E. M. Lees
34-38. R. E. MacPherson
39. H. E. McCoy, Jr.
40-44. R. W. McCulloch
45. A. J. Moorhead
46. T. W. Robinson, Jr.
47-51. J. P. Sanders, Sr.
52. R. L. Senn
53. H. E. Trammell
54. H. C. Young
55. ORNL Patent Office
56. Central Research Library
57. Document Reference Section
58-59. Laboratory Records Department
60. Laboratory Records, RC

External Distribution

61. J. E. Fox, High Temperature Reactor Program, Department of Energy, Washington, DC 20545
62. G. A. Newby, High Temperature Reactor Program, Department of Energy, Washington, DC 20545
63. Director, Office of Nuclear Power Systems, Department of Energy, Washington, DC 20545
64. Manager, DOE, SAN-San Diego, 110 West A Street, Suite 460, San Diego, CA 92101
65. Office of Assistant Manager for Energy Research and Development, DOE, ORO, Oak Ridge, TN 37830
66-196. Given distribution as shown in DOE/TIC-4500 under category UC-77 (Gas Cooled Reactor Technology)

☆U.S. GOVERNMENT PRINTING OFFICE 1983 646 055/310